Dissertation zur Erlangung des Doktorgrades
der Fakultät für Chemie und Pharmazie
der Ludwig-Maximilians-Universität München

The Role of Branched Actin Networks in Dendritic Cell Physiology

Alexander Eichner

aus

München, Deutschland

2013

Anfangs wollt ich fast verzagen,
Und ich glaubt, ich trüg es nie;
Und ich hab es doch getragen -
Aber fragt mich nur nicht, wie?

(Heinrich Heine)

SUMMARY

The role of branched actin networks in dendritic cell physiology

Dendritic cells (DCs) are the link between innate and adaptive immunity. At steady state, they reside within peripheral tissues and display low motility. Upon pathogen encounter, they adopt a highly motile state and migrate into the draining lymph node where they present peripherally acquired antigen to lymphocytes. Migrating DCs are confronted with diverse tissue environments, demanding a high degree of flexibility. As a result, DCs undergo constant amoeboid shape changes generated by actin cytoskeletal dynamics. The actin cytoskeleton is established by both cross-linked filamentous actin bundles and branched lattice-like structures. Its dynamics rely on constant turnover of actin filaments by cycles of polymerization and depolymerization. The spatiotemporal regulation of the polymerization rate is considered to be the central regulator of such actin driven shape changes. However, the effect of actin filament geometry on shape and migration has not been assessed yet.

Therefore, we aimed to investigate the role of actin network branching for DC morphology and migration. Actin branches are initiated by the Arp2/3 complex, which in turn is activated by nucleation promoting factors (NPFs) of the WASP and WAVE families. To study the consequences of loss of Arp2/3 function at the plasma membrane, we employed bone marrow derived DCs devoid of NPFs. Whereas neither WASP nor WAVE ablation affected differentiation and maturation, WAVE depleted DCs showed pronounced morphological alterations. In immature DCs the lack of WAVE caused a unipolar pointed cell shape with leading edges constituted of entirely branch-free, parallel arrays of filaments. Surprisingly, these cells migrated with increased velocity and their hyperpolarized shape caused a substantial increase in directional persistence. Despite their enhanced motility, WAVE deficient cells were unable to interpret chemotactic gradients. After maturation, actin branching was partially restored and chemotactic potential regained. The additional finding that WASP localizes to the leading edge of migrating mature DCs suggests an alternative Arp2/3 activation pathway.

In conclusion, we show that loss of actin branching severely alters cell shape, which in turn affects cell polarity, migratory behaviour and chemotaxis of DCs. We further show that, depending on the maturation state of DCs, actin branching at the leading edge is regulated by different pathways. While immature DCs exclusively rely on WAVE complex-dependent Arp2/3 activation, maturation enables an alternative Arp2/3 activation pathway that partially compensates for the absence of WAVE complex.

12

TABLE OF FIGURES

LIST OF ABBREVIATIONS

-/-	Knockout
fl/fl	loxP-containing conditional targeted gene (both alleles)
2D	Two-dimensional
3D	Three-dimensional
Ab	Antibody
ADP	Adenosine-5'-diphosphate
Ag	Antigen
ANOVA	Analysis of variance
APC	Allophycocyanin
aPKC	Atypical protein kinase C
Arp2/3	Actin related protein 2/3
ATP	Adenosine-5'-triphosphate
ATPase	Adenosine-5'-triphosphatase
Bp/kbp	Base pair(s), kilo base pairs
BSA	Bovine serum albumin
C-terminal, C-terminus,	Carboxy-terminus, carboxy-terminal
C57BL/6	Inbred mouse strain "C57 black 6"
CCL	CC- or β-chemokine
CCR	CC- or β-chemokine receptor
CD	Cluster of differentiation
Cdc42	Cell division cycle 42
CFSE	Carboxyfluorescein succinimidyl ester
CRIB	Cdc42-Rac1 interactive binding
ctrl	Control
D10	DMEM supplemented with glutamine and 10% FCS
Da/kDa	Dalton/kilodaltons
DC	Dendritic cells
ddH$_2$O	Double distilled water
DMEM	Dulbecco's Modified Eagle Medium
DMSO	Dimethyl sulfoxide
DNA	Deoxyribonucleic acid
dNTP	Deoxynucleotide -5'-triphosphate
ECM	Extracellular matrix
EDTA	Ethylenediaminetetraacetic acid
EM	Electron Microscopy
FACS	Fluorescence-activated cell sorting
FCS	Fetal calf serum
Fig.	Figure
FITC	Fluorescein isothiocyanate
FSM	Fluorescent speckle microscopy
GAP	GTPase activating protein

GB	Gigabyte
GDI	GDP dissociation inhibitor
GDP	Guanosine-5'-diphosphate
GEF	Guanine nucleotide exchange factor
GFP	Green fluorescent protein
GM-CSF	Granulocyte-macrophage colony-stimulating factor
GPCR	G protein-coupled receptor
GTP	Guanosine-5'-triphosphate
GTPase	Guanosine-5'-triphosphatase
HBSS	Hank's buffered salt solution
HEK	Human Embryonic Kidney 293 cells
Hem1	Hematopoietic protein 1
HEPES	N-(2-hydroxyethyl)-piperazine-N'-2-ethanesulfonic acid
hr(s)	Hour(s)
HRP	Horseradish peroxidase
Ig	Immunoglobulin
IL	Interleukine
IRM	Interference reflection microscopy
IRSp53	Insulin receptor substrate p53
IS	Immune synapse
KB	Kilobyte
KO	Knockout
LN	Lymph node
LoxP	Locus of X-over P1; site on the bacteriophage P1 genome consisting of two 13 bp inverted repeats flanking a 8 bp spacer region
LPS	Lipopolysaccharide
M-CSF	Macrophage colony-stimulating factor
MACS	Magnetic-activated cell sorting
MB	Megabyte
MEF	Mouse embryonic fibroblast
MEM	Minimum essential medium
MHC	Major histocompatibility complex
min	Minutes
mm	millimetre
MMP	Matrix metalloproteinase
MOPS	3-(N-morpholino)propanesulfonic acid
MT	Microtubule
MTOC	Microtubule organizing center
MyoII	Myosin II
N-terminal, N-terminus	Amino-terminus, amino-terminal
n.s.	not significant
Nm	Nanometer
nM	Nanomolar
OVA	Chicken Ovalbumin
Par	Partitioning defective

PBS	Phosphate buffered saline
PCR	Polymerase chain reaction
PE	Phycoerythrin
PEG	Polyethylene glycol
PH	Pleckstrin homology
pH	Power of hydrogen
P_i	Inorganic phosphate
PI3K	Phosphatidylinositide 3-kinase
PLT	Primary lymphoid organs
PRD	Proline-rich domain
PtdIns(3,4,5)P_3/PIP$_3$	Phosphotidylinositol-3,4,5-trisphosphate
PtdIns(4,5)P_2/PIP$_2$	Phosphatidylinositol-4,5-bisphosphate
PVDF	Polyvinylidene fluoride
R10/20	RPMI supplemented with glutamine, penicillin/streptomycin and 10% or 20% FCS, respectively
Rac	Ras-related C3 botulinum toxin substrate
rpm	Repeats per minute
RPMI	Roswell Park Memorial Institute medium
RT	Room temperature
SCAR	Suppressor of cAMP receptor
SDS-PAGE	Sodium dodecyl sulfate polyacrylamide gel electrophoresis
sec	Seconds
SEM	Standard error of the mean
SH2/3	Src Homology 2/3 domain
SLO	Secondary lymphoid organ
Src	Sarcoma tyrosine-protein kinase
T cell	T helper cell
TAT	Trans-Activator of Transcription
TAT-Cre	Cre Recombinase from bacteriophage P1 fused to TAT protein; Cre catalyzes the site-specific recombination between two DNA recognition sites termed loxP sites
TBS	Tris buffered saline
TCR	T cell receptor
TD	Thoractic duct
TIRF	Total internal reflection fluorescence
UAA	Under-agarose migration assay
VASP	Vasodilator-stimulated phosphoprotein
WASp	Wiskott–Aldrich Syndrome Protein
WAVE	Wiskott-Aldrich syndrome family protein
WT	Wildtype
μm	Micrometre
μM	Micromolar

INTRODUCTION

Leukocyte migration and trafficking

Cell migration – an introduction

Cell migration is a fundamental process in biology, relevant for unicellular bacteria or archaea to protozoa and finally to multicellular metazoa. Across phyla, it can occur at the single cell level or as a collective in which cells move co-ordinately by retaining cellular contacts (Friedl and Wolf, 2010). Cell migration serves many purposes: whereas unicellular organisms mainly use motility to trace nutrition sources and to assure survival and reproduction, multicellular organisms use cell migration in several steps and processes of their life cycle starting from the self organization during development and tissue formation, maintaining the organism's integrity and finally in sexual reproduction. Cell migration within an organism has to be precisely regulated since uncontrolled migration during cell differentiation significantly contributes to cancer formation and metastasis (Yang and Weinberg, 2008).

Cell locomotion, the ability and the process to move between different sites, requires an intrinsic force generator that can be coupled and transduced to the substratum and finally leads to the translocation of the cell. In the bacterial and archaeal kingdom as well as in eukaryotic sperm cells, single cell migration uses the propulsive force of the so-called "flagellum". The flagellum generates propulsion by translating biochemical into mechanical power via a molecular motor that rotates this lash-like cell protrusion. In contrast, the archetype of metazoan cell migration is characterized by four steps: (1) protrusion formation, (2) protrusion coupling to the substratum, (3) de-adhesion of the cell's rear and (4) retracting the cell body (Fig. 1) (Abercrombie, 1980; Mitchison and Cramer, 1996). Differences in cellular morphology, formation and employment of subcellular structures during these steps led to the classification of different migration modes

1) Protrusion of the leading edge

2) Adhesion at the leading edge

3) De-adhesion at the trailing edge

4) Retraction of the cell body
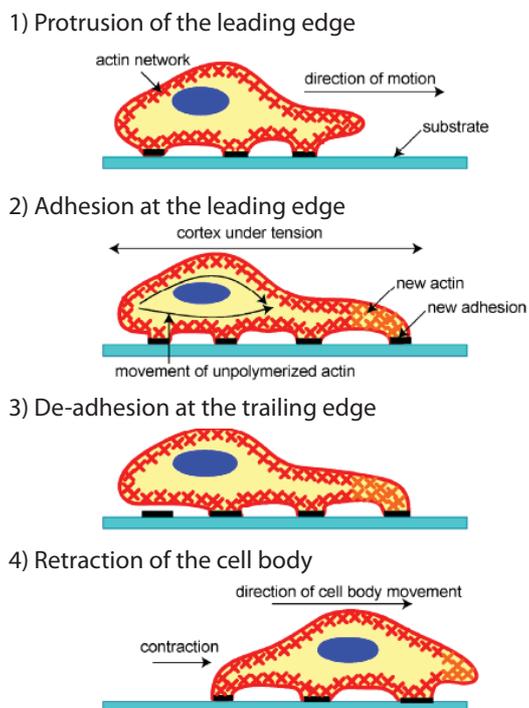
Fig. 1. The four steps of metazoan cell crawling (by (Abercrombie, 1980)). (1) Actin-driven extension of the leading edge and subsequent (2) adhesion of the newly formed protrusion to the substrate. (3) De-adhesion from the substrate at the cell's rear allows for (4) retraction of the cell body by contraction (taken from(Ananthakrishnan and Ehrlicher, 2007)).

(Friedl and Wolf, 2010). Furthermore, the properties and dimensionality of the substrate, e.g. the extracellular matrix (ECM) and/or cellular networks, imposes certain migration strategies. A first categorization was made by the discrimination of "mesenchymal" and "amoeboid" migration. Mesenchymal migrating cells characteristically form stable and sustained interactions with the ECM via organized adhesion structures, also referred to as focal contacts. Thereby, the ligation of the cell surface receptors of the integrin family by components of the substratum plays a key role in both signal and force transduction. This schematic is often associated with matrix degradation via controlled secretion of matrix metalloproteases (MMPs) in three-dimensional migration. The amoeboid mode of migration is derived from the protozoon *Amoeba proteus* and is characterized by constant cell shape changes driven by rapid and repetitive cycles of protrusion and contraction. The relatively short and weak engagement of the integrin receptors by substrate ligands results in a smooth gliding behaviour with maximum morphological adaption to the complexity of the ECM. Two subtypes of amoeboid movement can be distinguished by how the protrusive force is generated. During bleb-mediated migration the cell forms a balloon-like, actin-free membrane protrusion resulting from local membrane-cortex detachment and hydrostatic pressure-driven influx of the cell's cytoplasm. Thereby, propulsion is a consequence of contraction rather than cytoskeletal protrusion. In contrast, an amoeboid "pseudopodal" cell employs biochemical modifications of the cell's cytoskeleton to locally exert force on the membrane resulting in the formation of a protrusion. Depending on its morphology and cytoskeletal organization one can classify protrusion types.

Adhesion or the interaction of the migrating cell with the substratum is used to couple and transduce intracellularly generated force to the ECM and finally to move relative to it. Strength, number and turnover rates of adhesion sites determine cell shape and velocity or ultimately the cell's physiology. Mesenchymal cells literally migrate pinned down by a large number of substantial and robust adhesions with slow turn over resulting in elongated, spread-out cell morphologies and a limiting parameter in terms of migration velocities. In contrast, amoeboid locomotion can be considered as rather fast, with weak and short-lived contact sites on the substratum resulting in more compact cell morphology and enabling rapid, flexible crawling on and through complex structures of the ECM.

Important to note is that this classification does not necessarily connect specific cell types with certain migration modes. Many cells have to struggle with different environmental requirements during their life cycle, which they overcome and adapt to via mode transitions. Thus, migration types should be considered as extremes of a continuum with a certain degree of plasticity to enable cells to adapt to different environmental requirements and to fulfil their inherent biological function (Huttenlocher and Horwitz, 2011).

Cell migration within the immune system
Challenges and requirements of immune cell migration
The immune system is a key component of higher eukaryotic organisms to maintain tissue integrity and homeostasis. Whereas most cell types in a healthy adult organism, comprising

the connective, epithelial, muscular and nervous tissue, hardly move and are locally restricted when terminally differentiated, cells of the immune system need to be able to travel large distances and to pass several tissue barriers to make the immune system work and to guarantee protection against pathogenic invasion at any site of the body. Its function depends on the perfectly tuned interplay of a specialized group of cells, namely the leukocytes. Leukocytes need to sense danger, process and integrate this information, transmit it to and communicate with other cells, and sometimes even chase and combat pathogenic invaders. At steady state, leukocytes are either circulating between the blood and the lymphatic system or need to be precisely positioned in the tissue. In addition, they constantly need to be replaced upon cell death to keep the whole organism primed for danger. During inflammation, repositioning as well as replacement ensures an efficient and highly specific immune response with respect to the pathogen and its localization. Thus, a major prerequisite for immune-surveillance and response is leukocyte migration. Its pivotal role in immunity has been a challenging subject in research over decades.

Leukocyte trafficking

Leukocytes need to populate the entire body to guarantee its full protection. Originating from primary lymphoid organs, leukocytes travel between the blood circulation, the interstitium and lymphoid tissues, a process referred to as leukocyte trafficking (Fig. 2). Immune cell migration can occur either passively by employing fluidic streams, e.g. blood and lymph, or actively, which requires inherent force generation and transduction by the cell. Rapid pathogen clearance and limitation of tissue damage demands fast migrating cells. Shuttling streams as well as migration tracks are extrinsically provided by the blood and lymph system. Intrinsically, leukocytes need to use a migration mode that allows for high velocities and a maximum in adaption to the substratum. Indeed, it was shown that leukocytes exhibit amoeboid migration with constant and rapid cycles of morphological expansion and contraction, which allows for fast migration (2-30 μm/min)(Friedl et al., 1998b). They lack
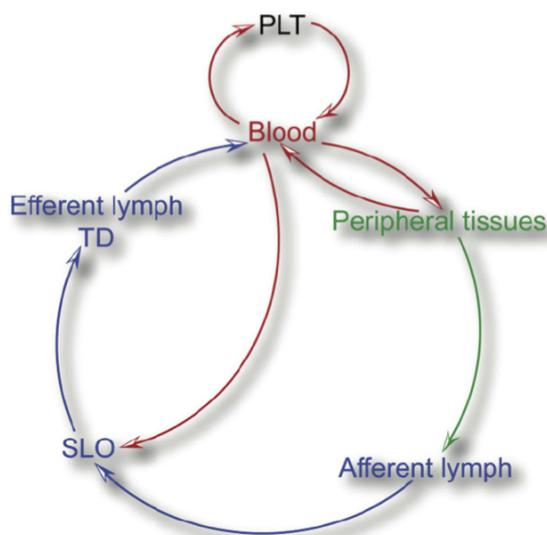
Fig. 2. Leukocyte trafficking. Immune cells originate from primary lymphoid tissues (PLT) such as the bone marrow or the thymus. From there they start trafficking via the blood stream. Some immune cells, e.g. DCs, leave the blood to seed peripheral tissues, where they reside until they receive an activating signal. Subsequently, DCs start migrating via the afferent lymphatics to next draining lymph node. Other cells, like B and T cells enter SLOs via the blood circulation. Leukocytes leave SLOs via efferent lymphatics followed by re-entry of the blood circulation via the thoracic duct (TD). Thereby, trafficking involves both, active migration by the cell and passive transportation by fluidic streams (blood and lymph)(taken from (Alvarez et al., 2008)).

stable focal adhesions and only form short-lived weak interactions with the ECM via integrins. In interstitial migration (3D) integrin-mediated adhesions are largely dispensable (Friedl et al., 1998a; Lämmermann et al., 2008). The cells are rather thought to entangle in and exert force laterally to adjacent fibrils of the ECM mesh, thereby squeezing themselves through narrow pores. This results in a mode of migration that is metaphorically best described as "chimneying" and supports the capability to adapt to the complexity and heterogeneity of the interstitium without degrading it by pericellular proteolysis (Friedl and Wolf, 2003; Lämmermann et al., 2008; Malawista et al., 2000; Mandeville et al., 1997; Wolf et al., 2003b).

In addition to 3D interstitial migration, leukocytes are also confronted with 2D environments, for example vessel walls, peritoneum and pleura. The reduction in dimensionality leads to the loss of opposing interaction sites and subsequently the incapability to move forward by pushing and squeezing. Therefore, to transduce force the cell requires coupling to the substratum via integrin-mediated adhesion that finally generates traction. In contrast to mesenchymal migration, leukocyte anchoring to the substrate is still a compromise between traction and speed. Within the protrusion zone only transient and spatially restricted nascent adhesions or focal complexes are assembled. Cell-matrix contacts are still integrin-mediated, but in contrast to focal adhesions, rapidly get disassembled. In fast migrating leukocytes, these adhesions do not mature to focal adhesions and do not connect to actin stress fibers (Alexandrova et al., 2008; Choi et al., 2008). They appear as less organized, dot-like adhesions (Huttenlocher et al., 1995) present only in the very front part of the cell but still efficiently transduce intracellularly generated force. Thus, local confinement paired with a high turnover of substrate attachment sites guarantees for a fast forward movement.

Leukocyte guidance

The challenge but also the beauty of the immune system is to have the appropriate leukocyte in the right place at the right time. This requires both a unique adaptability and flexibility in migration, which is at the same time precisely coordinated and tightly controlled. Misregulation of leukocyte migration contributes to a variety of diseases including immunodeficiency, autoimmunity and cancer. Tissue barriers, e.g. the endothelial layer or the basement membrane, and environmental changes conduct to the compartmentalization of body tissue and fluids, but also provide regulation points of leukocyte migration by controlling the direction of migration within as well as during tissue entry or exit (transmigration). Environmental cues attract and thereby accurately navigate immune cells across tissues to their site of action. Only leukocytes expressing the corresponding receptors are able to sense, integrate and respond to those guidance cues. Preceding signals, which determine the state of the cell and prime it for subsequent cues, in turn regulate their responsiveness. Thus, cell intrinsic properties and exogenous factors assure and orchestrate leukocyte trafficking.

Different principles of cell-environment interactions are employed during leukocyte guidance. Haptokinesis (greek, hapto = touch, contact; kinesis = movement, motion) depends

on the interaction between the leukocyte and the substratum and leads to an undirected contact-driven migration. On 2D substrates, e.g. the vascular endothelium, these interactions are integrin-dependent whereas three-dimensional amoeboid migration dispenses with integrins (see above)(Friedl et al., 1998a; Lämmermann et al., 2008). Haptokinesis can result in guidance when cells are crawling along non-random organized tissue structures.

Directional migration is guided by graded concentrations of chemotactic guidance cues. During chemotaxis (new latin, chemo = chemistry; greek, taxis = order, arrangement) soluble chemoattractants freely diffuse from a source in the surrounding environment resulting in a concentration gradient. Chemotactic leukocytes are able to sense low concentration differences of chemokines, polarize and migrate towards the source. If chemokines are immobilized on structural components of the ECM, directional migration is described as haptotaxis. Together these principles ensure controlled leukocyte trafficking.

Cell shape, polarity and migration

The actin cortex and cell shape control
The composition and organization of the cell cortex
A fundamental idea in biology is that shape determines function. Whereas protein function is strongly dependent on its 3D structure, cell shape is rather an attribute and might contribute to its function. In eukaryotic animal cells lacking a cell wall, shape is mediated and maintained by the actin cell cortex, an active cytoskeletal shell directly linked to the plasma membrane. Coupling to the plasma membrane makes the cortex the main determinant of mechanical stiffness and resistance to external forces and intracellular osmotic pressure - similar to the cell wall in other cell types (Bray and White, 1988). But the crucial difference between a rather rigid and static cell wall located outside the membrane is the dynamic plasticity of the cortex. It was back in 1939 as W.H. Lewis already postulated a "superficial plasmagel layer" with contractile properties that contributes to "form, locomotion and division" (Lewis, 1939). In 1986, D. Bray and J.G. White pursued his idea and suggested that cortical contraction leads to intracellular flows that promote these cellular properties and events (Bray and White, 1988). Nowadays we have a more detailed view of the structure, composition and assembly of the cortex, which give rise to its physical properties and function, albeit not everything is known and understood. The close proximity of the cortex to the plasma membrane makes it an accessible object to study its dynamics using modern live imaging microscopy methods (IRM, TIRF, FSM), but hinders a detailed analysis of its ultrastructural organization by electron microscopy (EM) due to difficulties and limitations in cortex extraction methods. Nevertheless, the cortical network has been described as a network with an isotropic layer of crosslinked filaments parallel to the membrane with mesh sizes of 20 - 250 nm (Charras et al., 2006; Medalia et al., 2002; Morone et al., 2006; Salbreux et al., 2012). Depending on the cell type estimations of its thickness ranges from 50 – 100 nm (Charras et al., 2006; Hanakam et al., 1996). The main cortical components are filamentous actin (F-actin) and bipolar non-muscular myosin II (MyoII) minifilaments, which serve as F-

actin crosslinker and active motor elements enabling filament sliding relative to each other at the expense of biochemical energy in terms of andenosine-5'-triphosphate (ATP). The resulting network, also referred as the actomyosin cortex, is a dynamic element by network contraction and relaxation (Fig. 3A).
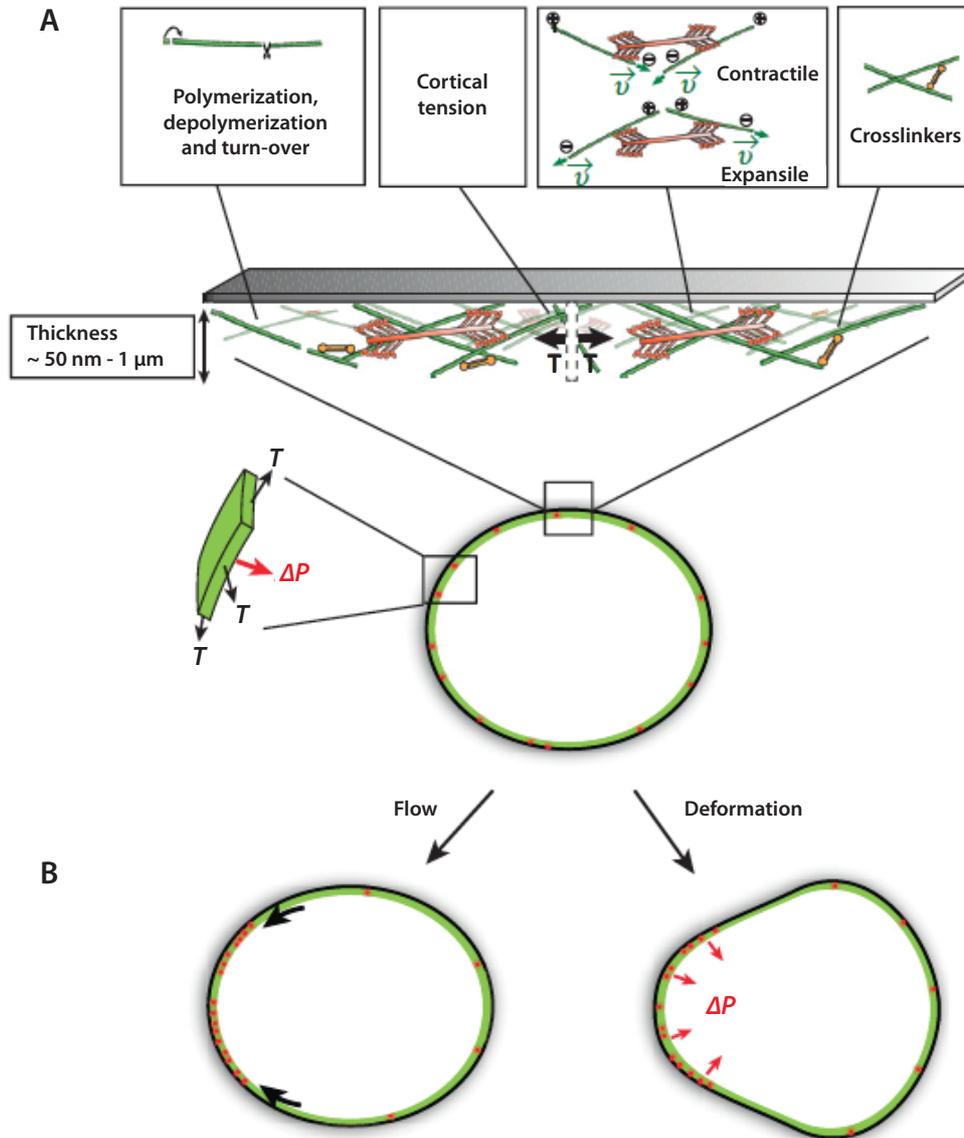
Figure 3. Cortex plasticity and tension. (A) Cortex tension (T) mediates eukaryotic animal cell shape and is the main determinant of cell stiffness. Actin filaments and myosin motors organize into a dynamic network that is able to contract or relax, thereby generating tension. Dynamics and plasticity of the cortical network is influenced by the regulated turnover of its components and the degree of crosslinking. (B) Cortical tension gives rise to a hydrostatic pressure (P) in the cytoplasm. Contractility gradients within the cortex can drive tangential flows of cortex in the plane of the membrane (left), but local contractions can also lead to cell deformations (right)(taken from (Salbreux et al., 2012)).

Other cortical components include that actin binding proteins α-actinin, fimbrin and filamin that are able to bundle and/or crosslink actin filaments, and tropomyosin and tropomodulin, which influence contractility. Since actin filaments arise from monomeric actin (G-actin), proteins that drive actin polymerization and contribute to cortex assembly are necessary. The actin nucleators of the formin family and the actin-related protein-2/3 (Arp2/3) complex are suggested to significantly take part in assembling the cortex although direct proof is yet missing (Eisenmann et al., 2007; Han et al., 2009; Hannemann et al., 2008; Roh-Johnson et al., 2012). The main proteic factors that mechanically link the cortex and the plasma membrane belong to the ezrin-radixin-moesin (ERM) family (Diz-Muñoz et al., 2010; Fehon et al., 2010). Hence, spatiotemporal regulation of the cortex components gives rise to a dynamic and plastic cortical network (Fig. 3) that orchestrates cell shape during cell division and migration.

Physical properties and dynamics of the cell cortex

The heterogeneous composition of the cortex appears as a gel-like functional entity exhibiting certain physical properties. The "superficial plasmagel" (Lewis, 1939) shows viscoelasticity, meaning elastic response at short time scales following viscous behaviour on time scales longer than the network turnover (Bray et al., 1986; Howard, 2001). The effective elastic modulus of the cortex depends on the actual cortex elasticity as determined by the inherent mechanical properties of the polymer network and the cortical tension governed by myosin-generated contractility (Salbreux et al., 2012). Cortex rearrangements and turnover render the cortex viscous. The dynamic remodelling of the cortex relies on the individual turnover of the cortex components such as F-actin and regulators of its polymerization or depolymerization, respectively, as well as network crosslinkers (Howard, 2001; Salbreux et al., 2012). Thus the spatiotemporal regulation of the viscous and contractile properties of the cortex result in a highly dynamic network, that allows for active control of the cell shape.

Cortex dynamics in cell migration

Myosin-driven contractile forces can actively modulate cortex tension. Local, non-uniform contraction of the cortex has been suggested to generate cortical flows along the plasma membrane towards regions of higher contractility and thus constituting the base for dynamic cell shape changes (Bray and White, 1988). Although these studies assumed that a gradient of cortical tension drives these flows, it was shown that for a viscosity-dominated cortex, it is rather the gradient of myosin contractility that drives the cortical flows and that cortical tension is reduced along the direction of flow. Hence, graded contractility results in anisotropies and not in gradients in cortical tension (Mayer et al., 2010). Actomyosin contractility can be locally regulated by both myosin activity and its distribution (Levayer and Lecuit, 2012). In addition, cortex kinetics can be affected by the spatial regulation of actin turnover, which governs its viscous behaviour (Mayer et al., 2010).

Several cell migration models are based on the dynamical modes of the cortex. One possible mechanism was derived from the discovery of antibody capping, which describes an

energy-dependent, actin-involving accumulation (cap) of crosslinked surface antigens at the cell rear of a migrating lymphocyte (TAYLOR et al., 1971). This phenomenon could be linked to rearward cortical movements along the plasma membrane, which in turn might drive membrane flows (Bourguignon and Bourguignon, 1984). Different models explain how the cortex flow can be transduced into a surface flow and ultimately into locomotion. They all converge in the idea that if rearward surface streams are to some extent coupled to the substrate, e.g. via transmembrane molecules, this will consequently result in forward movement of the cell (Bray and White, 1988; Bretscher, 1976; 2008; Hewitt, 1979). Since these models have not been directly tested yet, it is still not clear to what extent the underlying mechanisms contribute to locomotion (Bretscher, 2008).

One step in cell crawling that contributes to the net displacement of the cell involves the retraction of the cell body (Abercrombie, 1980). Whereas in mesenchymal migration the employment of stress fibres and the transduction of contractile forces to the substratum via focal adhesions mediate cell body retraction, amoeboid migration in 3D is ensured by cortical contraction alone. Local contraction in the posterior part of the cell squeezes the cell body including the nucleus forward (Lämmermann et al., 2008). Again spatially regulated myosin II activity is a basic module in the subsequent directed cell movement. Contractility gradients not only drive cortical flows, but can also lead to local contractions and cell deformations (Fig. 3B)(Salbreux et al., 2012).

As a consequence of contraction and cortex tension a hydrostatic pressure arises in the cytoplasm, which constitutes another migration mechanism. If the plasma membrane can locally separate from the actin cortex, the hydrostatic pressure rapidly bulges out the membrane forming a bleb (Charras et al., 2005; Trinkaus, 1973). This process, called "blebbing", can be exploited as a protrusive force that propels the cell forward: (1) local myosin contraction leads to a local increase in hydrostatic pressure and tension that can either cause cortex-membrane detachment (Charras et al., 2005; 2006) or rupture of the cortex (Paluch et al., 2005). (2) In both cases equilibration of the hydrostatic pressure causes a cytosolic flow from the cell body towards the membrane at the cortex-membrane breakage area resulting in a membrane bulge that is radially expanding. (3) Slowing and stalling of bleb growth is concomitant with the infiltration of cytoplasmic cortical components and subsequent cortex reassembly at the bleb membrane. (4) Bleb formation completes with the recruitment of myosin to the reforming cortical layer and myosin-governed cortex contraction finally leads to the retraction of the bleb (Fig. 4A)(Charras, 2008; Yoshida and Soldati, 2006). Blebbing can only be translated into movement if it occurs polarized and the forming bleb can be somehow linked to the substratum. Then, force can be exerted on it and cortex contraction at the rear entails retraction of the whole cell body and consequently leads to a net forward displacement of the cell. This can be achieved for example by weak adhesions with the substrate or by the application of a force perpendicular to the direction of movement through environmental confinement or entanglement with the matrix. Repetitive cycles of posterior contractions and daughter bleb formation on top of an existing bleb squeeze the cell forward (Fig. 4B)(Charras and Paluch, 2008).
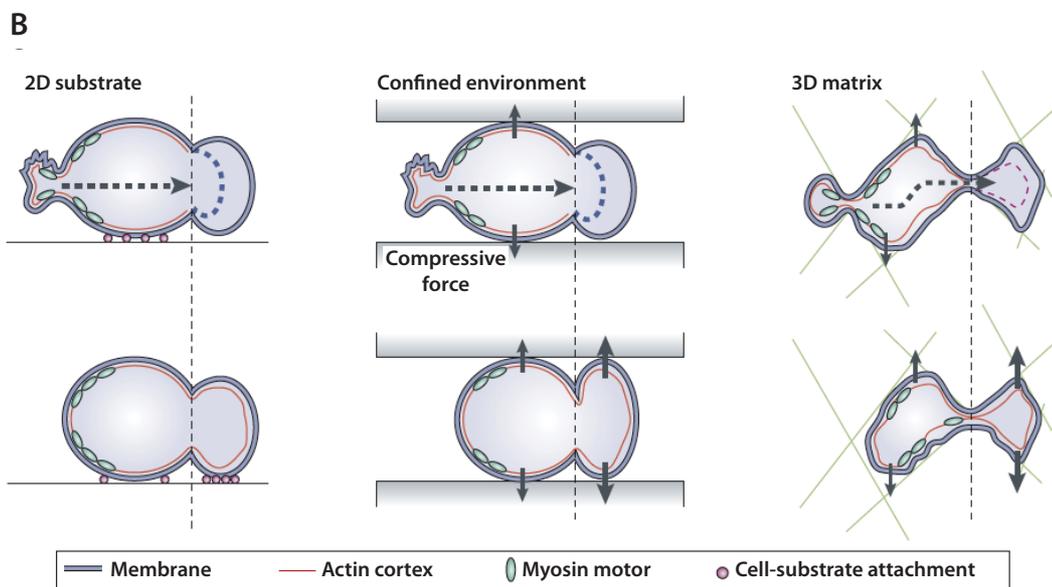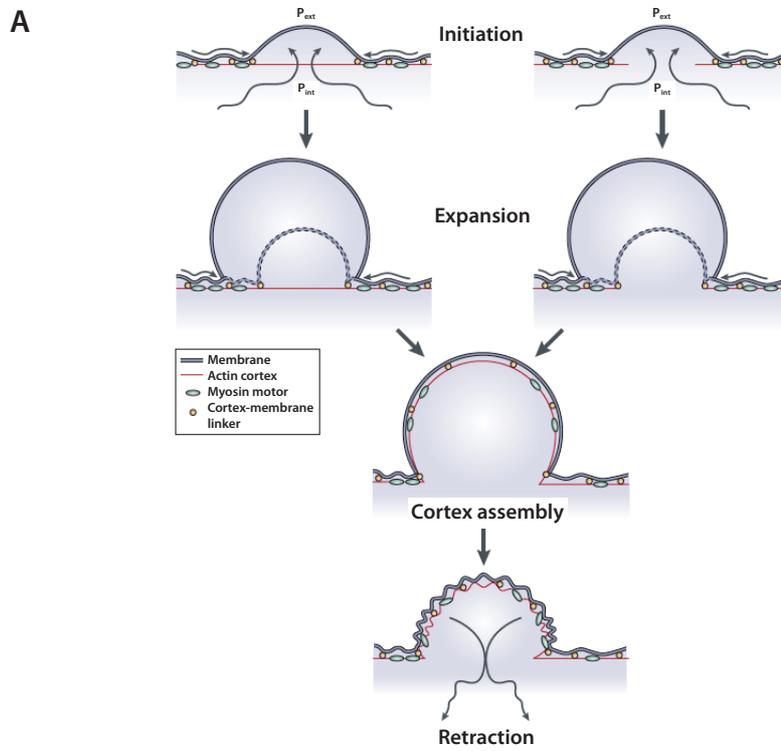
Figure 4. The cycle of a bleb and its translation into forward locomotion. (A) The initial step of blebbing requires the local separation of cortex and membrane. This can either be mediated by local cortex-membrane detachment or local rupture of the cortex. Then, the hydrostatic pressure (P_{int}) in the cytoplasm drives the formation of a radially expanding membrane bulge. With cumulative pressure equilibration, the bleb expansion slows down and a new actin cortex reforms under the bleb membrane. Recruitment of myosin to the new cortex is followed by bleb retraction. P_{ext}, extracellular hydrostatic pressure. (B) In order to translate polarized blebbing into movement the cell requires adhesion of the newly formed bleb to the substrate. In 2D this is mediated by concrete adhesion structures (left) whereas in confined environments the cell generates traction by exerting forces perpendicularly to the substrate and can squeeze itself forward (mid). In a complex 3D environment both mechanism can account for forward locomotion. The dashed line indicates the position of the leading edge before bleb nucleation, arrows indicate the forces that are exerted by the cells on the extracellular environment and dashed arrows indicate the streaming of cytoplasm (taken from (Charras and Paluch, 2008)).

Early hints that blebbing occurs were already made in the first half of the 20th (Hogue, 1919; Holtfreter, 1943) century and subsequent studies of Trinkaus and colleagues on *Fundulus* deep cells during embryo development indicated a link to locomotion (Fink and Trinkaus, 1988; Tickle and Trinkaus, 1973; Trinkaus, 1973; Trinkaus and Lentz, 1967). Follow-on observations on embryonic cell migration with bleb-like protrusions were described *in* and *ex vivo* for amphibian and fish (Fink and Trinkaus, 1988; KAGEYAMA, 1977; Kubota, 1981; SATOH et al., 1976), which could be later shown for chemotactic directed migration (Blaser et al., 2006). Similar findings were made for the chemotactic slime mould *Dictyostelium* (Langridge and Kay, 2006). Indeed, a cytoplasmic flow driven by hydrostatic pressure constituting a leading edge that is poor in filamentous actin during protrusion was described for several *amoebae* (Mast, 1926; Yanai et al., 1996) and therefore extends amoeboid cell migration (Friedl and Wolf, 2010). An amoeboid 'blebby' migration has also been suggested for tumour cells (Charras and Paluch, 2008; Yoshida and Soldati, 2006). In the absence of proteolytic matrix degradation bleb-like locomotion was shown to be used to invade and crawl through 3D matrices (Sahai, 2005; Sahai and Marshall, 2003; Wolf et al., 2003a). These studies were mainly performed using tumour cell lines and *in vitro* systems but to what extent this migration strategy is employed under physiological conditions remains largely elusive. Leukocyte amoeboid migration is largely considered to rely on actin polymerization-driven shape changes at the leading edge that generates the sufficient propulsive force required for forward translocation (Lämmermann and Sixt, 2009). A constriction-based cytoplasmic forward flow actuating bleb-like protrusions has been proposed during lymphocyte and neutrophil migration, but to what extent this observation is independent of actin polymerization at the membrane front could not be demonstrated (Bray et al., 1986; Haston and Shields, 1984). However, a pulsatile or oscillatory mechanism, in which myosin-contraction facilitates membrane detachment and supports subsequent actin polymerization at the leading edge is conceivable (Levayer and Lecuit, 2012; Yoshida and Soldati, 2006). This is consistent with studies on contractile forces during dendritic cell and T cell migration in a confined setup and argues for the contribution of myosin II-directed hydrostatic forces on fast amoeboid migration (Faure-André et al., 2008; Jacobelli et al., 2009). Interfering with actin polymerization in DCs by low dose latrunculin B treatment results in protrusive

blebbing, but to which extent this finding underscores the aforementioned model or if it is an epiphenomenon remains to be shown (Lämmermann and Sixt, 2009).

Symmetry breaking and cell polarization during cell migration

The prerequisite for a cell before any migration event can occur is polarization, or in other words the definition of its front and back. Cell polarization involves symmetry breaking and the establishment of an anterior-posterior axis, which is achieved by (1) the asymmetric distribution of cellular components and (2) the inherent polarity of proteins. Induction of cell polarity that allows for migration can be either directed by exogenous asymmetric spatial signals or can occur randomly as a consequence of stochastic fluctuations of polarity proteins (biochemical instability) intrinsically amplified by positive feedback loops (Sohrmann and Peter, 2003; Wedlich-Söldner and Li, 2003). Environmental factors initiating polarization can be gradients of soluble (chemotaxis) or immobilized (haptotaxis) chemoattractive cues. These exogenous heterogeneities in chemoattractant concentrations can be translated into intracellular asymmetries via unequal receptor occupation across the cell. This leads to the localized recruitment and activation of signalling cascades within the cell, finally generating a morphological and functional cell asymmetry (Chung et al., 2001).

Mechanisms of symmetry breaking

A polarized migrating cell can be morphologically distinguished by a distinct protruding cell front and a trailing cell back, also referred to as uropod. On the mesoscopic scale, polarity is established by several cellular system, involving the distribution of both cytoplasmic proteins and receptors, cellular networks and compartments, and vesicle transport in endocytic-exocytic loops (Fig. 5A)(Krummel and Macara, 2006). In addition, the discontinuous organization of distinct plasma membrane microdomains with different potentials to recruit and to serve as assembly platforms for specific signalling components can contribute to the compartmentalization of signalling pathways (Gómez-Moutón et al., 2004; Ibáñez, 2004).

Molecular asymmetry of cytoskeletal molecules

The structural basis for most of these polarization systems relies on the inherent polarity of cytoskeletal components, namely the actin filaments and microtubules. The consequent head-to-tail association of their intrinsically asymmetric monomers, in turn establishes the polarity of these polymers by forming two distinct ends. The incorporation and hydrolysis of ATP to ADP in the case of G-actin, and GTP to GDP for tubulin monomers, respectively, additionally contributes to asymmetries along the polymers. In particular, it affects polymer dynamics (described more precisely in the following chapter) by influencing the affinity of the monomers to each other resulting in different association-dissociation rates at the polymer ends. Thus, the intrinsic orientation of a filament coupled with differing polymerization rates at its poles gives rise to a dynamic asymmetrically behaving molecular machinery that, if the polymers are assembled into organized arrays, is able to generate cellular asymmetry (Fig. 5B)(Li and Gundersen, 2008).
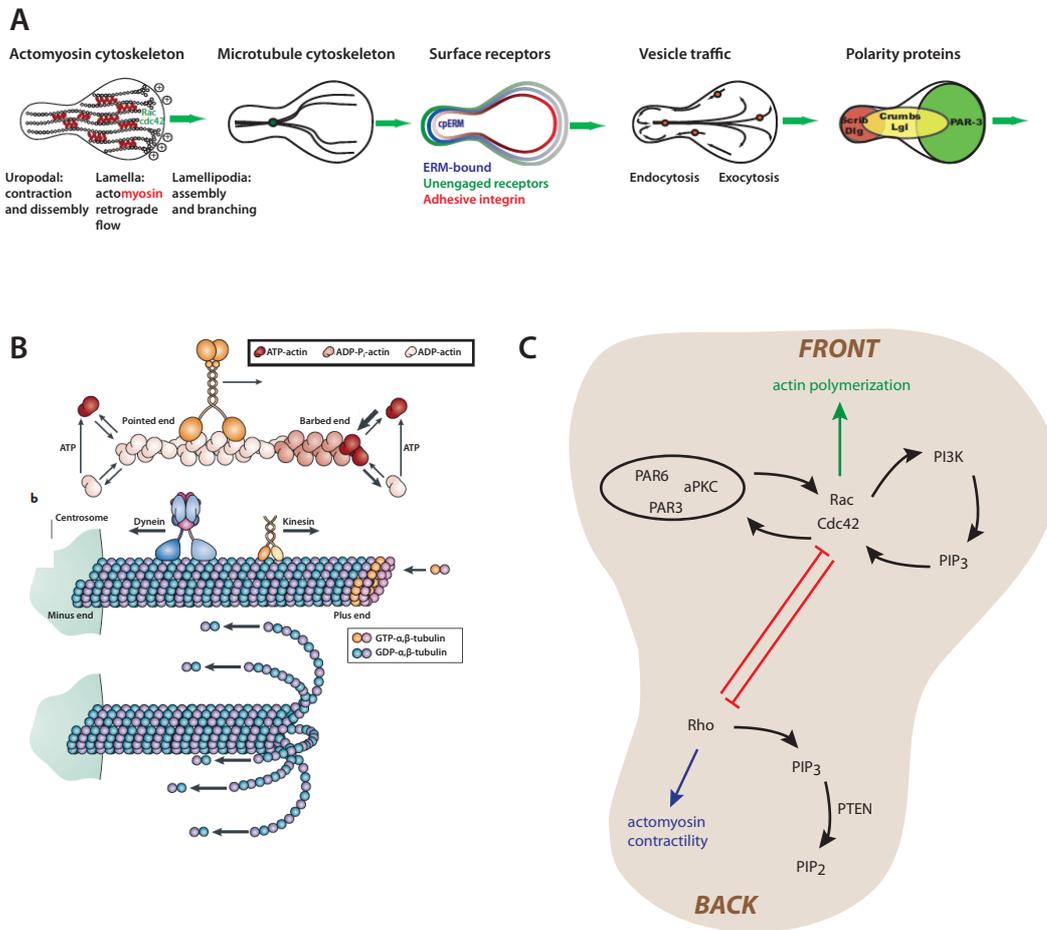
Figure 5. Mechanisms of symmetry breaking. (A) Polarity is established by several cellular systems: structure and distribution of the actin cytoskeleton; orientation of the MTOC and microtubules; distribution of surface receptors and polarity proteins; direction of vesicle transport/endocytic-exocytic loop (taken from (Krummel and Macara, 2006)). (B) Molecular asymmetry of cytoskeletal filaments: both actin and tubulin monomers exhibit an inherent polarity. Due to constant head-to-tail associations of the monomers their polymerization results in bipolar filaments. Additionally, asymmetry is enforced by different association-dissociation rates at both filament ends. The structural asymmetry of both filaments is employed to promote progression of symmetry-breaking through other cellular system, e.g. unidirectional movement of motor proteins along the filaments or the generation of distinct actin networks through varying filament orientations relative to each other (taken from (Li and Gundersen, 2008)). (C) Signalling loops and crosstalk enforcing cell polarity: The cell front-defining GTPases Cdc42 and Rac. Both are incorporated in signal amplifying feed forward loops and drive actin network expansion towards the prospective leading front. A Rho-driven actomyosin network establishes the cell's back. Cross-inhibition of the "front"- GTPase Rac and the "back-" GTPase Rho additionally ensures asymmetry. The spatially distinct activity of the antagonist pair PI3K at the leading edge and PTEN at the uropod, respectively, generates a PIP$_3$ gradient from front to back that supports the maintenance of a stable polarization.

Translating molecular to cellular polarity

The structural polarity and dynamics of the cytoskeleton is the base to drive the progression of symmetry-breaking or to maintain polarity through other cellular components (Li and Gundersen, 2008). Molecular motor proteins from the myosin superfamily, kinesins and dynein can bind to and move along these organized filament arrays and use them as tracks for cargo transport. Exhibiting unidirectional movement along a filament, motor proteins can specifically traffic and target their cargo molecules or organelles, thereby contributing to their unequal distribution across the cell (Fig. 5B). Again, it is an inherent property of these proteins that constitutes symmetry breaking on a cellular level. However, also nonpolar proteic polymers have been shown to contribute to the establishment of polarity. The septin cytoskeleton has been shown to play a role in the establishment of polarity. By the interaction with both, the membrane and the actomyosin network, the spatially restricted engagement of septins locally influences cortical rigidity and membrane curvature. Direct binding of septins to myosin suggests a role for septins in regulating actomyosin dynamics. Through their interaction with microtubules they may participate in the regulation of directed vesicle transport, thereby contributing to the asymmetric distribution of cargo proteins and lipids (Gilden and Krummel, 2010).

Organisation of distinct actin networks in front and back

The central determinant of cell migration is the mechanical asymmetry between the cell's front and back. Both, the protrusive force of the leading edge and the contractile forces needed for uropod retraction rely on the inhomogeneity of the actomyosin cytoskeleton along the migration axis. On the actin level, the assembly of filament arrays need to be directed towards the leading membrane to generate a protrusive front, whereas in the rear of a cell filaments are organized more in an anti-parallel manner that can be moved against each other by myosins to mediate contractility. Myosin II processively participates in the orientation of actin filaments and can also stabilize and bundle them. Local myosin activity or weakening of the actomyosin network can lead to a global anisotropic contractile response and affects the distribution of polarity proteins, hence driving symmetry breaking (Li and Gundersen, 2008).

Polarized signalling drives and maintains symmetry breaking

These mutually exclusive actomyosin networks are generated following a polarized signal. Irrespective of the polarization induction happened extrinsically or intrinsically, the signal is amplified by local feed forward loops and global cross-inhibition (crosstalk) to proceed symmetry breaking and maintain polarization. The signalling pathways include the small GTPases Rho, Cdc42 and Rac, whose balanced temporal and spatial activities are essential for the polarization process. GTPases cycle between an active GTP-bound and an inactive GDP-bound state regulated by a myriad of guanine nucleotide-exchange factors (GEFs) and GTPase-activating proteins (GAPs). Locally increasing activation of the small GTPases Rac and Cdc42 defines the cell's front and leads to the formation of a highly dynamic actin network extending and expanding towards the prospective leading membrane (Itoh et al.,

2002)(Fig. 5C). Cdc42 is considered to be the "master regulator of cell polarity" targeting several pathways to establish polarity (Etienne-Manneville, 2004; Johnson, 1999). Altered activity and localization does not affect protrusion formation and migration *per* se, but interfered with the protrusion stability and migration directionality (Allen et al., 1998; Etienne-Manneville and Hall, 2002; Lammermann et al., 2009; Srinivasan et al., 2003). Despite its function in coordinating actin polymerization at the leading edge, it also controls the positioning of the microtubule-organizing centre (MTOC) and the Golgi apparatus, thus aligning the microtubule-mediated delivery of vesicles and cargo proteins needed for leading edge stabilization and progression. Interestingly, localization of Cdc42 itself relies on that directed vesicle trafficking (Osmani et al., 2010), thus promoting its own distribution to the cell front. It also controls the recruitment of PAR3, PAR6 and atypical protein kinase C (aPKC), members of the partitioning-defective (PAR) polarity proteins, to the leading front, which in addition contributes to the polarization of the microtubule cytoskeleton and MTOC orientation (Etienne-Manneville and Hall, 2003). Rac activity is essential for localized actin polymerization at the protrusive front (Nobes and Hall, 1999). It has been shown that in fast migrating cells, such as leukocytes and *Dictyostelium discoideum*, loss of function crucially impairs polarization and directional migration towards a chemoattractant source (Park et al., 2004; Srinivasan et al., 2003). In contrast, the key GTPase bringing up the cell's rear is Rho. Its posterior activity accounts for both, the organization and contraction of the uropodal actomyosin network (Fig. 5C).

Signalling crosstalk enforces polarity
In order to retain a stable polarization, the cell needs to maintain the asymmetric GTPase activity along the migration axis. This is achieved by a reciprocal inhibition of active Rac and Rho, suppressing each other's activity and ensuring the mutually exclusive actomyosin structure of the front and back (Evers et al., 2000) In addition, several local positive feedback loops serve as signal amplifiers to guarantee for sustained GTPase activity and allows polarization even in the presence of small signalling differences along the anterior-posterior axis. Another major determinant of 'frontness' is the asymmetric accumulation of phosphatidylinositol (3,4,5)-triphosphate (PtdIns(3,4,5)P_3 or PIP$_3$) generated by locally active phosphoinositide 3-kinases (PI3Ks) at the leading edge. The antagonist of PI3Ks acting at the cell's rear is the phosphatase and tensin homologue (PTEN). There, it hydrolysis and removes PIP$_3$ resulting in a PIP$_3$ gradient from front to back. Although neither PI3K nor PTEN are necessary for locomotion, their coordinated activity seems to be crucial for directional migration during chemotaxis (Cain and Ridley, 2009; Kölsch et al., 2008). PIP$_3$ regulates the protrusion dynamics by directing the corresponding signalling clusters and the actin polymerization machinery towards to leading edge. The mutual recruitment and activation of the anterior GTPases Cdc42/Rac and the PI3Ks generates a feed forward loop that results in signal amplification and prolonged polarization (Fig. 5C).

Gradient sensing during chemotaxis

Leukocyte function depends on the ability to react on chemoattractant (or chemorepellent) cues with polarization and directional migration towards (or away from) its source. Hence, the cell needs a system that is able to detect, interpret and respond to extracellular chemical gradients. Whereas bacterial gradient sensing relies on the temporal comparison of chemokine differences, two hypotheses have been proposed for eukaryotic chemotaxis: temporal sensing as employed by bacteria and spatial sensing, which is based on perceiving concentration differences along the cell perimeter (Lauffenburger et al., 1988; 1987; Vicker, 1989; Vicker et al., 1986). Models of eukaryotic gradient sensing seem to favour the spatial model as the primary mechanism, but temporal sensing is still discussed and cannot be excluded. In both models, the cell needs to sense the outside stimulus, transduce the signal to the inside, process the information and respond to it. For the spatial interpretation of a gradient the cell needs to compare and integrate signalling events across the cell to finally initiate polarization and migration according to the gradient direction.

The initial step in gradient sensing is carried out by receptors that convert extracellular ligand binding to an intracellular signal. The predominant receptors belong to the family of the G-protein coupled receptors (GPCRs). This class of receptors exhibits an extracellular N-terminus and an intracellular C-terminus, which are connected by seven helical transmembrane domains. Their intracellular loops and the C-terminus form the signalling domain and bind to corresponding heterotrimeric G-proteins ($G_{\alpha\beta\gamma}$). Receptor ligation induces conformational changes and promotes the exchange of GDP with GTP in the GTPase domain of the G_α subunit of the heterotrimeric G-protein. This results in the separation of the G_α and the $G_{\beta\gamma}$ subunits followed by G_α release from, as well as $G_{\beta\gamma}$ release at the plasma to their downstream effectors (Fig. 6)(Wettschureck and Offermanns, 2005).
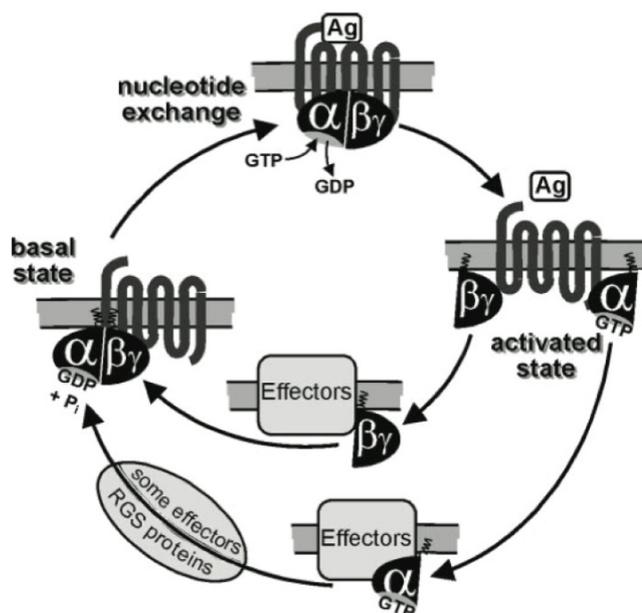
Figure 6. G-protein coupled receptor (GPCR)-mediated signal transduction. (A) Binding of its ligand to the extracellular N-terminus and loops of the GPCR induces intramolecular conformationnal changes that promote the release of GDP from the α-subunit of the heterotrimeric G protein resulting in the formation of GTP-bound G_α. This triggers subsequently the dissociation of the GTP-G_α and $G_{\beta\gamma}$ subunits and enables their effector functions. The intrinsic GTPase activity of the α-subunit hydrolysis GTP to GDP and P_i is released. GDP-bound GTP-G_α then reassociates with $G_{\beta\gamma}$. The spontaneous hydrolysis of GTP to GDP can be accelerated by various effectors as well as by regulators of G protein signalling (RGS) proteins (taken from (Wettschureck and Offermanns, 2005)).

In order to read a spatial gradient and/or its temporal changes in chemokine concentrations those receptors are uniformly distributed along the plasma membrane(Servant et al., 1999; Xiao et al., 1997). Only this receptor distribution guarantees an equal sensitivity along the cell perimeter and the external signals can be analogously transduced to the inside of the cell by translating the extracellular heterogeneities of chemoattractant concentrations into a polarized distribution signalling modules and a cellular polarized response. To detect even shallow gradients (1-2 % concentration differences between front and back) this translation does not occur in a linear fashion. It rather results in a qualitative readout meaning that small external differences are converted to a fairly strong redistribution of intracellular signalling modules. Several gradient sensing models emerged from experimental and computational studies trying to elucidate the underlying molecular mechanisms and many of them are based on a local excitation, global inhibition (LEGI) principle (Fig. 7A): receptor occupancy results in an immediate production of a local activator and a delayed locally generated but globally acting inhibitor (Devreotes and Janetopoulos, 2003). Thus, receptor ligation according to the external gradient results in a corresponding graded accumulation of the activator and a more uniformly distributed inhibitor across the cell. Only in the focal area of highest receptor ligation the local excitation exceeds the inhibition. Vice versa, the inhibitor dominates the activator at the opposite pole (Swaney et al., 2010). In addition, spatially restricted local positive feedback loops are proposed to amplify the signalling readout. As a consequence, the shape of the signalling response is rather independent of the extracellular gradient steepness(Iglesias and Devreotes, 2008).

Another model rather neglects the translation of the external gradient into an internal signalling polarity that is amplified and self-maintained by positive feedback loops (Fig. 7B). It points more to the inherent capability of polarization that is entirely decoupled from the gradient sensing. A polarized cell then senses and responds to an exogenous gradient by a biased protrusion extension due to enhanced receptor signalling at the side closer to the chemoattractant source within an existing leading edge. Therefore, gradient sensing might not be an integrative but stochastic process and the result of local coupling of receptor signalling events to local protrusion extension. The cell gradually aligns its polarity axis and migration direction to the gradient (Arrieumerlou and Meyer, 2005). In both models the central compass parameter is PIP_3 (and its associated signalling modules). Whereas in the LEGI model its redistribution across the cell reflects the sensed gradient, the local coupling model attributes it a dual role: global self-polarization and biasing leading edge extension. None of these models can explain and integrate the observed gradient sensing response during chemotaxis completely. But in either case, gradient sensing and motility have been shown to be independent processes and their coalescence is fundamental for chemotaxis.

A central conundrum in gradient sensing, which has not been completely understood to date, is how the cell stays sensitive towards changing gradients while prolonged receptor occupancy and continuous downstream signalling is ongoing. Therefore, the cell employs mechanisms to adapt signalling strength and length. Adaption can be achieved by the concomitant activation of negative feedback loops temporally restricting or quenching the

excitatory signal (Swaney et al., 2010). In addition, it can already occur directly at the stimulus entry site, designated as receptor desensitization. Receptor desensitization can be accomplished by the biochemical and steric inhibition of G-protein coupling by G protein receptor kinases (GRKs) and β-arrestin, as well as ligand-binding induced clathrin-dependent receptor internalization (Lefkowitz and Whalen, 2004; Premont et al., 2004). Subsequent endosomal ligand degradation, the latter can lead to receptor recycling and resensitization at the plasma (Otero et al., 2006). Adapting to prolonged stimulation ensures sensitivity over a wide range of concentration differences and temporally changing gradients.
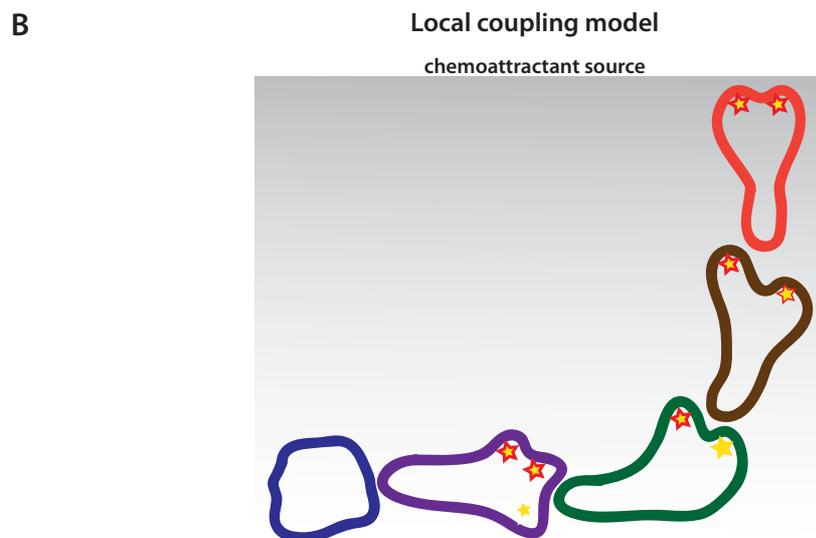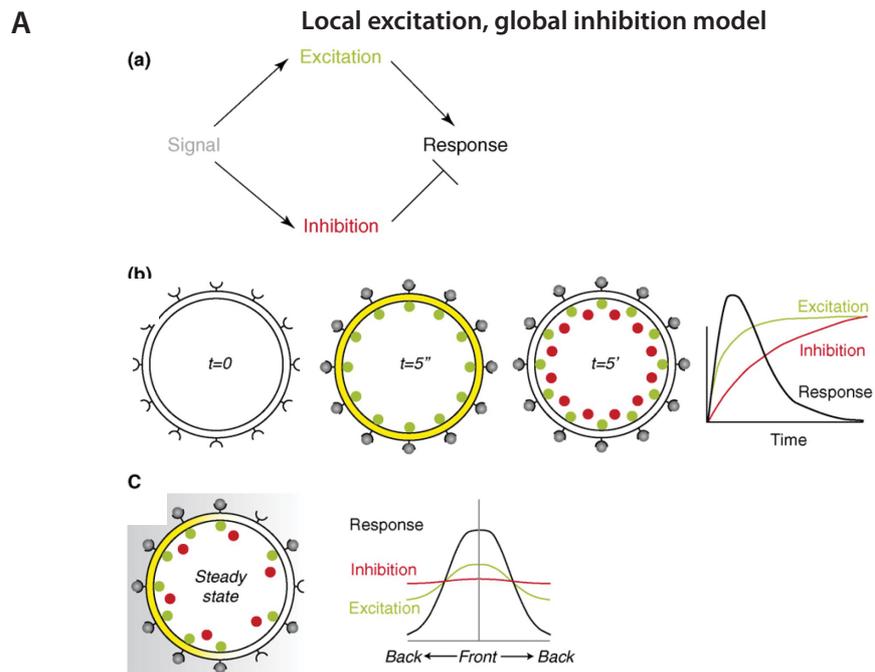
Figure 7. Gradient sensing models. (A) Local excitation, global inhibition (LEGI) model of gradient sensing: a chemotactic stimuli induces both a rapid, local excitor (green dots), as well as a slower, global inhibitory response (red dots)(upper and mid panel). After uniform stimulation, fast excitation (e.g. t = 5s) is followed by its quenching by the slower inhibitor (e.g. t = 5 min) and the combinatory effect results in a transient response. Because the stimulus is spatially uniform, the distinction between local and global disappears (mid panel). In a gradient, the excitatory signal exceeds the inhibitor at the side of high stimulus concentration, whereas inhibition cancels out excitation at the side of low stimulus concentration. The slower acting inhibitory signal is strongly influenced by diffusion, thus equilibrating across the cell. This results in an overall stronger response at the front than at the back (lower panel)(taken from (Iglesias and Devreotes, 2008)). (B) Local coupling model: this model assumes a successive alignment of the cell towards the gradient as a result of biased protrusion formations at the side of higher chemokine concentrations.

Subcellular structures and their actin cytoskeletal organization at the leading edge of migrating cells

The highly dynamic behaviour and constant reorganization of the actin cytoskeleton is the basis for both intracellular processes that involve directed movement of molecules and vesicles, and cell migration *per se*. Depending on the organization of the actin filament network, distinct protrusive structures can be distinguished by their differential use and requirement for locomotion.

Lamellipodia and lamella

The term "lamellipodium" was coined in the 1970s as the most distal portion of the front of a migrating cell(Abercrombie et al., 1970). It is a flat, sheet-like membrane protrusion constituted of a dense mesh of filamentous actin. Characteristically, lamellipodia are 1-3 μm in width, 100-300 nm thick and devoid of organelles. Branched and short actin filaments dominate the lamellipodium showing high polymerization and depolymerization rates resulting in a confined band of F-actin treadmilling (see following chapter)(Chhabra and Higgs, 2007). The orientation of the fast growing barbed ends towards the leading membrane provides the protrusive force for lamellipodium expansion. Filament polymerization occurs by actin monomer addition between the barbed ends and the membrane interface. This outward pushing against the stiffness of the membrane gives rise to a centripetal counterforce resulting in the backsliding of the filaments, observable as a retrograde flow of F actin. Thus, a high polymerization rate results in a high retrograde flow. Linking retrograde flow to the ECM via integrins translates into forward movement, and net protrusion depends on the linkage efficacy. Lamellipodium advance is not a monotonous unidirectional process but the outcome of phases of protrusion, pause and retraction, associated with differently oriented populations of actin filaments. Protrusion phase features predominantly pointed angles between the actin filaments and the membrane front, whereas filaments get more parallelised to the leading edge during pause and retraction (Bear et al., 2000; Burnette et al., 2011; Giannone et al., 2007; Koestler et al., 2008). Shifting the angles could be possible mechanism to tune protrusion rate while filament density stays unchanged.

Lamellipodia function is controversial since cells are still able to migrate in the absence of lamellipodia (Gupton et al., 2005). Their major task might be in the rapid response towards
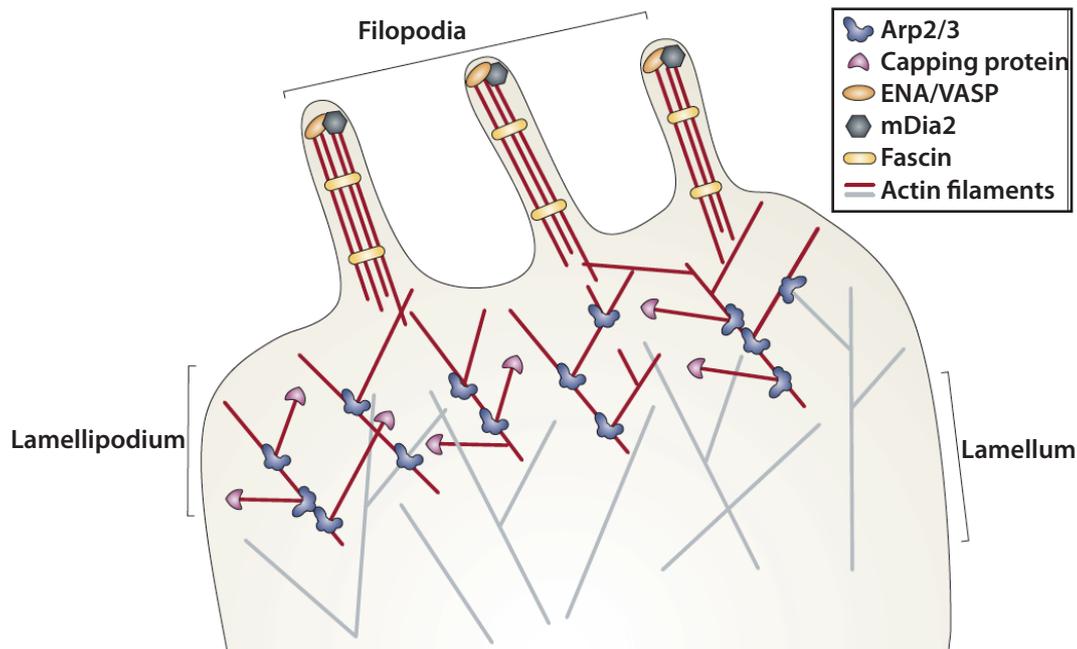
Figure 8. Actin-based subcellular structures of the leading edge. Top view of lamellipodium, lamellum and filopodia. A branched and disordered network of actin filaments characterizes the sheet-like lamellipodium. Its generation and dynamics rely on the coordinated interplay of several actin nucleators including the actin brancher Arp2/3 complex, as well as barbed end-binding proteins that modify filament elongation rate. Orientation and polymerization of actin filaments towards the membrane generates a protrusive force. The lamellum describes the F-actin network just behind the lamellipodium. It appears less dense and contains longer filaments than the lamellipodium. Formation of focal adhesions and the action of myosin II provide a contractile network that makes the lamellum a functionally distinct zone. The finger-like filopodia contain long and parallel crosslinked actin filaments. As in the lamellipodium, barbed end orientation towards the membrane generates a protrusive force. Filopodia can be formed from lamellipodial F-actin but does not rely on Arp2/3 activity (taken from (Heasman and Ridley, 2008)).

directional cues and environmental exploration. The formation and stabilization of lamellipodia was correlated with directionally persistent migration (Harms et al., 2005).

The lamellum extends just behind the lamellipodium towards the cell body and displays the second part of a leading edge. It is thicker (>200 nm), occupies a wider band (10-15 μm), but contains longer and fewer branched filaments than the lamellipodium. Moreover, the lamellar actin network is dynamically and functionally distinct. In addition to the criss-crossed actin mesh pointing towards the leading membrane, it comprises bundled filaments, myosin II (and tropomyosin) and focal adhesions, hence providing a contractile network for traction (Fig. 8)(Cai et al., 2006). A less pronounced actin turnover and actomyosin-based contraction drives a rather slow retrograde flow in the lamella (Ponti et al., 2004). Due to actin network stability and coupling to the substrate the lamella is thought to have a major function in leading edge advance and the net cell translocation (Gupton et al., 2005; Ponti et

al., 2004). To what extent two actin networks are independently established and mechanically connect to mediate cell migration is still controversial. There is evidence that filaments and branches "born" in the lamellipodia are gradually dragged back to the lamella during forward movement, reorganized and incorporated into contractile structures (Burnette et al., 2011; Vinzenz et al., 2012). Furthermore, in mesenchymal migration, lamellipodial and lamellar zones particularly differ in their integrin-mediated adhesiveness. Adhesion required for traction is initiated in the lamellipodium as low adhesive small nascent focal complexes (Vicente-Manzanares et al., 2009). Unless undergoing turnover they mature into elaborate long-lived focal adhesions beginning at the lamellipodium-lamellum boundary. Thus, lamellipodia and lamella are distinct structures that are functionally interrelated.

To date the existence of the distinctive nature of these two leading edge modules in leukocyte amoeboid migration has not been explicitly shown. Observations on T cell migration led to the separation of the dynamic leading edge with a rather loose adhesiveness and a mid-cell focal zone containing high affinity integrins binding to the substratum, similar to focal adhesions in the lamella (Smith et al., 2005; Stanley et al., 2008). Since these studies were performed using 2D substrates, it is doubtable to assume a focal zone in 3D migration, in which integrin-mediated traction is dispensable (Lämmermann et al., 2008). Observations of our group on DC migration show a retrograde flow that is not limited to the narrow distal zone of the leading edge but continues far into the cell body (Renkawitz et al., 2009). These findings would rather suggest an extended lamellipodium or an actomyosin cytoskeletal continuum covering the whole leading edge.

Filopodia

As lamellipodia, filopodia are actin polymerization-driven structures at the leading front of a migrating cell. Appropriately described as finger-like protrusive structures, they are typically 0.1 - 0.3 μm in width and their length can range from 10 μm to 40 μm (Mattila and Lappalainen, 2008; Welch and Mullins, 2002). They are filled with long parallel crosslinked actin filaments organized into densely packed bundles. The unipolar orientation of the fast growing barbed ends of the filaments towards the plasma membrane results in filopodia growth and ultimately promotes cell extension and contributes to migration. Filopodia growth or retraction are controlled by shifting the balance between polymerization rate at the filopodial tip and retrograde flow (Mallavarapu and Mitchison, 1999). Furthermore, filopodial actin bundles can be formed and extended by the alignment and reorganization of the filaments within the lamellipodial meshwork (Fig. 8). However, a lamellipodial actin network is not strictly required for filopodia formation (Steffen et al., 2006). In contrast to the lamellipodium, they do not build up the whole leading edge, but multiple filopodia can emanate from a lamellipodial sheet. Thus, filopodia and lamellipodia coexist. Moreover, it has been shown that filopodial actin bundles can be recycled in contractile structures of the lamella: (1) two filopodia laterally folding back in opposite directions and aligning within the cell edge can give rise to a contractile actin bundle with antiparallel filaments. After myosin incorporation, (2) fragmented bundles or filaments are found reused in lamellar adhesive

structures (Nemethova et al., 2008).

Compared to lamellipodia, filopodia alone cannot drive motility and their function during cell migration seems to be diverse. Nonetheless, filopodial protrusions are employed for cell guidance along a gradient, as well as cell-matrix and cell-cell adhesions, hence enhancing efficient directed migration. By localisation of adhesion molecules, e.g. integrins or cadherins, to their tips, filopodia can function as "sticky fingers" probing the environment for adhesion sites (Galbraith et al., 2007; Partridge and Marcantonio, 2006; Steketee and Tosney, 2002). Increased filopodia formation has also been correlated with cancer cell invasiveness (Vignjevic et al., 2007). In macrophages filopodia are used as "cellular tentacles" for pathogen capture, followed by filopodia retraction and pathogen phagocytosis (Kress et al., 2007; Vonna et al., 2007).

In summary, filopodia act as exploratory and sensory protrusions promoting migration. Their dynamics, length, number, as well as their position vary significantly between cell type and/or environmental conditions.

Lobopodia

Another type of cellular protrusions observed in some eukaryotic cells are lobopodia. Characteristically, they appear as blunt, cylindrical protrusions, sometimes accompanied with multiple small lateral blebs (Friedl et al., 2001; Yanai et al., 1996). Compared to solely actin polymerization based protrusions as lamellipodia and filopodia, lobopodial protrusions rely on an actomyosin-driven intracellular pressure (Yanai et al., 1996). But in contrast to blebs, lobopodia can still form focal adhesions and stress fibres. Lobopodia formation could be recently linked to the mechanical rigidity of the environment (Fig. 9). In human fibroblasts, depending on the elastic behaviour of the ECM lobopodial or lamellipodial migration was triggered (Petrie et al., 2012).

Figure 9. Lopopodial migration of fibroblasts. Lobopodia show an intermediate mechanism of lamellipodial and bleb-like migration. Lamellipodia formation relies on the formation of a protrusive actin meshwork (blue), as well as polarized PIP$_3$, Cdc42, and Rac activation. In fibroblasts 2D migration employs focalized integrin-mediated adhesions with associated RhoA-driven stress fibers to generate traction. Lobopodia exhibit blunt-end protrusions with many myosin driven small lateral membrane blebs , which require RhoA activity but no polarized Rac, Cdc42, and PIP3. Compared to bleb-based migration, Lobopodia employ focalized adhesions and stress fibers. Lobopodia have only been found in 3D migration and depend on the elastic properties of the ECM (taken from (Sixt, 2012)).
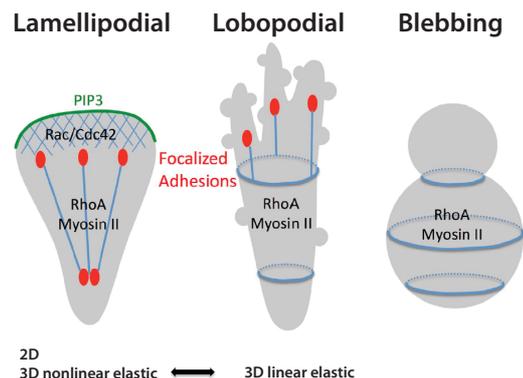
The generation of protrusive actin networks

Cellular mechanisms of actin polymerization

Actin is synthesized as a 43-kDa globular protein (G-actin) and expressed throughout all cell types in eukaryotes. Enzymatically, actin is an ATPase hydrolysing ATP to ADP and inorganic phosphorous (P_i). To fulfil its mechanical function it is assembled into filamentous helical structures (F-actin) via polymerization, a process that does not involve ATP hydrolysis. Actin polymerization can be subdivided into actin nucleation and elongation. Nucleation requires the formation of a stable nucleation core containing three actin monomers. Once a stable core has formed, filament elongation and growth is achieved by monomer addition. Since filament assembly is a reversible, non-covalent reaction, depolymerization can occur and result in filament shrinkage. The constant actin filament turnover by repetitive cycles of polymerization and depolymerization is the base for actin dynamics, which is in turn the prerequisite for protrusive force generation required for most cell migration modes.

Actin treadmilling: the base for actin dynamics and remodelling

The inherent polarity of G-actin and its consistent incorporation into a growing filament in the same orientation leads to a structurally polar filament. This bipolarity is accompanied by distinct actin subunit binding dynamics at each end, resulting in a filament comprising a fast growing plus (+), or barbed end, and slow growing minus (-), or pointed end. In addition, depending on the actin-bound nucleotide, the monomer binding affinity towards neighbouring subunits is affected. At a given monomer concentration, an ATP-actin monomer adds with a higher binding rate to a growing filament than the ADP-bound form. At steady state, the quantity of actin monomers binding to and dissociating from one filament end is equal, and the corresponding monomer concentration is termed critical concentration. The aforementioned characteristics of the filament end dynamics and the binding affinities of nucleotide-bound G-actin lead to a barbed end having a lower critical concentration than the pointed end. At a concentration between the two critical concentrations of both ends, filament polymerization occurs at the barbed end while depolymerization is taking place at the pointed end. Since the hydrolytic activity of actin towards ATP is a rather slow but irreversible process compared to the binding rates, filament turnover under physiological conditions is as follows: an ATP-actin binds at the growing filament's barbed end. As monomer addition is ongoing it is gradually shifted towards its pointed end. While shifting, ATP is hydrolysed and ADP-actin is released at the pointed end (Fig. 10A). This mechanism, designated as actin treadmilling, determines actin dynamics at physiological conditions.

Actin nucleators assemble linear F-actin

Since the clustering of three actin monomers is a kinetically unfavourable process, several actin nucleators are employed by the cell to initiate actin filament assembly (Fig. 10B). The

most studied and best-characterized actin nucleators producing linear filaments are the formins. Formins catalyse both actin nucleation and elongation. In general, they are constituted by highly conserved formin homology (FH) domains, namely FH1 and FH2, and obtain their function as homodimers. Based on their FH2 divergence the 15 mammalian formins are classified into seven subclasses: Diaphanous (DIA), formin-related proteins in leukocytes (FRLs), Dishevelled-associated activators of morphogenesis (DAAMs), formin homology domain proteins (FHODs), formins (FMNs), dolphin and inverted formins (INFs) (Higgs and Peterson, 2005). Studies working with purified FH2 domain could show its ability to dimerize, forming a donut-shaped ring that is sufficient to nucleate actin *in vitro*. Lacking a discrete monomer-binding domain, FH2 hemidimers are thought to stabilize spontaneously formed actin dimers. Association of two FH2 domains then results in the clustering of four actin monomers and the formation of a stable nucleation core. The kinetic barrier of nucleation is overcome and polymerization can continue. In addition to its nucleation function homodimeric formins can act as processive motors for filament elongation (Romero et al., 2004; Watanabe and Higashida, 2004). Alternating contacts of the FH2 monomers with two terminal actins of the barbed end and actin monomer recruitment and delivery, e.g. profilin-actin, by the corresponding FH1 domain drives and accelerates actin polymerization compared to diffusion-limited growth. Hence, the homodimer remains with the barbed end competing with and protecting it from elongation termination by barbed end capping proteins.

Formins are employed for the assembly of diverse cellular actin structures, particularly those based on long parallel networks. Their necessity for migration and their major contribution in the formation of filopodia and stress fibres has been shown. An unbalanced formin activity could be linked to disease progression through enhanced cell motility, promoting invasiveness and metastasis in tumour spreading, as well as myeloproliferative defects leading to immune diseases. Defective expression of the formin mDia1 affects polarization, chemotaxis and trafficking to secondary lymphatic organs in T cells and neutrophils (Eisenmann et al., 2007; Sakata et al., 2007; Shi et al., 2009). Beside impaired directional migration along chemotactic gradients *in vivo*, loss of mDia1 in DCs compromises adhesion and T cell stimulation (Tanizaki et al., 2010).

Another class of nucleators generating linear filaments contains multiple WASP homology 2 (WH2) domains that bind actin monomers. Among them are Spire (Fig. 10B), cordon bleu and the leiomodins. Using their WH2 domains they cluster three to four G-actins forming a nucleation core. In contrast to the processive behaviour of the formins, most of them are thought to solely cause nucleation, and while elongation is taken over by formins and other elongation factors, they remain with the pointed end. However, Spire was also reported to bind to the barbed end, competing with elongation factors and promoting filament severing (Campellone and Welch, 2010). Since most of the observations were made *in vitro* and a major function for migration is still elusive, these nucleators are just briefly mentioned here for the sake of completeness.
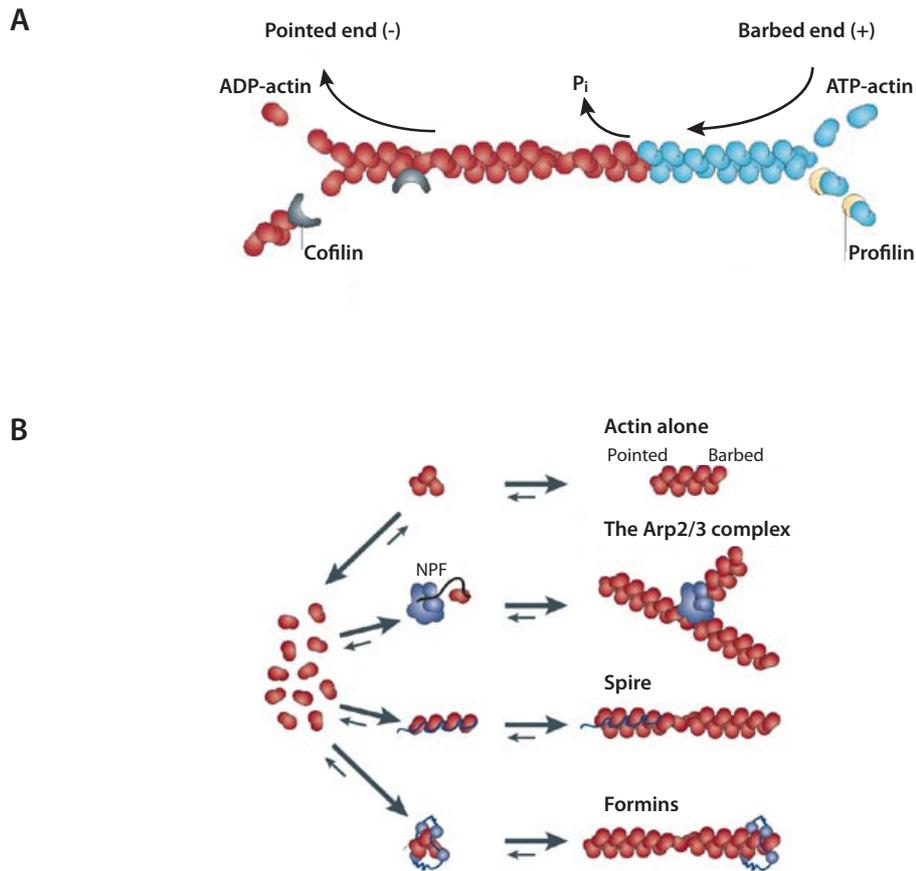
Figure 10. Actin treadmilling and nucleation. (A) Under physiological conditions actin monomers assemble into bipolar filaments with a growing barbed (+) and a shrinking (-) end. ATP-actin binds to the barbed (+) end and shifts backwards as polymerization is ongoing. While moving towards the pointed end ATP is hydrolysed to ADP and P_i by the inherent ATPase function of actin. Since ADP-actin exhibits a lower affinity to the filament it is subsequently released at the pointed (-) end. Profilin supports monomer transport and addition at the barbed end, whereas cofilin assists monomer release at the pointed end (adapted from(Cingolani and Goda, 2008)). (B) Actin nucleation requires the simultaneous clustering of three actin monomers. Since this process is kinetically unfavourable, it is catalysed by actin nucleators. Whereas *de novo* assembly of actin filaments is mediated by several nucleators, the only known "actin brancher" is the Arp2/3 complex. The Arp2/3 complex binds to existing (mother) filament and initiates the formation of a new filament in a 70° angle. Its subunits Arp2 and Arp3 structurally resemble an actin dimer and upon binding of one actin monomer an actin trimer is mimicked (nucleation core) and a new filament can arise by elongation. Thereby Arp2/3 activity depends on its association with NPFs. Formins and Spire promote nucleation of unbranched linear actin filaments by stabilizing 3-4 actin monomers (taken from (Goley and Welch, 2006)).

The Arp2/3 complex: actin nucleation and branching

The actin-related protein-2/3 (Arp2/3) complex was the first identified and has been the most intensively studied actin nucleator until now. Compared to the aforementioned actin nucleators, which form actin filaments *de novo*, the Arp2/3 complex requires the association with a pre-existing "mother-"filament (Fig. 10B). Following binding to this filament, the Arp2/3 complex catalyses the polymerisation of a new "daughter" filament at a ~ 70° angle,

resulting in a Y-branched structure. Thus, the Arp2/3 complex exhibits bifunctionality performing actin nucleation and branch-organization. The complex is constituted of seven subunits: two actin-related-proteins Arp2 and Arp3, and the five unique but highly conserved ArpC1-5. Arp2 and Arp3 structurally resemble an actin dimer. Upon binding of one actin monomer an actin trimer is mimicked (nucleation core) and a new filament can arise by elongation. Thereby, Arp2 and Arp3 are forming the first two subunits of the new filament. Since the complex is bound to the mother filament, it caps the pointed end of the new filament, which is able to grow in barbed end direction. The isolated reconstituted heptameric complex hardly shows activity *in vitro*. To gain sufficient nucleation activity it requires not only mother filament binding but also the interaction with nucleation promotion factors (NPFs). Additionally, phosphorylation of certain threonine and tyrosine residues of the Arp2 subunit seems to be critical for filament binding (LeClaire et al., 2008). The structural similarity of Arp2 and Arp3 also accounts for their function as ATPases. ATP binding by both subunits induces conformational changes in the whole complex that affects nucleation activity, whereas its hydrolysis by the Arp2 subunit triggers filament dissociation leading to debranching and complex recycling (Martin et al., 2006). The position of Arp2/3 complex binding along the mother filament has been under debate: one model suggests complex binding to and branching of barbed ends whereas the other model claims binding to the side of the pre-existing filament (Amann and Pollard, 2001; Blanchoin et al., 2000; Pantaloni et al., 2000).

The Arp2/3 complex has been supposed to be an important element for efficient migration. So far, it was shown to localize to lamellipodia and pseudopodia where it is found incorporated in Y-branched actin networks, suggesting functionality in the establishment of the underlying network complexity of these protrusive structures (Goley and Welch, 2006). Fibroblasts deficient of Arp2/3 exhibited filopodia-based non-persistent migration (Suraneni et al., 2012; Wu et al., 2012). Additionally it seems to be involved in the coordinated assembly and dynamics of focal adhesions, thus facilitating haptokinesis (Wu et al., 2012). In contrast, the complex was not found in filopodia and its requirement for their formation is still controversial; the observations made seem to be dependent on the experimental setup or cell type, respectively (Chesarone and Goode, 2009). Hence, more direct and detailed studies are necessary to prove a presumed essential role of the Arp2/3 complex in the formation and dynamics of protrusive structure, as well as its precise function and contribution to migration.

The nucleation and branching activity of the Arp2/3 complex is also exploited by numerous microbial pathogens. Manipulated recruitment and activation of the host cell's Arp2/3 complex by the pathogen from inside or outside the host cell contributes to pathogen motility in the host cytoplasm and is used during infection (Goley and Welch, 2006).

Regulating actin dynamics

Actin network dynamics and organization relies on the coordinated interplay of actin

nucleators, elongators and other actin binding proteins. Upstream signalling pathways tightly control their activity and availability in space and time. Ultimately, this leads to distinct subcellular actin structures with unique dynamics and mechanics required for different steps and phases of migration.

Nucleation promotion factors: regulators of Arp2/3 activity

As mentioned before, Arp2/3 activity depends strongly on the association with nucleation promotion factors (NPFs). Based on their Arp2/3 activation mechanism they are classified in class I and class II NPFs.

Mammalian class I NPFs are compromised of the Wiskott-Aldrich-Syndrome protein (WASP), neural WASP (N-WASP), the three WASP family verprolin homologue (WAVEs or SCAR, suppressor of cyclic AMP repressor) and the recently identified WASP and SCAR homologue (WASH), WASP homologue associated with actin, membrane and microtubules (WHAMM) and junction-mediated regulatory protein (JMY)(Fig. 11A). Although their individual overall protein sequence is rather diverse, they all share a conserved carboxy-terminal WCA domain: the W or WH2 (WASP-homology-2) domain binds G-actin for barbed end addition and the CA (C = central/cofilin-homology/connector; A = acidic) domain is responsible for Arp2/3 complex binding and activation. The isolated WCA domain has been demonstrated to be sufficient to activate Arp2/3 *in vitro* for nucleation and polymerization of branched actin filaments (Goley and Welch, 2006; Machesky et al., 1999; Stradal et al., 2004). Thus, class I NPFs serve as scaffolding proteins recruiting and bringing together activated Arp2/3 and G-actin. Association of this entity with an existing filament paves the way for the polymerization of a new filament branching off the old one (Fig. 11C).

Class II NPFs lack the G-actin binding WH2 domain and instead harbour repetitive sequences binding to F-actin. An acidic Arp2/3 binding domain is located at the N-terminus. Class II NPFs include cortactin, coronin, haematopoietic-specific protein 1 (HS1), actin-binding protein-1 (Abp1) and Pan1. They are rather weak activators of Arp2/3 but can cooperatively bind to it together with class I NPFs, resulting in enhanced Arp2/3 activation. In contrast to class I NPFs, they remain with branch junctions either stabilising or destabilising them (Campellone and Welch, 2010; Goley and Welch, 2006).

(N-) WASP

The best-characterised class I NPF is (N-) WASP. Whereas WASP expression is restricted to the haematopoietic system, N-WASP is ubiquitous, with highest expression levels in the nervous system. WASP has been identified as the causative gene of human Wiskott-Aldrich Syndrome, an X-linked disease, which was described as a clinical triad of immunodeficiency, thrombocytopenia and eczema (Bosticardo et al., 2009; Derry et al., 1994). Both, WASP and N-WASP comprise approx. 500 amino acids and exhibit a similar modular domain organization: an amino-terminal WAVE homology 1 (WH1) domain, a more central basic domain followed by the GTPase-binding (GBD) domain including CDC42 and Rac interactive binding (CRIB) domain and autoinhibitory motifs. A prolin-rich region (PRD)

precedes the abovementioned carboxy-terminal WCA domain. By itself, (N-) WASP is autoinhibited by the folding of the N-terminal acidic domain within the basic region. This intramolecular interaction sterically blocks its regulatory CBD as well as the WCA domain preventing Arp2/3 binding. The WH1 was shown to bind the WASP interacting protein (WIP), which regulates its activity and stability (Antón et al., 2007). Binding of the Rho-GTPase Cdc42 to the CRIB region releases the WCA domain and enables Arp2/3 activation. Additionally, binding of phosphatidylinositol-4,5-bisphosphate (PIP$_2$) to the basic region, as well as SH3 (Src homology 3)-domain-containing proteins to the PRD contributes to (N-) WASP activation (Takenawa and Suetsugu, 2007). Phosphorylations close to the CRIB domain by tyrosine kinases of the Src family seem to enhance Arp2/3 activation in cooperation with Cdc42 but also mark it for proteasome-mediated proteolysis (Fig. 11B)(Cory et al., 2002; Suetsugu et al., 2002).

As one of the major Arp2/3 activators, (N-) WASP is a key regulator of actin polymerization for multiple cellular functions. Its activity during migration has been linked to filopodia formation where it localizes to filopodial tips, but filopodia can still form in its absence (Lommel et al., 2001; Snapper et al., 2001). Its necessity and implication in immune cell function and leukocyte trafficking has been demonstrated in several studies and its absence in the hematopoietic compartment affects both innate and adaptive immune responses, resulting in increased susceptibility to infections and increased incidence of autoimmune diseases. In essence, WASP seems to contribute to but is not essential for leukocyte migration (Bouma et al., 2011; 2009; Pulecio et al., 2008).

WAVE complex

In contrast to monomeric (N-) WASP, WAVE acts as a multimeric complex of five subunits. The hetero-pentameric complex is referred to as WAVE complex and consists of the WAVE protein itself, Abelson interactor (Abi), Nap1 (Nck-associated protein), Sra1 (or: PIR121, p53 inducible messenger RNA 121) and HSPC300 (or Brick1). Three isoforms of WAVE, namely WAVE 1-3, have been identified, which can differ in their intracellular localisation and tissue expression. The WAVE subunits show a similar modular domain organization as (N-) WASP including the basic, the PRD and the WCA domain but lack the GBD region. Instead of the WH1 domain they exhibit an N-terminal Scar homology domain (SHD) and their basic region binds phosphatidylinositol-3,4,5-triphosphate (PIP$_3$). Differences in the PRD sequence lead to the binding of distinct regulatory SH3-containing proteins compared to (N-) WASP. The SHD mediates the binding of Abi and HSPC300, which in turn bind Nap1 and Src resulting in the formation of a functional pentamer. Due to the missing GBD, the upstream activating GTPase Rac cannot directly associate with the WAVE protein but the interaction is established indirectly by the binding of Rac to Nap1 and Sra1. Depending on the tissue, the other subunits are expressed as different isoforms and it could be shown that the absence of a single component affects the localisation of the others and/or results in the degradation of the whole WAVE complex. Similar to (N-) WASP, the reconstituted complex is inhibited and gains activity through the association of several other factors. Compared to (N-) WASP, the
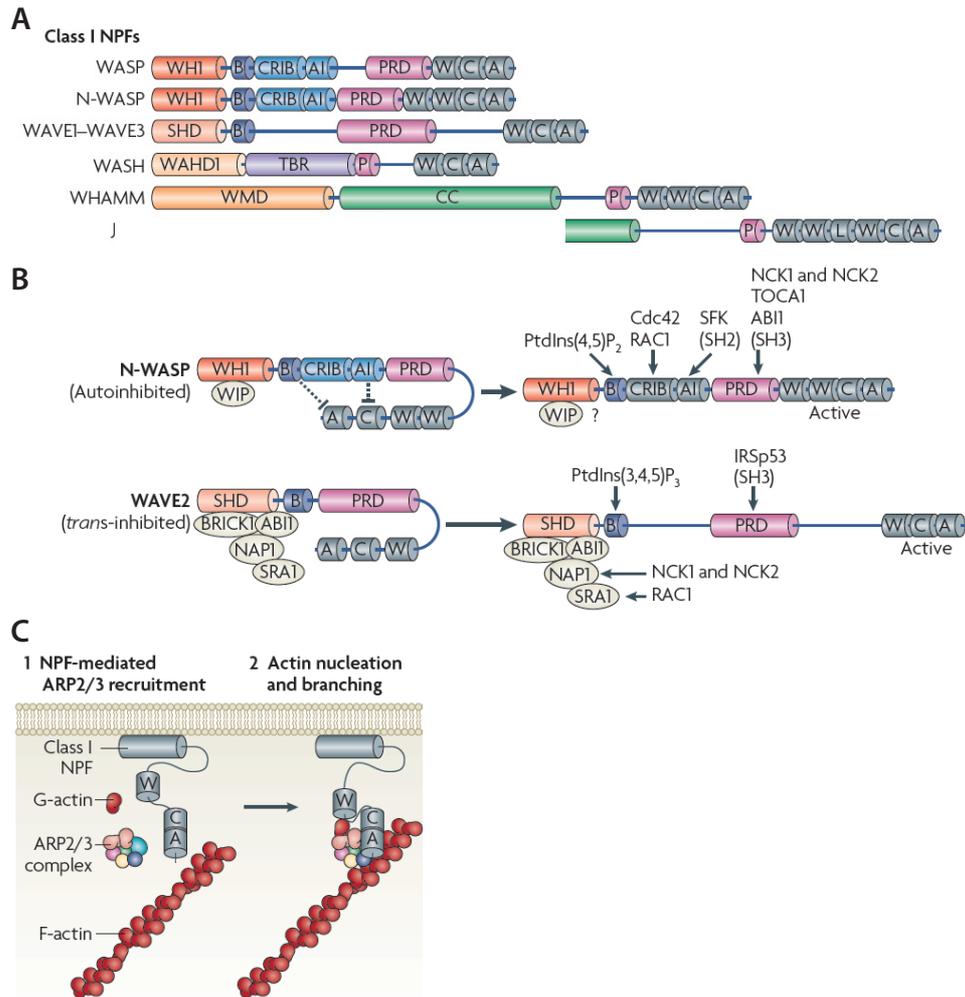
Figure 11. Mammalian nucleation-promoting factors (NPFs). (A) All class I NPFs comprise carboxy-terminal WCA domains that bind G-actin and the Arp2/3 complex. In addition, they contain diverse amino-terminal regulatory regions. (B) (N-) WASP shows a modular domain organization and is autoinhibited by an intramolecular fold. Its activity is regulated by interactions with Cdc42 and WIP family proteins. Additionally, its activity can be stimulated by direct binding of phosphoinositides and SH2- or SH3-domain-containing proteins, as well as Tyr phosphorylation. WAVE appears as a hetero-pentameric complex. The activity of the WCA containing WAVE subunit is controlled by a protein complex comprising BRICK1 (also known as HSPC300), ABL interactor 1 (ABI1), NCK-associated protein 1 (NAP1) and specifically Rac-associated 1 (SRA1). Its activity is modulated by non-catalytic kinase (NCK)–NAP1 and Rac–SRA1 interactions, or by binding of phosphoinositides or SH3-domain-containing proteins to WAVE2 itself. (C) Class I NPFs serve as scaffolding proteins. Upon GTPase activation they are recruited to the plasma membrane where they assemble and activate Arp2/3, F-actin and actin monomers, thus, facilitating actin nucleation and branching. Question marks indicate that the mechanism of activation is speculative. B, basic region; CRIB, Cdc42–Rac interactive binding; IRSp53, insulin receptor substrate protein of 53 kDa; JMY, junction-mediating regulatory protein; P, polyproline; PIP, phosphorylated phosphoinositides; PRD, Pro-rich domain; PtdIns(3,4,5)P3, phosphatidylinositol-3,4,5-trisphosphate; PtdIns(4,5)P2, PtdIns-4,5-bisphosphate; SFK, Src family kinase; SHD, SCAR homology domain; TBR, TOCA1, transducer of Cdc42-dependent actin assembly 1; W, WASP homology 2 domain; WH1, WASP homology 1 domain; WIP, WASP-interacting protein ()adapted from (Campellone and Welch, 2010)).

activation is not only mediated by direct interactions with WAVE but also through interactions via the other complex subunits. Direct binding of SH3-containing proteins and PIP$_3$ in addition to tyrosine-phosphorylation within the WAVE sequence synergistically activate the WAVE complex and augment its affinity for Arp2/3. Apart from the indirect complex-mediated activation by Rac, several other regulatory proteins, particularly kinases associate with the other subunits of the complex and modulate WAVE activity (Fig. 11B).

Whereas (N-) WASP has been shown to be involved in diverse cellular processes, WAVE-dependent Arp2/3 activation mainly contributes to actin polymerization-driven membrane protrusion. The absence of WAVE1 or WAVE2 particularly impairs the formation of protrusive structures and cell motility. Moreover, WAVE2 has been shown to be crucial for lamellipodia formation and extension, whereas WAVE1 stabilizes lamellipodia during mesenchymal migration (Suetsugu et al., 2003; Yamazaki et al., 2005; 2003; Yan et al., 2003). Likewise, WAVE3 has been also observed locating to the leading edge of chemotacting endothelial cells (Sossey-Alaoui, 2005). In summary, WAVE complex was found to be concentrated in the leading edge during mesenchymal migration, and the absence of a single WAVE protein affects distinct subcellular structures of cell motility.

WASH, WHAMM and JMY

These more recently discovered class I NPFs also feature a WCA domain and promote Arp2/3-dependent actin polymerization.

WASH was found to stimulate Arp2/3 activity, thereby controlling endosomal trafficking Like WAVE it is incorporated in a larger multimeric complex, which locks it in an inhibited state (Derivery et al., 2009; Gomez and Billadeau, 2009). By regulating endosomal integrin trafficking, WASH has been shown to be affect integrin-mediating cancer cell invasion (Zech et al., 2011). However, a direct link between WASH-dependent Arp2/3 activity and protrusive actin structures has not been described yet.

WHAMM interacts with both the actin and the microtubule cytoskeleton. It has also been shown to be involved in regulating the endoplasmic reticulum (ER)-Golgi transport(Campellone et al., 2008). Its contribution to cell migration is still elusive.

JMY has been originally identified as a co-activator of p53-dependent transcription (Shikama et al., 1999). Later, its potential to promote actin nucleation was revealed (Zuchero et al., 2009). Compared to the other class I NPFs, JMY exhibits a unique WCA domain consisting of three WH2 domains and enabling it to bind three actin monomers. Thus, JMY is able to directly nucleate and elongate actin filaments even in the absence of the Arp2/3 complex (Campellone and Welch, 2010). This bifunctionality might give JMY the capability to induce and drive rapid actin network assembly (Roadcap and Bear, 2009). JMY has been shown to predominantly locate to the nucleus. However, JMY redistributes to the leading edge in primary human neutrophils. Consistent with the observation that the leading edge localization particularly correlates with rapidly migrating cells, this reinforces the presumption that JMY regulates highly dynamic actin networks (Roadcap and Bear, 2009; Zuchero et al., 2009).

Actin-binding proteins regulate filament length

In vitro studies have shown that essentially five proteins are sufficient to provide regulated actin treadmilling of filaments reconstituting actin-based motility of bacteria or beads: actin, Arp2/3 complex, an NPF (Arp2/3 activator), an actin depolymerization factor and a capping protein (Disanza et al., 2005). *In vivo* several actin-binding proteins are engaged to promote or interfere with actin assembly thus providing a spatiotemporally controlled dynamic actin network.

Profilin and ADF/cofilin both guarantee a steady-state monomer concentration suitable for actin treadmilling and synergistically accelerate the treadmilling rate by a multitude (*in vitro* by 125-fold). ADF/cofilin promotes pointed end depolymerization by preferentially binding to ADP-actin of G- and F-actin. Thereby the available actin monomer pool increases and boosts barbed end growth. Additionally, by severing filaments ADF/cofilin generates new barbed ends, which can be used for elongation. ADF/cofilin localizes in the lamellipodium but is excluded from the very leading edge. In contrast, profilin specifically complexes with ATP-actin, and delivers it to filament barbed ends. By catalysing nucleotide exchange, profilin supports the formation of polymerization-competent ATP-actin. In essence, the combined action of profilin and ADF/cofilin shifts the distribution of incorporable G-actin towards the barbed end, thus fostering directional filament growth (Disanza et al., 2005; Le Clainche and Carlier, 2008).

Once the catalytic help of the actin nucleators has overcome the kinetic barrier of filament nucleation, filament elongation proceeds. Apart from the elongation activity of the formins, other proteins bind and accelerate barbed end growth. Prominent representatives of elongation factors involved in cell motility are the Ena/VASP family proteins. In addition to barbed end binding, these proteins complex with profilin/G-actin. This interaction orients the G-actin towards the F-actin, thereby facilitating its addition to the growing end (Ferron et al., 2007). Ena/VASP localise to filopodial tips and the lamellipodial rim, as well as focal contact sites, hence, driving actin polymerization required for cell migration. Moreover, it was proposed that Ena/VASP protects growing filament ends from binding capping proteins ("anti-capping hypothesis") thereby permitting fast actin polymerization (Bear and Gertler, 2009). Actin cappers compete with actin elongators for binding of the filament's barbed ends and terminate elongation. Several actin cappers with partly redundant capping functions are known (Witke et al., 1995). The actin cappers gelsolin, CapG, capping protein (CP) and Eps8 have been shown to be involved in the formation of protrusive structures required for motility. Actin-cappers support treadmilling in several ways. Blocking of filament growth increases the G-actin steady-state concentration that in turn promotes F-actin nucleation or elongation of non-capped filaments. By preventing filament extension capping protein activity influences the filament lifetime and length, as well as the density of the actin array. Thus, signalling-controlled and spatially-restricted capping/uncapping is a proposed mechanism how the cell selectively regulates elongation of individual filaments, thereby generating site-specific actin structures (Disanza et al., 2005). Capping proteins seem to essentially contribute to lamellipodia formation(Carlier and Pantaloni, 2007). In cooperation

with Arp2/3-dependent actin nucleation and branching it determines the density of the lamellipodial actin meshwork (Disanza et al., 2005; Wiesner et al., 2003). Disturbing the activity of CP supresses lamellipodia but promotes filopodia(Mejillano et al., 2004).

Rho GTPases controlling actin-based motility

Spatiotemporal control of the dynamics and organization of the actin cytoskeleton is fundamental for actin-based motility. Several physiological processes including leukocyte trafficking require directional migration in response to environmental cues. To follow and react to environmental guidance the exogenous signal is transduced by distinct cue-specific receptors, which subsequently switch on signalling cascades initiating actin remodelling. Typically, signal transduction occurs via receptors of the G-protein coupled receptor (GPCR), receptor tyrosine kinases (RTK), integrin or the immunological Toll-like, B and T cell receptor families (Fig. 12). Although the proximal downstream signalling events are rather receptor-specific they all converge at the level of Rho-GTPase activation. Among other fundamental cellular processes Rho-GTPases have emerged as central players in the signalling network governing actin remodelling for cell motility. The mammalian Rho GTPase family comprises 23 members and their activity is determined by the cycling between a GTP-bound active and a GDP-bound inactive state. The latter is caused by its intramolecular enzymatic activity leading to GTP hydrolysis. This molecular switch is regulated by GEFs (guanine nucleotide-exchange factors) and GAPs (GTPase activating proteins). RhoGDIs (Rho guanine dissociation inhibitors) control the availability of activatable Rho-GTPases from their entire pool. The post-translationally prenylated carboxy-terminus usually targets and anchors Rho-GTPases to membranes where their activation is controlled by GEFs and GAPs. By masking of the hydrophobic anchor, the RhoGDIs keep the Rho-GTPases in the cytosol, thus impeding their membrane distribution and preventing the interaction with their activators and effectors. Downstream receptor signalling controls the activity of the Rho-specific GEFs, GAPs and RhoGDIs.

The pioneering work by Hall and colleagues revealed the Rho-family GTPases RhoA, Rac, and Cdc42, regulating different actin cytoskeletal rearrangements and structures required for motility via distinct downstream signalling pathways.
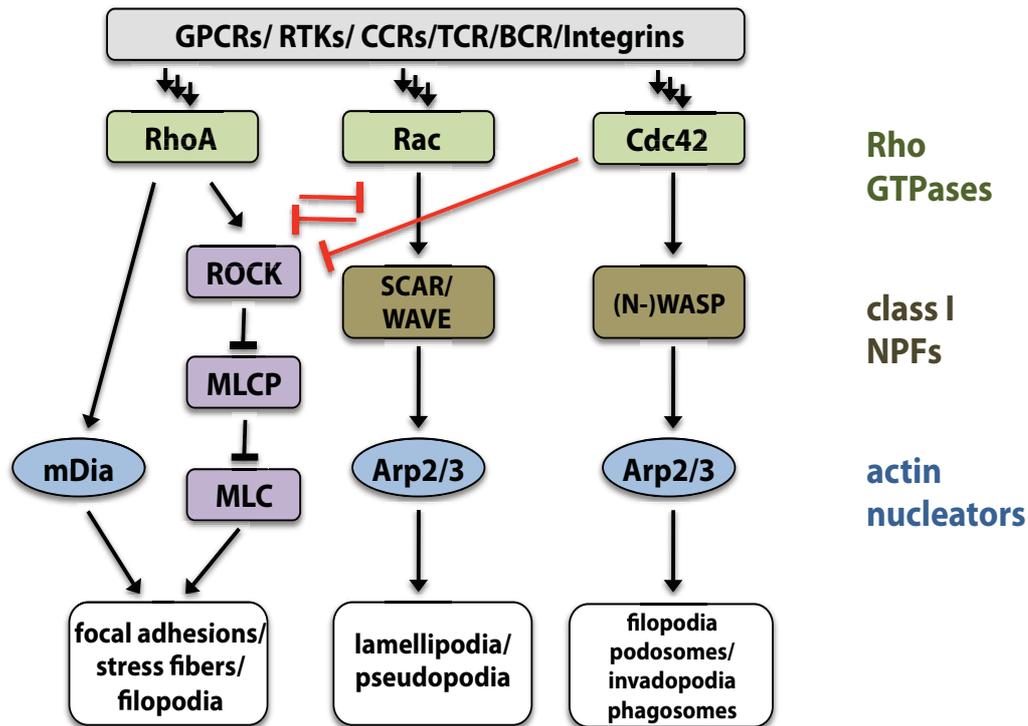
Figure 12. Distinct signalling pathways control different actin cytoskeletal rearrangements. In response to receptor ligation distinct signalling pathways that include the activation Rho family GTPases lead to the activation of different actin nucleators and result in the formation of distinct cellular structures. Cdc42 has been attributed with the formation of filopodia, podosomes and invadopodia via the regulation of the formin mDia2 and the Arp2/3 complex. Rac activity has been linked to lamellipodia formation via the WAVE complex. RhoA is critical for the formation of actomyosin structures such as focal adhesions and stress fibers. GTPase crosstalk enforces spatial and temporal separation of these processes (red lines). ROCK, Rho-associated protein kinase; MLCP, myosin-light-chain phosphatase; MLC; myosin light chain.

Rac activity has been shown to mediate lamellipodia formation by targeting different modules of the actin polymerization machinery. Active Rac at the leading edge of a migrating cell associates with the WAVE complex, thereby driving Arp2/3-dependent actin nucleation and filament branching. Moreover, Rac signalling controls actin filament turnover by negatively regulating the actin depolymerization factor ADF/cofilin, thus limiting filament severing in the lamellipodial region (Disanza et al., 2005). Via positive regulation of actin cappers such as gelsolin, Rac confines filament growth and guarantees a high G-actin concentration at steady state, feeding newly arising and elongating non-capped filaments (Azuma, 1998). Hence, Rac signalling drives a protrusive lamellipodial actin array by controlling filament length, density and turnover.

Aside from its function in cellular polarity, Cdc42 activity has been implicated in the formation of filopodia (Nobes and Hall, 1995). Cdc42 directly activates (N-) WASP and induces Arp2/3-dependent actin assembly. This pathway was implicated in filopodial actin network generation (Prehoda, 2000; Takenawa et al., 1998). However, this has been challenged by the observation that filopodia can still form in the absence of Cdc42, (N-)WASP and Arp2/3 (Ladwein and Rottner, 2008; Ridley, 2006). Nevertheless, none of these observations can exclude a contribution of this pathway in filopodia formation but preclude an essential role. More recent studies provide evidence that Cdc42 signalling drives actin polymerization in filopodia via formins (Block et al., 2012; Ridley, 2011). In addition to its function in filopodia formation, Cdc42 can also localize in and induce lamellipodia via Rac (Ladwein and Rottner, 2008; Machacek et al., 2009). Cdc42/(N-)WASP/Arp2/3-driven actin polymerization has been also linked to the formation of invasive structures like invadopodia and podosomes, as well as phagocytotic cups (Murphy and Courtneidge, 2011; Ridley, 2011; Swanson, 2008).

Both, Rac/WAVE and Cdc42/(N-)WASP bind the membrane-associating IRSp53 (insulin-receptor substrate of 53 kDa). Upon accumulation at the membrane, the curved structure of IRSp53 induces outward deformation. Thus, bringing together actin polymerization by Arp2/3 and active membrane-bound IRSp53 is a possible mechanism for the initiation and extension of lamellipodia or filopodia, respectively (Ridley, 2011; Takenawa and Suetsugu, 2007).

Active RhoA controls the formation of contractile actomyosin structures as focal adhesions and stress fibers by targeting the formin Dia1 and the myosin activation pathway. The contractile potential of these structures is usually employed for the retraction of the cell body and tail detachment, and are therefore assembled behind the protrusive front (Ridley, 2006). However, RhoA has been also observed to localise to the leading edge under certain conditions (Kurokawa, 2005; Pertz et al., 2006).

PROJECT DESCRIPTION

The role of branched actin networks in dendritic cell physiology

Dendritic cells – the cellular system used

Dendritic cells (DCs) act as sentinels of tissue barriers and operate at the interface of innate and adaptive immunity. They exist in two distinct states: an immature and a mature state. Immature DCs reside in the periphery and scan the environment for pathogenic invasion using pattern recognition receptors (PRRs)(Steinman, 1991; 2002). In response to danger signals, e.g. microbial-associated patterns, DCs undergo a differentiation process that has been termed maturation. Upon maturation DCs ingest microbial material and subsequently start migrating from the periphery via the afferent lymphatic vessels into the T cell area of the draining lymph node (LN)(Banchereau and Steinman, 1998; Mellman and Steinman, 2001). Here, DCs present the peripherally acquired and processed antigen (Ag) via MHCs (major histocompatibility complex) to induce an Ag-specific immune response. Naïve T cells scan the DCs and in case of a cognate interaction between the MHC-peptide complex and the T cell receptor (TCR) the T cell is activated.

To reach the next draining lymph node, mature DCs need to be guided to the afferent lymphatic system where they are then passively transported by the lymphatic stream. Once arrived at the subcapsular sinus of the LN DCs transmigrate into the cortical region. There, they are further conducted to the T cell zone where T cell priming can occur. Migration towards the lymphatic vessels, as well as into the T cell zone requires guidance that is realized by gradients of the homeostatic chemokines CCL19 (soluble) and CCL21 (matrix bound). DC maturation includes the expression of the chemokine receptor CCR7 that is exposed at the cell surface of mature DCs. The chemokines CCL19/21 are sensed by CCR7 and mature DCs respond with directional migration along the chemokine gradient (chemotaxis). On their journey from the periphery to their ultimate destination, the T cell zone, DCs have to pass several tissue environments and barriers demanding a highly adaptable but at the same time rapid migration mode to start a quick immune response.

Altogether, this makes DCs a challenging and appropriate cell system to study directed cell migration (chemotaxis, transmigration) including interaction and force transduction to the ECM, as well as dynamic cell-cell interactions (like DC-T cell interactions).

Aim of the thesis

Many processes contributing to the maturation and function of DCs depend on the coordinated remodelling of the actin cytoskeleton. To pass and overcome the diverse tissue environments and barriers demands a high degree in flexibility of migrating DCs, which is achieved by constant amoeboid shape changes generated by actin network dynamics

(Lämmermann and Sixt, 2009). Thus, one can regard DCs as an archetype of amoeboid migrating cells. Spatiotemporal regulation of polymerisation rate is one of the central regulators of such actin-driven shape changes. Apart from the kinetic parameters of actin remodelling, actin filament and network geometry are considered as another determinant of fast amoeboid migration. But how actin filament geometry affects the network dynamics and mechanics, and ultimately DC morphology and its physiological function, particularly its chemokine-guided migration has not yet been assessed.

Therefore we aim to describe the importance of branched actin networks for the abovementioned DC functions. Whereas *de novo* assembly (nucleation) of actin filaments is mediated by several actin nucleators the only known "actin brancher" is the Arp2/3 complex, whose activity is dependent on the association with nucleation promoting factors (NPFs). One of the major NPFs is the multimeric WAVE complex, which functions downstream of Rac-GTPase signalling. Its assembly was shown to be essential for lamellipodia formation and the absence of each single component of the complex results in the destabilization of the whole complex (Derivery et al., 2008; Innocenti et al., 2004; Kunda et al., 2003; Rogers et al., 2003; Steffen et al., 2006; 2004). Although ubiquitously expressed and showing a highly conserved stoichiometric composition of the five core components, WAVE complexes diverge due to cell/tissue specific isoform expression and alternative splicing of the subunit transcripts. A specific subunit of the hematopoietic compartment is the Hem1 protein. A mutant was reported, which carries a point mutation in the *Hem1* gene leading to a premature stop codon and consequently a lack of all WAVE complex components in all hematopoietic cells (Park et al., 2008). Those mice are viable but show a very severe and complex immunological phenotype. To what extent the depletion of *Hem1* in dendritic cells affects their function and finally contributes to the observed immunological phenotype is still unclear.

In this thesis, I characterize the consequences of WAVE complex ablation upon *Hem1* deletion, and the resulting loss of branched actin filaments on DC maturation and physiology. For this purpose, we accessed a conditionally targeted *Hem1* mouse. Using this mouse we were able to generate constitutively *Hem1* deleted animals that we employed for the *in vitro* generation of WAVE depleted DCs. Using these cells I was able to morphologically and functionally characterize the consequences of the knockout *in vitro* and *in vivo*.

Preliminary work: Generation of the conditionally targeted *Hem1* mouse

This work is based on the recently generated and yet not published conditionally targeted *Hem1* mouse. This work was carried out in the laboratories of our collaborators Prof. Dr. Theresia Stradal and Prof. Dr. Klemens Rottner, in particular by their former postdoc Dr. Frank Lai at the Helmholtz Centre for Infection Research in Braunschweig, Germany. In the following, I briefly describe the applied conditional targeting strategy for the *Hem1* allele and the subsequent generation of a constitutively *Hem1* deleted mouse.

The *Hem1* gene is located on the murine chromosome 15F3 and comprises 31 exons of

approx. 45 kilobases. Exons 4 and 5 were flanked with loxP sites and an excisable neomycin resistance cassette was placed in the intron before exon 4. A targeting construct was used to replace one wildtype (*WT*) allele in embryonic stem cells (ES line IGD3.2 (Hitz et al., 2007)), with the mutated allele flanked by loxP-sites for recombination. A targeted ES cell clone was injected into blastocysts and gave rise to germline transmitted chimeric animals. The resulting animals (fl_neo/*WT*), carrying one wildtype and one mutated allele were crossed with a transgenic mouse expressing the flip recombinase to remove the neo cassette and to produce the floxed allele. The floxed allele (fl/*WT*) was backcrossed into a pure C57BL/6 background. For the generation of *Hem1* knockout (del/del) animals, the *Hem1* (fl/*WT*) mice were crossed with a mouse expressing Cre-recombinase under control of the keratin 14 promotor. This *Cre* allele, when inherited from the mother results in total gene deletion, because it is expressed in the oocyte (Hafner et al., 2004). Thus, crossing of male *Hem1* (fl/*WT*) animals with female K14-cre mice produced heterozygously deleted *Hem1* (del/*WT*) animals in the next generation (F1 generation).

RESULTS

BMDC differentiation from Hem1 depleted bone marrow precursor cells

In this study, we used murine bone marrow-derived DCs (BMDCs) as an experimental paradigm. DCs derive from the lymphoid and myeloid lineage from pluripotent hematopoietic stem cells (HSCs) and can be differentiated *in vitro* from precursor cells within the bone marrow in the presence of growth factor granulocyte macrophage colony-stimulating factor (GM-CSF). BMDCs were used for two reasons: (1) endogenous DCs are rare populations in all organs and spread throughout the whole organism, which makes it difficult to isolate them in sufficient quantities. Additionally, depending on their tissue localisation, DCs appear in several distinct subsets with diverse physiological functions and cellular characteristics. Employing BMDC cultures circumvents the heterogeneity aspect and the limited availability. Using *in vitro* cultures, we were able to obtain DCs in large quantities in a rather homogenous population from little biological material. (2) BMDCs were accessible throughout the whole differentiation period and could be manipulated (e.g. transfection with plasmids) prior to subsequent experimental assays.

Hem1 deletion does not affect BMDC differentiation and results in the degradation of the WAVE complex

As mentioned in the project description, we aimed to interfere with Arp2/3-dependent actin branching by destabilizing the upstream activating WAVE complex. *Hem1* was suggested as the hematopoietic cell specific component of the WAVE complex and the recently reported *Hem1*-deficient mouse exhibits loss of WAVE components in several hematopoietic cell types (Park et al., 2008). To experimentally approach the role of actin branching for DC migration, we differentiated WAVE depleted DCs from bone marrow of $Hem1^{-/-}$ mice, which could then be used for further experimental investigations.

First we had to exclude a possible impact of the *Hem1* deletion on DC differentiation. Thus, bone marrow of *WT* and $Hem1^{-/-}$ mice was cultured separately until day 8 of the BMDC differentiation protocol to obtain immature DCs. Using flow cytometry, the expression levels of the DC specific cell surface marker CD11c as well as the major-histocompatibility complex class II (MHCII) were determined. The latter characterizes immature DCs by low to intermediate expression levels and shows high expression upon DC maturation. As seen in Fig. 13A, *Hem1* deletion did not impair CD11c expression and surface levels were comparable to immature *WT* BMDCs. Similarly, low MHCII levels were detected for *WT* and $Hem1^{-/-}$ cells but a slightly increased population expressing intermediate levels was observed in immature $Hem1^{-/-}$ BMDCs, indicating a higher rate of spontaneous maturation in *in vitro* cultures. Following DC maturation, expression of MHCII was equally upregulated in *WT* and
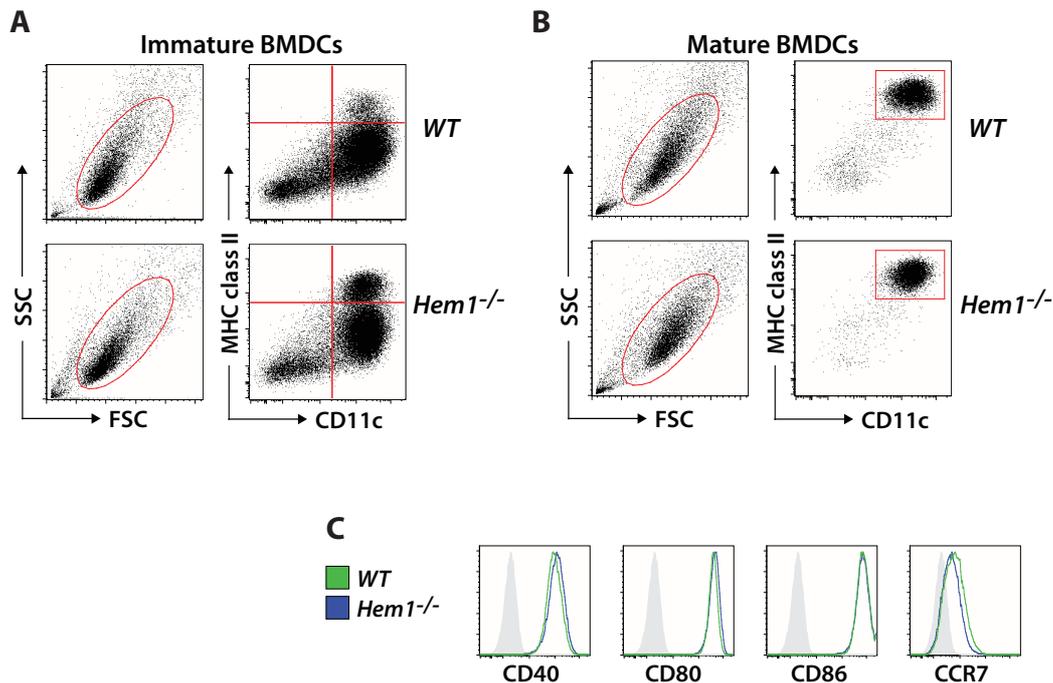
Figure 13. Differentiation of BMDCs is unaffected by *Hem1* deletion. *WT* and *Hem1^{-/-}* bone marrow was cultured in the presence of GM-CSF to differentiate BMDCs for 8 days (immature BMDCs, A) or were further matured using LPS for another 24 hours (mature BMDCs, B). Cell size (FSC, SSC) and expression of cell surface markers (CD11c, MHC class II) were determined by flow cytometry and representative dot plots are shown for immature (A) and mature BMDCs (B). Histograms (C) depict expression levels of maturation markers CD40, CD80 and CD86, as well as chemokine receptor CCR7 in gated populations of CD11c^{+}MHCII^{high} corresponding to fully matured BMDCs. Gated populations are indicated by red ovals or rectangles in A and B. FSC, forward scatter; SSC, side scatter; MHCII, MHC class II.

Hem1^{-/-} DCs (Fig. 13B). In addition, the expression of several other maturation markers was compared (Fig. 13C). Neither the costimulatory phenotype indicated by the levels of CD40, CD80 and CD86, nor the expression of the chemokine receptor CCR7 varied significantly between *WT* and *Hem1^{-/-}* DCs, thus further emphasizing an unaffected maturation process upon *Hem1* deletion.

Next, we assessed the consequence of *Hem1* deletion on WAVE complex composition and stability in BMDCs. Using Western blot analysis we detected the protein levels of *WAVE* in *WT* compared to *Hem1^{-/-}* whole cell lysates of immature and mature BMDCs. Indeed, as reported for several other leukocyte subsets, loss of *Hem1* resulted in the absence of WAVE2 in both immature and mature BMDCs (Fig. 14A). To exclude a WAVE2-specific degradation or a compensation by other isoforms, the protein levels of WAVE1 or WAVE3 were verified, but were neither detected in *WT* or *Hem1^{-/-}* BMDCs (Fig. 14B and C).

These results collectively demonstrate an unimpaired differentiation and maturation of BMDCs from *Hem1^{-/-}* bone marrow precursor cells. Thus, *Hem1* is dispensable for DC development *in vitro*. Furthermore, they recapitulate WAVE complex degradation following

Hem1 deletion for BMDCs and show that in BMDCs, WAVE2 is the unique functional component of the WAVE complex.
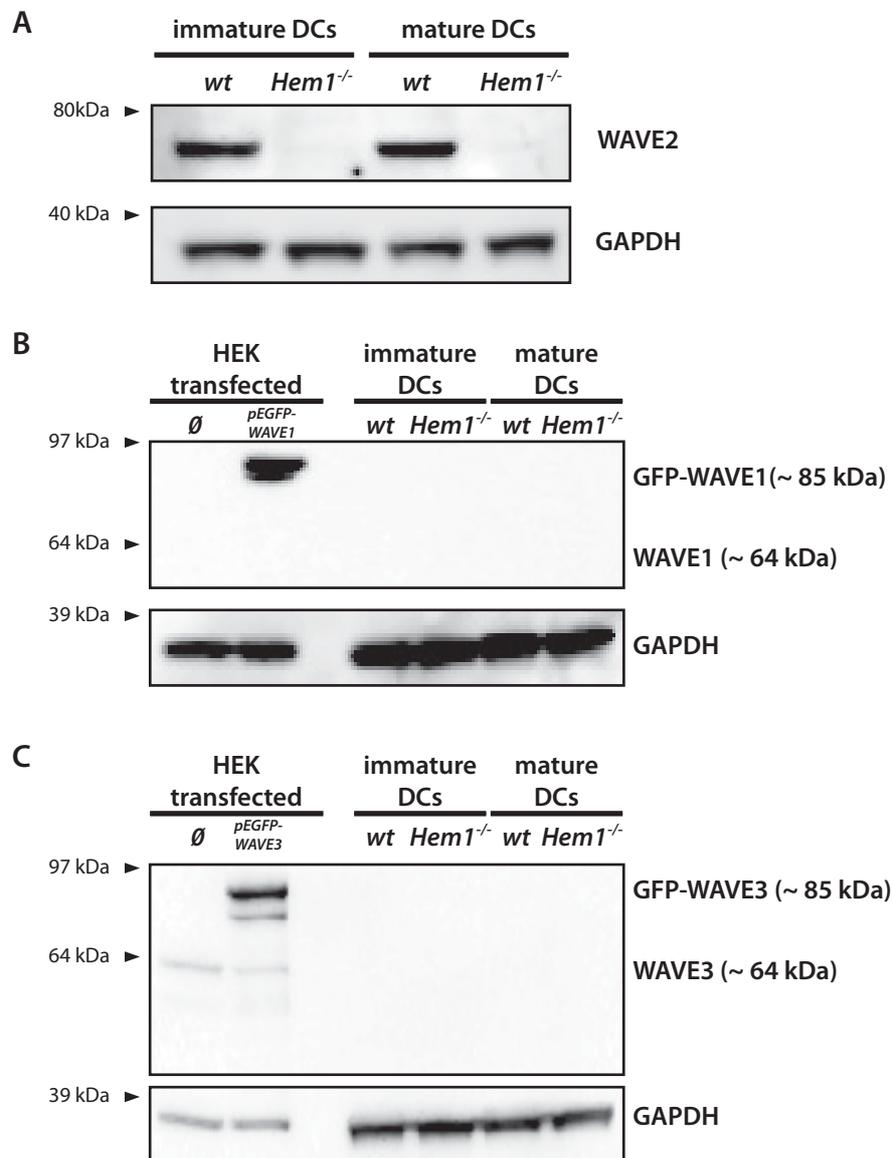
Figure 14. Expression of WAVE isoforms in *WT* and *Hem1*$^{-/-}$ BMDCs. WAVE protein levels in whole cell lysates were determined by Western blot and representative immunoblots are shown. (A) WAVE2 isoform detection in immature and mature *WT* and *Hem1*$^{-/-}$ BMDCs. (B and C) Expression of the WAVE1 or WAVE3 isoform, respectively, in BMDCs was determined relative to the expression levels in HEK cells transfected with the corresponding GFP-WAVE isoform construct. GFP-WAVE1/3 fusion proteins are expected to run at around 85 kilo Dalton (kDa), whereas the endogenous WAVE1/3 are expected at 64 kDa. Transfection experiments allowed us to verify that WAVE1/3 antibodies do indeed work. Glyceraldehyde-3-phosphate dehydrogenase (GAPDH) protein level was used as loading control.

59
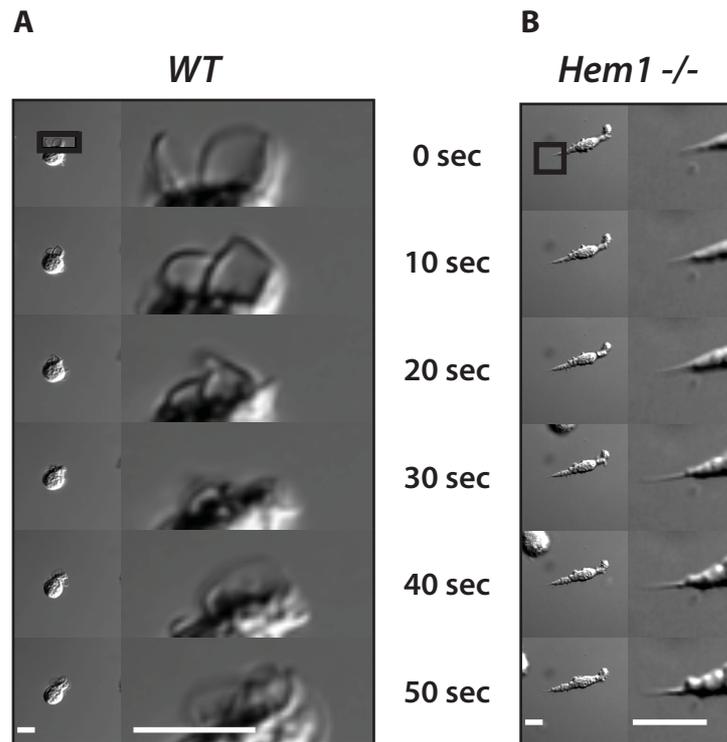
Figure 15. Morphology and protrusion dynamics of immature *WT* and *Hem1*^{-/-} BMDCs.
Immature BMDCs were observed in solution for 50 sec using differential interference contrast (DIC) microscopy. The whole cell morphologies or protrusion morphologies are displayed in the left panel and as magnified image sections in the right panel for each genotype over time, respectively. Scale bars, 10 μm; box, magnified image section.

Absence of functional WAVE complex results in a pronounced morphological phenotype

Following successful differentiation of WAVE ablated immature and mature BMDCs, we first studied its consequences on cell morphology. Using time-lapse differential interference contrast (DIC) microscopy, dynamical aspects of the cell torso and membrane protrusion morphology in solution could be observed. Immature *WT* cells overall appeared with a spherical cell body showing a unipolar formation of several membrane protrusions (Fig. 15A, left panel; Mov. S1). The membrane protrusions developed as thin lamellar sheets and could form or retract within minutes (Fig. 15A, right panel). In contrast, *Hem1* deletion caused a substantial change in cell shape. The cell body anisotropically expanded, resulting in an elongated conical morphology exhibiting two distinct cell ends (Fig. 15B, left panel; Mov. S2). The putative cell rear emerged as a roundish appendix from the torso and was separated by a small constriction site. The cell's front forms a pointed end that was continuously protruding over time (Fig. 15B, right panel). To validate the contribution of the actin cytoskeleton to the observed morphological phenotype we applied several chemical inhibitors interfering either with actomyosin or microtubule dynamics: Latrunculin A sequesters actin monomers and prevents actin polymerization, whereas Blebbistatin inhibits myosin II activity and blocks

A

$$\text{aspect ratio} = \frac{\text{major axis X}}{\text{minor axis Y}} = \frac{\text{length}}{\text{width}}$$

X/Y = 1   X/Y > 1

B

C
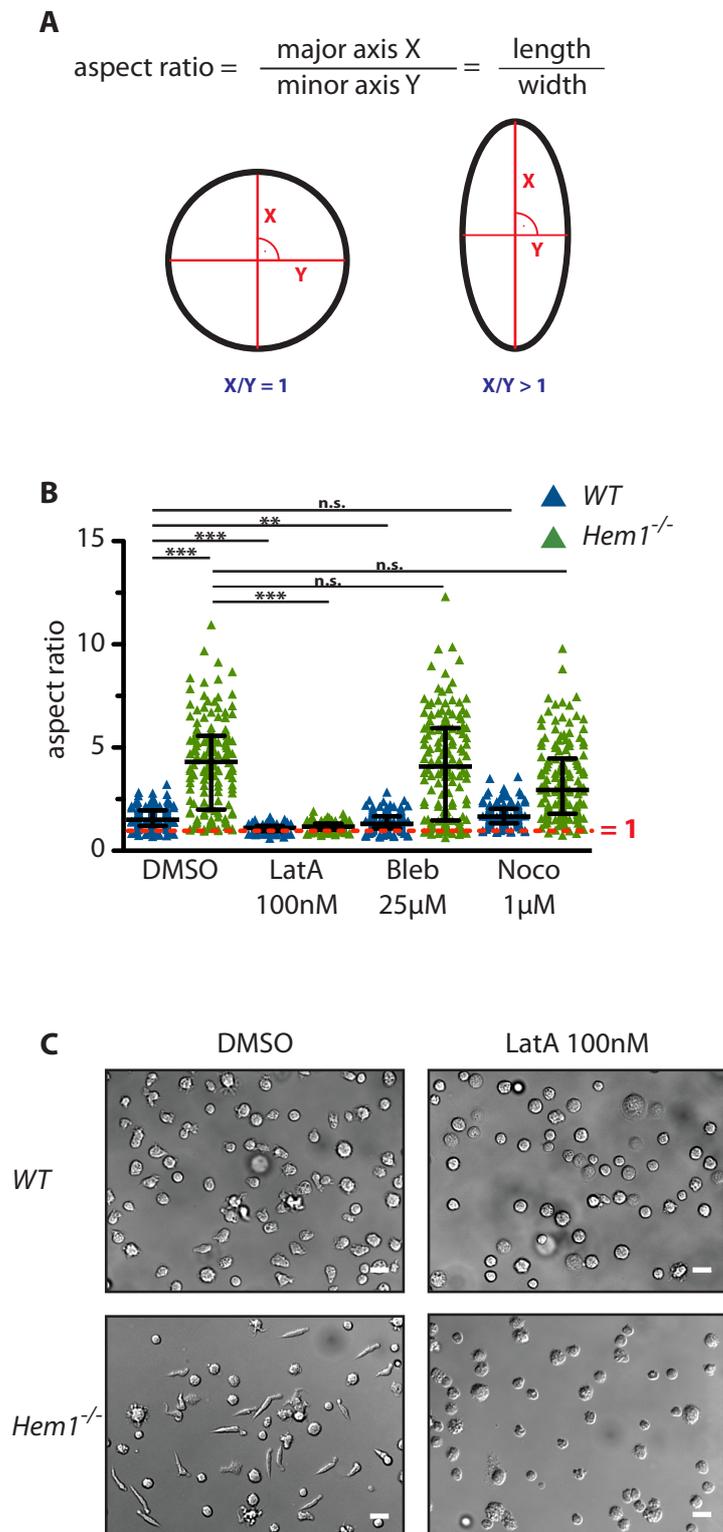
Figure 16. Cell and leading edge morphology of immature *Hem1*$^{-/-}$ BMDCs is still actin-driven. Cell morphologies of immature BMDCs in solution were read out as aspect ratios. (A) Aspect ratios were calculated by dividing the length of the major axis (cell length) of the cell diameter by the length of its minor axis (cell width). Thus, ratios close to 1 indicate for a roundish cell shape, whereas ratios > 1 signify an increasing ellipsoid shape. (B) Aspect ratios of immature *WT* and *Hem1*$^{-/-}$ BMDCs in the presence of several inhibitors affecting the cytoskeleton: DMSO was used as solvent for all inhibitors and corresponds to the global control inhibitor; Latrunculin A (LatA), prevents actin polymerization; Blebbistatin (Bleb), inhibits myosin II; Nocodazole (Noc), interferes with microtubule polymerization. n = 150, cell number analysed for each condition; triangles, aspect ratio of an individual cell; black line, median with interquartile range (error bars); red dashed line, aspect ratio of 1; n.s., not significant. Statistics: *WT (DMSO) vs. Hem1*$^{-/-}$ *(DMSO),* two-tailed student's T-test, P < 0.0001, U = 3639; all other ratios were tested using the nonparametric Kruskal-Wallis statistics, P< 0.0001. For a detailed statistical analysis see appendix. (C) Representative DIC images of immature *WT* and *Hem1*$^{-/-}$ BMDCs in the presence of DMSO or LatA, respectively. Scale bar, 20 µm.

actomyosin contraction. Nocodazole disturbs microtubule growth. Effects of the inhibitors on cell shape were read out as changes in the aspect ratio (Fig. 16A). The almost spherical morphology of the *WT* cells depended on both actin polymerization and actomyosin contractility as the corresponding inhibition led to a further cell rounding indicated by decreasing aspect ratios (Fig. 16B, blue rows, and 16C, upper panel). The *Hem1*$^{-/-}$ cell morphology significantly differed from the *WT* cells due to a high length to width ratio (Fig. 16B, green rows DMSO). As depicted in Fig. 16C (lower panel) and quantified in Fig. 16B, this elongated shape and the pointed leading edge were still purely driven by actin polymerization since addition of Latrunculin A resulted in rounding of the entire cell. Neither myosin contractility nor the microtubule cytoskeleton appeared to contribute to cell morphology (Fig. 16B).

Next, we examined the effect of the *Hem1* knockout on the morphology of mature BMDCs. Mature *WT* cells exhibited a spherical cell body characteristically covered by dynamic veil-like membrane protrusions (Fig. 17A, Mov. S3). Although commonly described as dendrites, their morphological appearance may be best illustrated as a head of a lettuce. In contrast, mature *Hem1*$^{-/-}$ BMDCs, whilst also spherical in cell body, bear plenty of finger-like membrane protrusions (Fig. 17B, Mov. S4). These protrusions could exceed the cell body diameter and continuously grow and retract uniformly over the whole cell surface. Moreover, their mechanical stability in solution seemed to be very labile, denoted by occasional buckling along the protrusion axis and back folding on the cell body.

Taken together, *Hem1* deletion and the subsequent loss of the WAVE complex resulted in pronounced differences in cell morphologies of immature and mature BMDCs. Moreover, we could clearly show that the unipolar elongated morphology of immature *Hem1*$^{-/-}$ cells was exclusively dependent on actin polymerization. Maturation in the absence of *Hem1*$^{-/-}$ transformed the unipolar elongated cell into a globular cell with uniformly distributed pointed cell protrusions. Loss of WAVE considerably changed protrusion morphology whereas numbers seemed to be largely unaffected.

A

WT

B
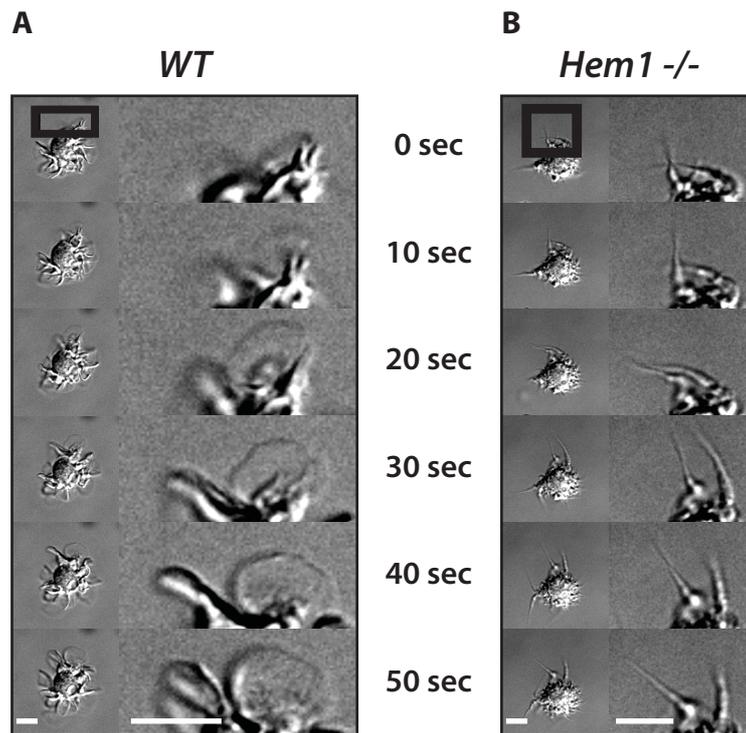
Hem1 -/-

Figure 17. Morphology and protrusion dynamics of mature *WT* and *Hem1*^{-/-} BMDCs. Mature BMDCs were observed in solution for 50 sec using differential interference contrast (DIC) microscopy. The whole cell morphologies or protrusion morphologies are displayed in the left panel or as magnified image sections in the right panel of each genotype over time, respectively. Scale bars, 10 μm; box, magnified image section.

Actin network organization in consequence of WAVE ablation

The absence of WAVE alters actin network organization at the leading edge of immature DCs

We hypothesized that *Hem1* deletion may abolish actin branching at the leading edge. To validate this assumption, and to elucidate the underlying cytoskeletal changes of the remarkable morphological phenotype of immature *Hem1*^{-/-} BMDCs, we performed high-resolution transmission electron tomography.

Immature *WT* cells nicely polarized on the electron microscopy (EM) grids and typically exhibited a "mushroom-shaped" cell outline when crawling on a planar substrate (Fig. 18A). They spread out a wide and thin lamellipodium (bright area) followed by a compact cell body and a cell back frequently accompanied by retraction fibers at its distal end (dense dark area). Immature *Hem1*^{-/-} cells maintained their unipolar shape observed in solution after attachment to the 2D grid (Fig. 18B). The leading cell tip merged into the elongated cell torso and the spherical cell rear was separated by a small membrane constriction. Tilting series of fixed and
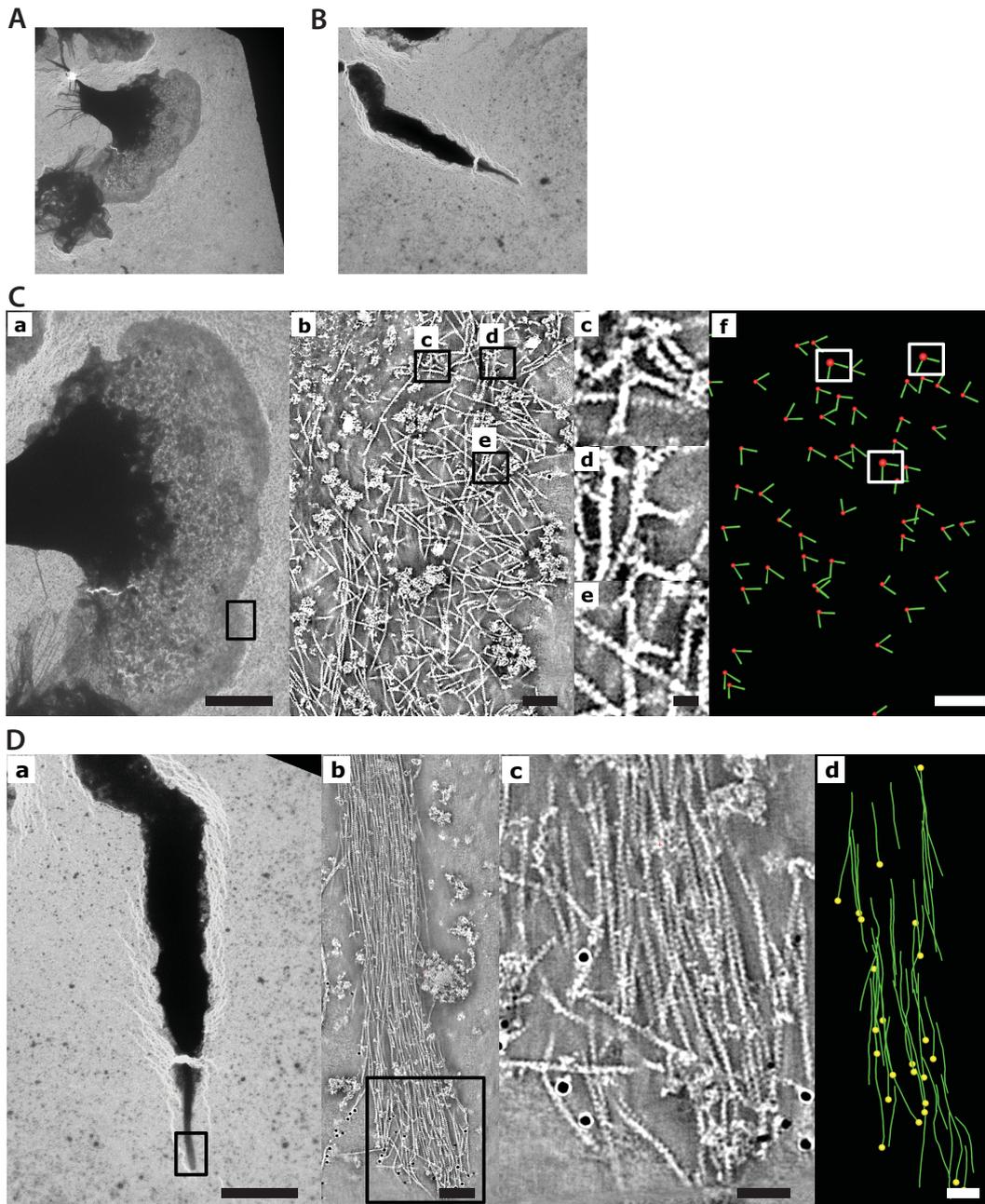
Figure 18. Actin network within the leading edge of immature _WT_ and _Hem1^{-/-}_ BMDCs.
Overview electron micrograph of a fixed and negatively stained _WT_ (A) and _Hem1^{-/-}_ cell (B). (C)
Immature WT BMDC: (C-b) Section of an electron tomogram taken from the indicated lamellipodial
region (black box) in C-a to show general organization of the actin network. (C-c to C-e) branch
junctions manually found in the tomogram. (C-f) Model of branch junctions (red dots) and
associated filaments positions (green angles). The model was used to determine the branch
angles. Scale bars: C-a, 5 μm; C-b,f, 100 nm; C-e, 220 nm (D) _Immature Hem1^{-/-} BMDC:_ (D-b) Section
of an electron tomogram taken from the leading tip (black box) in D-a to show general
organization of the actin network. (D-c) Magnified region indicated in D-b (black box). D-b and D-a
show a parallel actin network devoid of any actin branches. (D-d) Model of the branch-free leading
edge. Filaments (green) were manually tracked and their polarity (yellow dots indicate for barbed
ends) was determined as described in (Akihiro Narita, 2012). Scale bars: D-a, 5 μm; D-b,d, 100 nm;
D-c, 20 nm.

cytoskeleton-extracted samples were performed and a 3D image of the actin cytoskeleton was reconstructed. Two exemplary processed tomograms for each genotype are shown in Fig. 18C and D. In the lamellipodial segment of the *WT* cell (Fig. 18C, b-e; Mov. S5) actin filaments were clearly visible, exhibiting their characteristic helical structure. The resolution quality even allowed the identification of the globular actin subunits. The actin network exhibited a disordered array of diagonal actin filaments variably orientated towards the leading membrane that has been shown typical for lamellipodia (Koestler et al., 2008). Individual actin branches could be manually identified and tracked (Fig. 18C, f, red dots) from characteristic end-to-side associations of filaments in an angular range of 60-90° in the same z-level, accompanied by additional filament material at their apex (Fig. 18C, f)(Vinzenz et al., 2012). The average branch angle could be measured as 72 ± 10° (n=58) and branches were mostly orientated towards the leading membrane. In clear contrast to this lamellipodial actin network was the pointed leading edge of the *Hem1*$^{-/-}$ cells. The tomograms revealed an aligned array of actin filaments entirely devoid of actin branch junctions (Fig. 18D, b-d; Mov. S6). We determined filament orientation using a recently published image analysis method (Akihiro Narita, 2012). Filament barbed ends were almost entirely facing the leading tip, disclosing a parallel filament alignment (Fig. 18D, d, yellow dots).

Maturation leads to actin cytoskeletal reorganization and recovery of actin branching in the lamellipodium of *Hem1* depleted DCs

Next, we performed EM tomography with mature BMDCs to further explore the morphological changes between *WT* and *Hem1*$^{-/-}$ BMDCs.

Similar to their immature state, mature *WT* BMDCs polarized on the planar grid forming a thin and broad lamellipodia defining the cell's front, followed by a compact cell body and rear. A segment of the 3D reconstructed actin network just behind the leading membrane displayed a comparable disordered network in which several branch junctions could be identified as observed in the immature precursors. Surprisingly, attachment of mature *Hem1* deleted cells resulted in two populations: one polarized and spread out lamellipodia as seen in *WT* cells, and the other exhibited a rather unpolarized shape surrounded by several thin and pointed octopus feet-like cell extensions reflecting more the observed morphology in solution. None of these cell morphologies seemed to be preferred over the other as both populations were equally frequent (data not shown). Highly resolved EM images of a lamellipodial edge of a polarized cell of the first population revealed an apparently normal actin array indistinguishable to the *WT* situation (Compare Fig. 19A and 19B). Filaments are variably orientated towards the plasma membrane and several branch junctions with typical branch angles could be observed (Compare Fig. 19A, b-f and 19B, b-f). Tomographic segments of the actin network within a lateral region of an octopus foot of the second observed population also showed a disordered and branched actin network (Fig. 19C). These findings suggest that actin branching and lamellipodia formation can at least be partially or transiently restored in *Hem1*$^{-/-}$ BMDCs upon maturation.
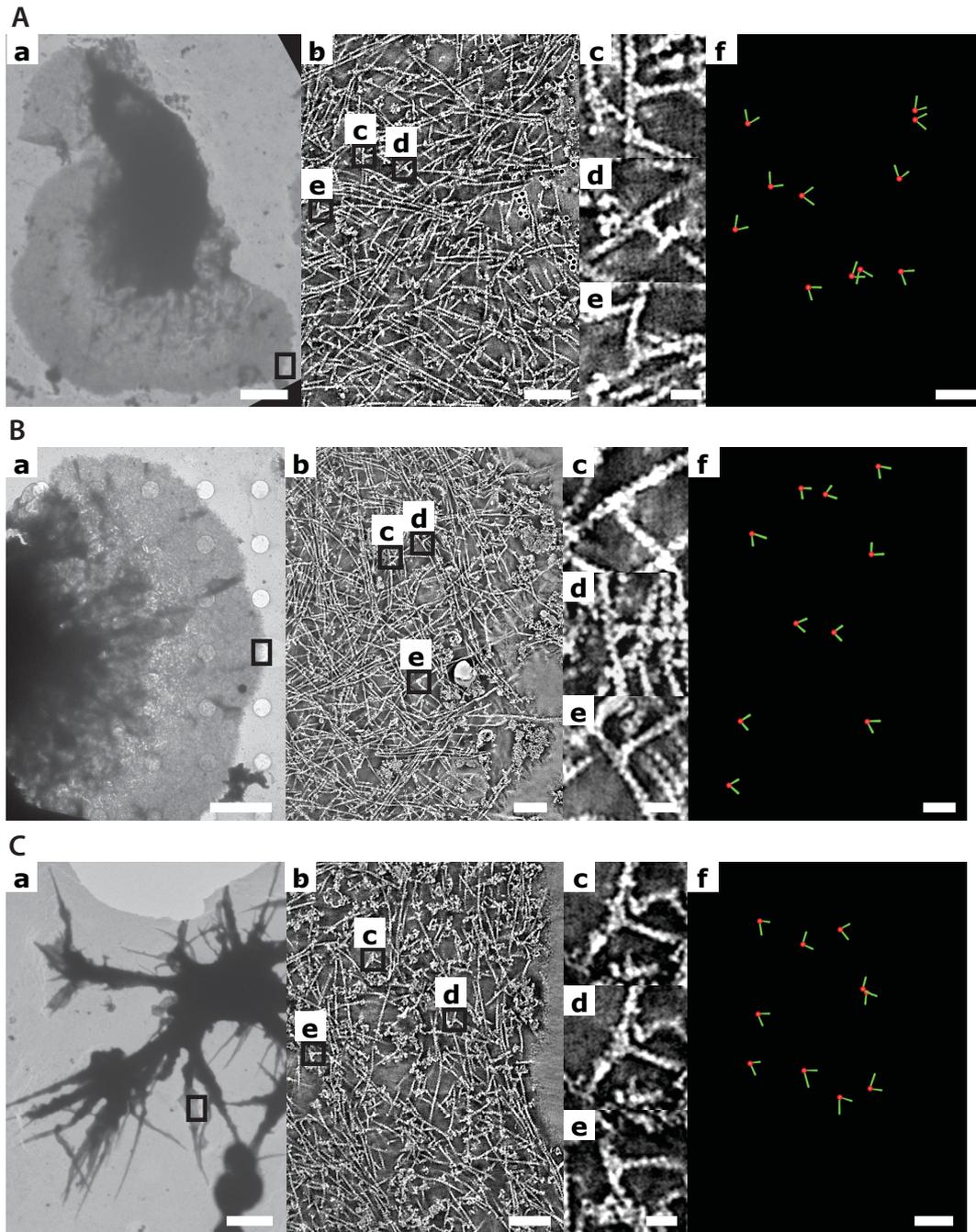
Figure 19. Actin network within the leading edge of mature *WT* and *Hem1*^{-/-} BMDCs. Overview electron micrograph of a fixed and negatively stained *WT* (A-a) and two distinct *Hem1*^{-/-} cells (B-a and C-a). (A-b to C-b) Section of an electron tomogram taken from the indicated lamellipodial region (black box) in (a) to show general organization of the actin network. (c-e) branch junctions manually found in the tomogram. (f) Model of branch junctions (red dots) and associated filaments positions (green angles). The model was used to determine branch angles of 71 ± 5° (n=11) for A, 75 ± 6° (n=10) for B and 75 ± 10° (n=10) for C. n, number of angles analysed; scale bars: a, 5 μm; b,f, 100 nm; c, 20 nm.

Migration in the absence of WAVE complex

In the previous section we could verify loss of the WAVE complex upon *Hem1* deletion in BMDCs. Furthermore, we could show that this deficiency severely influenced actin network geometry and resulted in distinctive morphological alterations in immature and mature *Hem1*$^{-/-}$ BMDCs compared to the *WT*. In this section we address how these actin network rearrangements and cell shape changes affect 3D cell migration.

Loss of branching results in the switch from random walk to random persistent walk due to increased polarity in immature DCs

In order to observe potential differences in the locomotion of immature BMDCs, we first tested chemokinesis using a reductionist *in vitro* setup. Cells were placed into 3D collagen matrices mimicking *in vivo* interstitial conditions (Lämmermann et al., 2008) and exposed to uniformly distributed CCL3. Both *WT* and *Hem1*$^{-/-}$ immature cells were able to polarize when embedded into the collagen matrix resulting in a morphological distinctive cell front and back (Fig. 20A and B). *WT* cells exhibited a lamellipodia-based migration and continuously repolarized within minutes (Fig. 20A, Mov. S7). They appeared to have several competing leading edges with a multitude of highly dynamic lamellipodia. In contrast, *Hem1*$^{-/-}$ cells maintained their extraordinary unipolar cell shape observed in solution (Compare Fig. 15B and 20B, Mov. S8). The single pointed leading edge was preserved for several minutes and dictated migration direction. Whereas the overall migration velocities of *WT* cells averaged at 2.1 μm/min, sustained hyperpolarization of *Hem1*$^{-/-}$ cells led to a more than doubled average velocity of 4.9 μm/min and maximum velocities of up to 10 μm/min (Fig. 20C). In addition to the pronounced differences in migration speed the chemokinetic behaviour in a uniform CCL3 field was substantially affected. Hence, *WT* cells used short migration trajectories including a multitude of turns and basically kept their starting position (Fig. 20D, left panel Mov. S9). *Hem1*$^{-/-}$ cells exhibited a high directional persistence indicated by long trajectories with very rare turning points (Fig. 20E, Mov. S10). By analysing the mean square displacement (MSD) over time, we were able to distinguish the inherent motility characteristics revealed by the two different genotypes. A linear relation between MSD and time has been termed random walk and is characterized by an unbiased direction of movement completely independent of the preceding moving directions, a stochastic property also called Markov property. Correlations between successive step directions have been described as persistence and are remarked by a non-linear velocity jump in an MSD-time plot. Directional persistence is the result of sustained front-back polarity during migration, which terminates a Markov process. Persistent random migration shows a global unbiased migration but a short-term correlation since the cell is more likely to proceed with movement in the same direction. Using Fürth's formula to parametrically fit the empirically determined displacements, we were able to calculate the persistence time, a parameter that describes the average time a cell migrates without changing its direction. Although the migration trajectories observed resembled a complete random walk, short persistence times of 2.6 ± 1.1
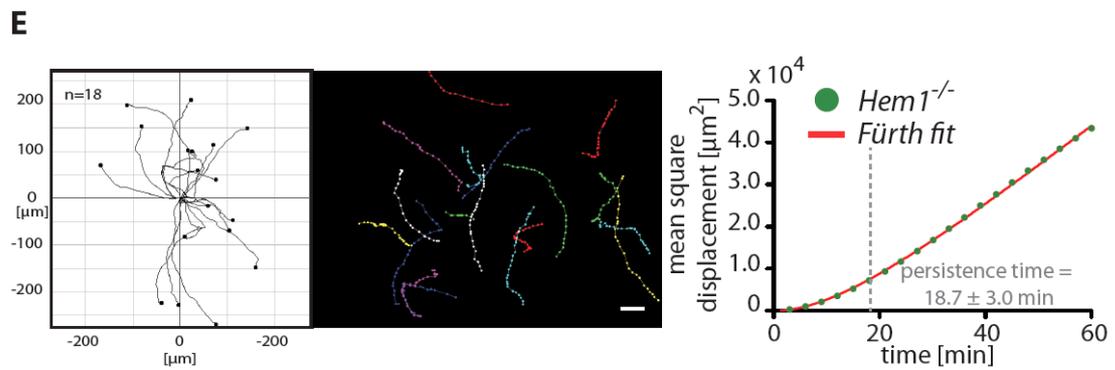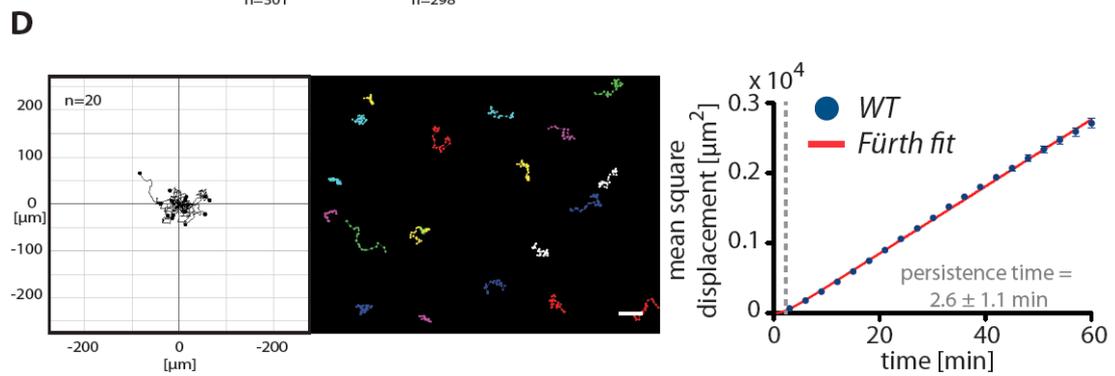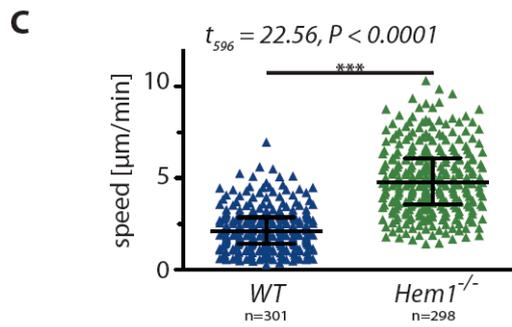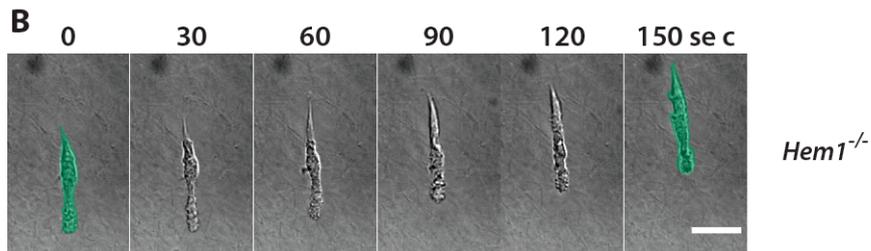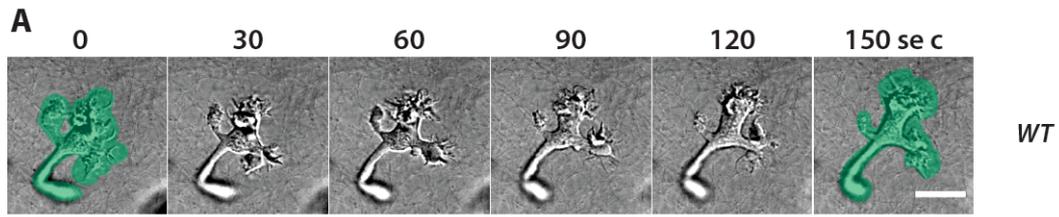
Figure 20. 3D migration behaviour of immature *WT* and *Hem1*-/- BMDCs in a uniform CCL3 field. (A and B) Time-lapse sequences of migrating WT (A) and (B) *Hem1*-/- cells in a 3D collagen gel observed by high-resolution DIC microscopy. Green outlines indicate the start or the end cell morphology, respectively; scale bar, 20 μm. (C) Velocities of single DCs (triangles; black line, median with interquartile range (error bars); n = number of cells tracked); P < 0.0001 (two-tailed student's T-test). (D and E) Single cell tracks of migrating DCs in a uniform CCL3 field; left, normalized to a common start point; mid, actual position in the collagen gel; right, analysis of the mean square displacement (MSD) over time and Fürth fits (red solid line). Symbols, average MSD at a given time point; error bars represent mean ± SEM; calculated from n=120 individual cell tracks (at least three independent experiments).

min could be quantified for *WT* cells (Fig. 20D, right panel). In contrast, *Hem1* deleted cells exhibited a significantly prolonged persistence time, averaging at 18.7 ± 3.0 min as indicated by the polynomial phase of the Fürth fit in the MSD-time plot (Fig. 20E, right panel). Collectively, the random walk-like *WT* chemokinesis is switched to a persistent random walk with a dramatic gain of migration speed upon *Hem1* deletion in immature BMDCs.

Moreover, we could demonstrate that as observed for *WT* cells, integrin-mediated adhesion is *per se* dispensable for migration of *Hem1*-/- cells in 3D collagen matrices. Employment of substrate adhesions was however crucial for locomotion efficiency. Inactivation of integrins by application of EDTA diminished velocities but did not abrogate migration completely (Fig. 21B). In contrast, contractility seems to be obligatory for migration within the applied collagen network densities of both genotypes, as myosin II inhibition by Blebbistatin blocked locomotion entirely (Fig. 21C).

Next we addressed the influence of the increased inherent polarity and persistence on the chemotactic behaviour. Therefore a CCL3 chemokine gradient was applied to the collagen matrices and directional migration was determined as y-displacement towards the CCL3 source using automated imaging analysis as described (Fig. 36). Directional migration along a CCL3 gradient could only be observed for approx. 30 minutes in *WT* cells with continuously rising displacement rates within the first 12.5 minutes followed by a successive decrease for the remaining time until chemotaxis is abolished (Fig. 21A, Mov. S11 and S12). In contrast, no biased migration towards the CCL3 source could be detected for *Hem1*-/- BMDCs within the same time window, or either cell type without a CCL3 gradient (Fig. 21A).
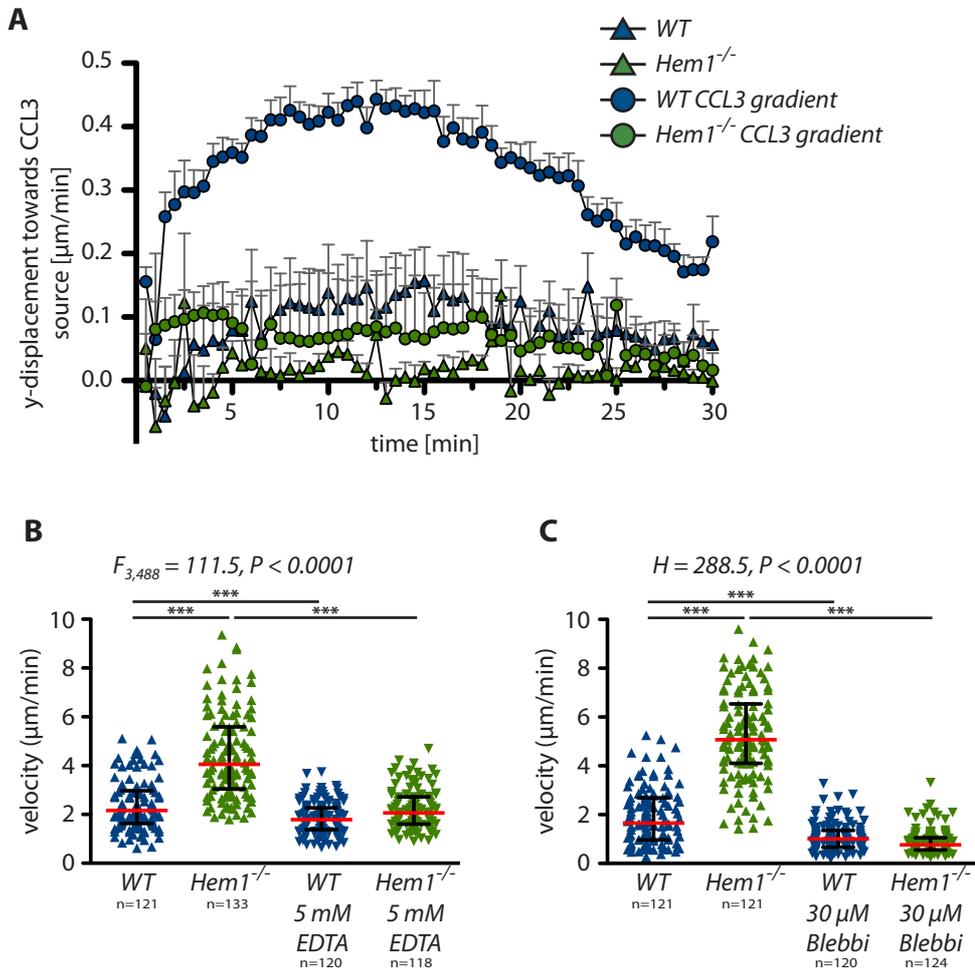
Figure 21. Directional migration of immature *WT* and *Hem1*$^{-/-}$ BMDCs in a CCL3 gradient. (A) Migration over time in the presence (circles) or absence (triangles) of a CCL3 gradient. Directional migration was read out as y-displacement (µm/min) towards the gradient source and quantified as described in Material and Methods. Symbols; average y-displacement at a certain time point; error bars, standard error of the mean calculated from at least three independent experiments. (B and C) Velocities of single DCs (triangles) in the presence or absence of EDTA (B) or Blebbistatin (C), respectively. Red line, mean ± SEM (black error bars); n = number of cells tracked); P < 0.0001 for (B) and (C) (One-way ANOVA). Graphs include data from at least three independent experiments.

Hem1 deletion affects protrusion morphology and dynamics but not protrusion number upon DC maturation

DC maturation leads to highly motile cells that leave the periphery in order to present peripherally acquired antigen to naïve T cells located in the T cell zone of a lymph node (LN). This task is realized by interstitial migration towards the lymphatic system and transportation to the next draining LN via the lymphatic stream. During this process, DCs directionally migrate along an interstitial chemokine gradient that is sensed by the upregulated chemokine receptor CCR7. To assess the consequences of *Hem1* deletion on gradient sensing and directional migration, we performed 3D collagen assays and applied a CCL19 gradient, the soluble ligand of CCR7. Both genotypes showed an amoeboid shape and were able to sense and polarize towards the chemokine source using several dynamic and competing pseudopodia (Fig. 22). Unlike their broad lamellar shape in the *WT, Hem1$^{-/-}$* cells extended less dynamic pointed protrusions towards the chemokine source (Fig. 22A, Mov. S13 and S14). Overall, the altered protrusions did not affect directed migration as *Hem1$^{-/-}$* cells migrated persistently along the CCL19 gradient but reduced migration velocities were detected (Fig. 22B, Mov. S15 and S16). Since preceding studies using different experimental setups observed decreased migration velocities of BMDCs deleted for the other nucleation promoting factor (NPF) WASp, we also included *WASp$^{-/-}$* deficient cells in our setup. *WASp$^{-/-}$* BMDCs were able to polarize and directionally migrate towards CCL19. Compared to *WT* BMDCs, which migrated with on average 2.2 μm/min, *WASp$^{-/-}$* cells indeed showed slightly reduced velocities (1.9 μm/min). Notably, the reduction was less pronounced than for *Hem1$^{-/-}$* BMDCs (1.6 μm/min) (Fig. 22B).

To derive conclusions on the necessity of lamellipodia-shaped protrusions for efficient interstitial migration we confronted the cells with more complex and inhomogeneous environments. This was realized by using rat-tail collagen that polymerizes into a more crosslinked and thus more complex collagen network, with varying collagen concentrations affecting the network's pore sizes (Fig. 22C, lower panel). Increasing the density and complexity of the collagen network reduced the migration velocities of both *WT* as well as *Hem1$^{-/-}$* BMDCs, but with more prominent effects on the latter (Fig. 22C, upper panel). At collagen concentration of 2.3 mg/ml, *Hem1* deleted cells got almost completely stuck in the collagen gel and only basal cell movements reflecting cell protrusions transiently extended into the surrounding matrix could be observed.

A

B

$F_{2,536} = 40.82, P < 0.0001$

C
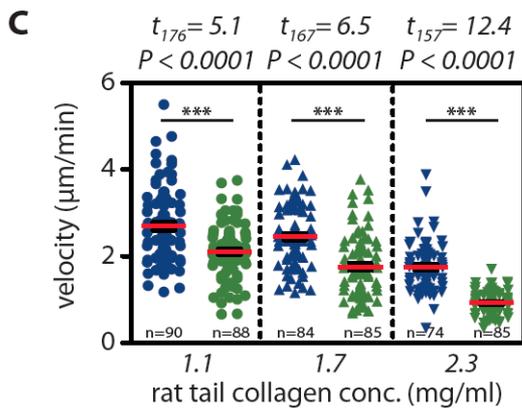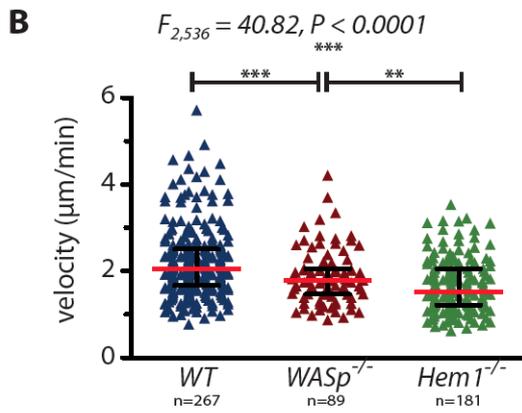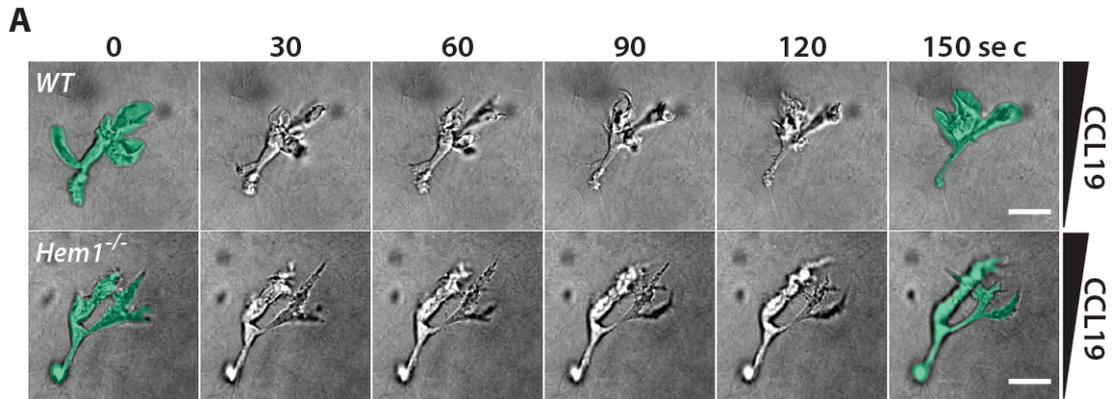
$t_{176} = 5.1$ $t_{167} = 6.5$ $t_{157} = 12.4$
$P < 0.0001$ $P < 0.0001$ $P < 0.0001$

Figure 22. Directional migration of mature *WT* and *Hem1*^{-/-} BMDCs in a CCL19 gradient. (A) Time-lapse sequences of migrating cells in a 3D collagen gel observed by high-resolution DIC microscopy. Green outlines indicate the start or the end cell morphology, respectively; scale bar, 20 µm. (B) Velocities of single *WT* (blue triangles), *WASp*^{-/-} (red) or *Hem1*^{-/-} (green) DCs, respectively. Red line, median with interquartile range (error bars); n = number of cells tracked; P < 0.0001 (One-way ANOVA). Graphs include data from at least three independent experiments. (C) Velocities of single *WT* (blue triangles) or *Hem1*^{-/-} (green) DCs, respectively, depending on increasing rat tail collagen concentrations (left to right, upper panel). The complexity of the collagen matrix acquired by confocal reflection microscopy is shown in the lower panel. Red line, mean ± SEM (black error bars); n = number of cells tracked; P < 0.0001 for all collagen concentrations (two-tailed student's T-test). Graphs include data from at least three independent experiments.

Impaired migration of *Hem1* deleted DCs can be recapitulated *in vivo*

To validate our *in vitro* findings in a more physiological setup we investigated the consequences of the *Hem1* knockout on the migration along *in vivo* chemokine gradients. First we co-injected 1:1 ratios of differently labelled *WT* and *Hem1*^{-/-} BMDCs subcutaneously (Fig. 23A) into mouse footpads and quantified their arrival in the draining LN using FACS analysis (Fig. 23B). We also examined the effect of *WASp* ablation. Migration was inhibited approx. 1.5-fold in *WASp*^{-/-} cells compared to *WT* 24 hrs post injection. Only approx. half the number of *Hem1*^{-/-} BMDCs reached the LN compared to the *WT*. Thus, the *in vitro* measured differences in migration velocities translated into an even more pronounced difference in an *in vivo* BMDC homing assay.

Next, to assess the ability of *Hem1*^{-/-} BMDCs to migrate along interstitial gradients, we used an *in situ* end point approach to observe BMDC arrival and transmigration into the lymphatic vessels (Pflicke and Sixt, 2009). Therefore, 1:1 ratios of differently labelled *WT* and *Hem1*^{-/-} BMDCs were placed onto tissue explants of split mouse ears. This exposes cells to endogenous gradients of CCL21, the immobilized ligand of CCR7, and triggers cell entry of the interstitium and subsequent directional migration to nearby lymphatic vessels (Weber et al., 2013). Two hours after exposure, the assay was stopped by fixation and a snapshot of lymph vessel entry at this time point was acquired. A representative picture is shown in Fig.
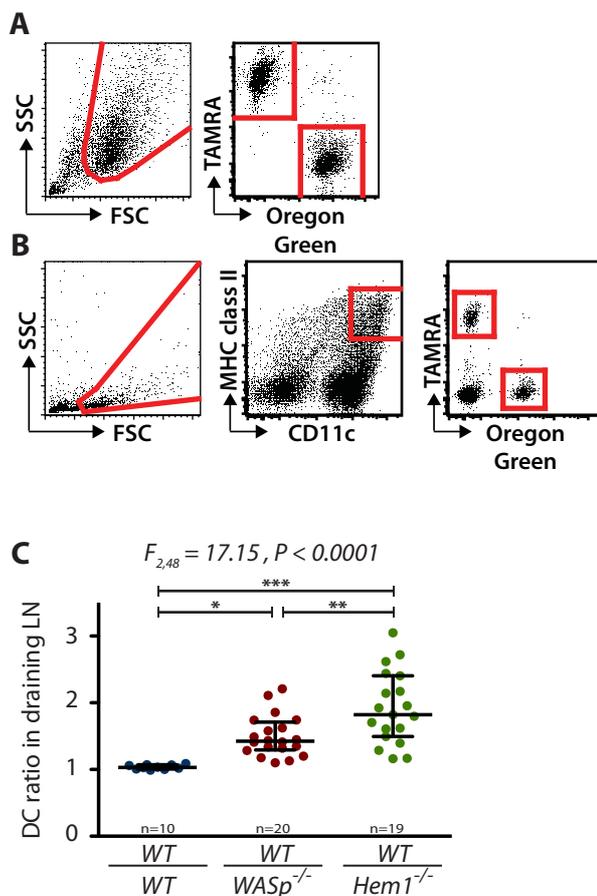
Figure 23. DC migration to draining lymph nodes. A 1:1 mix of *WT/WT, WT/WASp*^{-/-} or *WT/Hem1*^{-/-} mature BMDCs labelled with Oregon Green® or TAMRA, respectively, were injected into the footpad of *WT* recipient mice. (A) Representative dot plot of the injected cell mixture. (B) Gating strategy to recognize the injected WT and *Hem1*^{-/-} BMDCs in the draining (popliteal) lymph nodes 24 h after injection. Cells were first gated according to their cell size before they were accurately identified by the CD11c+MHCII[high] expression and their corresponding fluorescent label. Gates are highlighted in red (A and B). (C) Quantification of the DC arrival in the LN. Cell ratios were calculated from the absolute BMDC numbers arrived in the lymph node and normalization to the initially injected ratio to correct for unequal injection ratios. Dots represent relative ratios acquired from a single experiment. Black line, median with interquartile range (error bars); n = number of experiments. Fluorescent labelling for each injection pair was inverted in half of the experiments to exclude labelling influences.
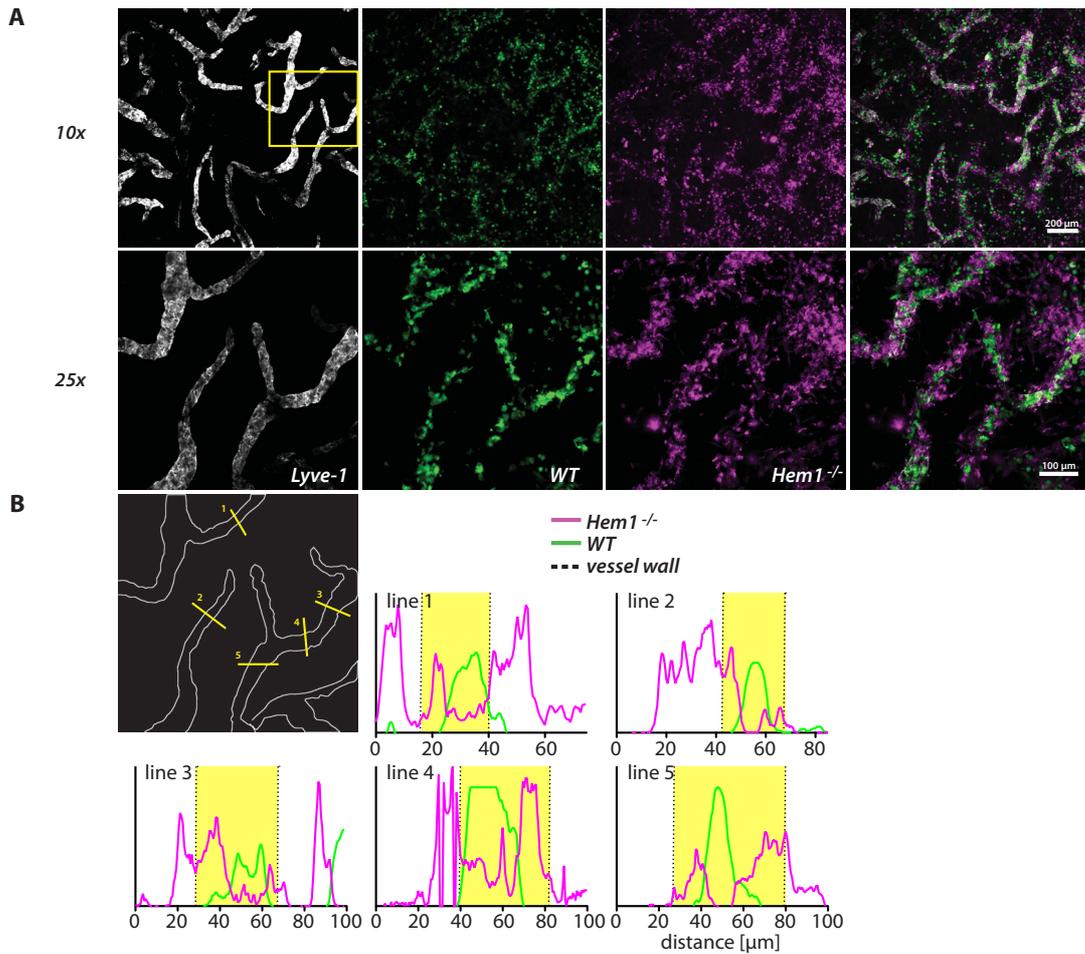
Figure 24. Interstitial migration of DCs within the dermis of ear explants. Endpoint of ear crawl-in assay. A 1:1 mix of *WT/WT*, or *WT/Hem1*^{-/-} mature BMDCs labelled with eFluor® 670 or TAMRA, respectively, was applied to ventral ear sheets to allow for interstitial migration towards the lymphatic vessel. Maximum intensity Z-stack projections of confocal fluorescence image series of the mouse ear immunostained for Lyve1^{+} lymphatic endothelial cells (LECs, white) and fluorescence-labelled *WT* (green) and *Hem1*^{-/-} mature BMDCs (magenta) after 2 hours of migration (upper panel). Higher magnification pictures (middle panel) of a selected area (yellow box, upper panel). (B) Line intensity histograms across the lymph vessel (LV) diameter (yellow lines, left image, white lines correspond to LV outlines) show fluorescent signal distribution of *WT* (green line) and *Hem1*^{-/-} BMDCs (magenta line). Dashed line, vessel walls; yellow background, vessel lumen.

24A. *WT* as well as *Hem1*^{-/-} BMDCs had efficiently approached the lymphatic vessels at this time point. However, whereas most of *WT* cells had already entered the lymphatic vessels (indicated by a cell rounding in the vessel lumen) (Fig. 24A, green), transmigration of *Hem1* deleted cells appeared to be delayed (indicated by the elongated and dendritic morphology of the cells) (Fig. 24A, magenta). Using line histogram analysis we could confirm that indeed most of the knockout cells were either still outside the vessels or aligned with the vessel walls (Fig. 24B). Whether the delayed transmigration of *Hem1*^{-/-} BMDCs is a consequence of a reduced interstitial migration velocities or an impaired transmigration or both could not be clarified in this end point setup

Actin assembly and dynamics of migrating Hem1$^{-/-}$ BMDCs

This section summarizes the insight we gained into actin assembly and dynamics of *Hem1* deficient BMDCs during the actual migration process. Using TIRF microscopy we mapped GFP-fusions of actin, actin nucleators or elongators during cell locomotion in a confined 2D setup. Therefore, cells were placed between a coverslip and an agarose layer to provide cell confinement allowing for adhesion-independent migration (Renkawitz et al., 2009).

Absence of integrin coupling leads to differences in leading edge actin dynamics between mature *WT* and *Hem1$^{-/-}$* BMDCs

First, in order to visualize the consequences of WAVE ablation on actin dynamics during migration we employed the F-actin marker Lifeact (Riedl et al., 2008). When migrating on adhesive glass surfaces, cells transfected with Lifeact-GFP formed broad leading edges exhibiting actin enrichment within the first few micrometres just behind the leading membrane (Mov. S17 and S18). The broad lamellipodium is followed by a more compact cell body and trailing edge in which thicker actin bundles could be detected. No significant difference could be seen between *WT* and *Hem1$^{-/-}$* cells. As shown previously (Renkawitz et al., 2009), actin at the leading edge remained stationary relative to the substrate during cell advancement as demonstrated by the vertical lines in the corresponding kymograph analysis along the central length axis of the cell (Fig. 25A and B). Thus, the absence of a retrograde actin flow proved efficient force coupling to the substrate and an entire conversion of polymerization into protrusion in both genotypes. On the other hand, different actin dynamics between *WT* and *Hem1$^{-/-}$* cells could be induced using inert PEG surfaces that prevent coupling to the substrate. While *WT* cells responded with enhanced actin polymerization at the leading edge (Mov. S19), *Hem1$^{-/-}$* cells were apparently unable to adapt their actin polymerization rate (Mov. S20). In order to compensate for missing integrin-coupling and to maintain protrusion velocity, massive actin polymerization could be observed in a zone of 3-4 μm behind the leading membrane in *WT* cells. Consistent with previous findings, this resulted in a substantial retrograde flow of F-actin towards the cell centre, as derived from diagonal lines in the corresponding kymograph (Fig. 25C). Although retrograde flow was also induced when migrating on PEG surfaces, *Hem1* depleted BMDCs did not show upregulated actin polymerization. Moreover, the more vertical diagonals in the kymograph analysis of the *Hem1$^{-/-}$* cells indicated a lower retrograde flow resulting from a lower actin polymerization rate compared to the *WT* (Fig. 25D).

Taken together, whereas actin dynamics under adhesive conditions seems to be unchanged upon WAVE ablation, regulation of actin polymerization rate in the absence of integrin coupling is disturbed.
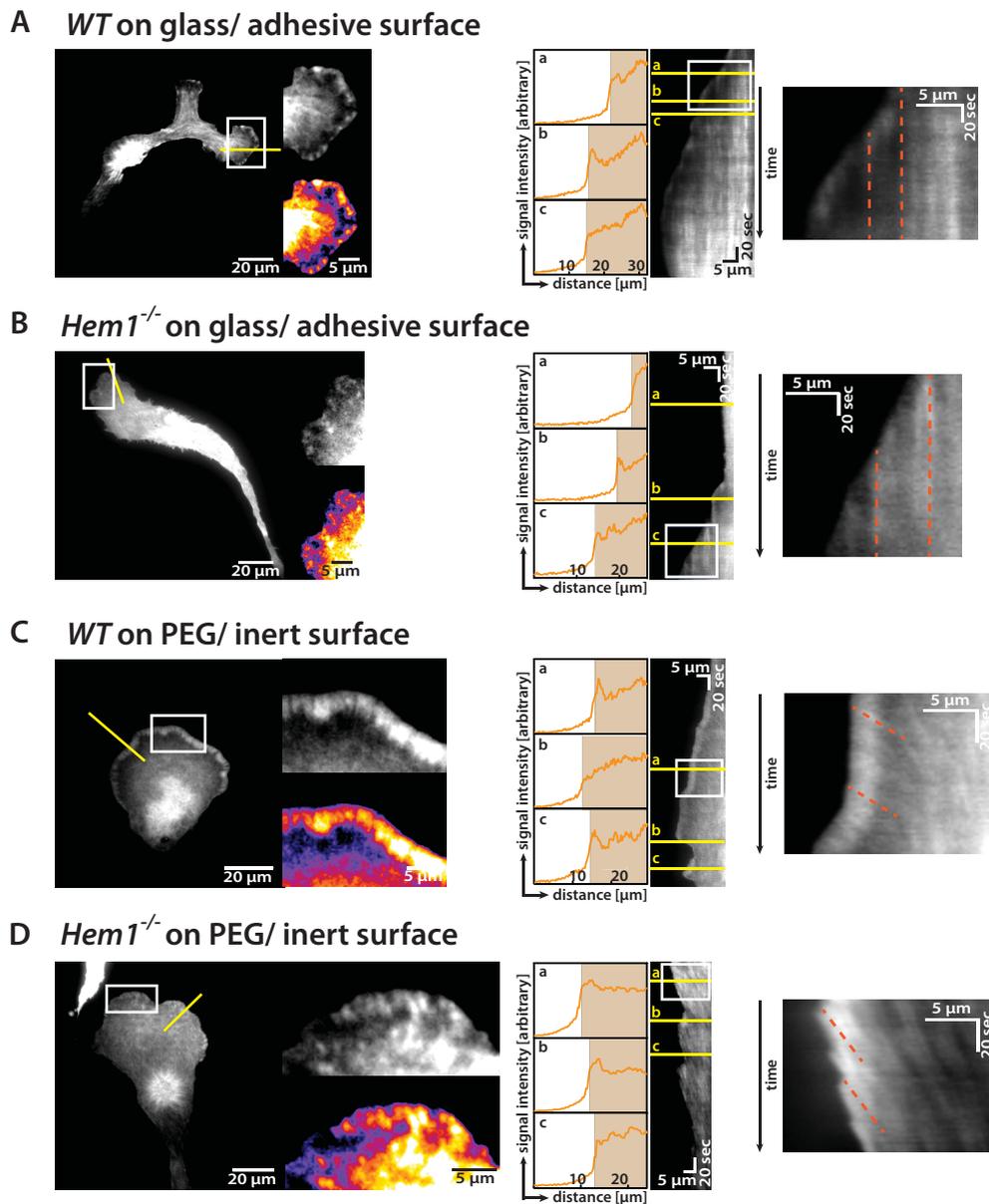
Figure 25. Actin dynamics in migrating BMDCs. TIRF images of Lifeact–GFP-transfected DCs migrating on adhesive glass (A and B) or non-adhesive (C and D) PEG-coated coverslip under agarose. *Left panels*: Exemplary pictures of migrating cells (grey scale) and a magnified region (white box) of the leading edge (grey scale and false colour) are shown for mature *WT* (A and C) and *Hem1*^{-/-} (B and D) cells. *Middle panel*: Kymograph analysis (right, grey scale) show the development of the line segment (yellow line) marked in the left panel (cell overview) over time. Three exemplary line intensity histograms show the fluorescent Lifeact-GFP signal distribution along the kymograph line at three distinct time points (a-c). Brown backgrounds of the line intensity histograms indicate the cell interior. Membrane edges correspond to a background colour switch from brown to white. *Right panel*: Magnified regions of the kymograph (white box) qualitatively indicate for retrograde flowing actin. Lifeact-GFP signals that keep their position over time result in vertical patterns (orange dashed lines in A and B) and refers to the absence of a retrograde actin flow. Diagonal downward orientated signal patterns point to retrograde moving actin (orange dashed lines in C and D). The faster actin flows backward, the more horizontal the signal pattern gets. (A and C).

WASp associates with the lamellipodial membrane and might activate Arp2/3 independent of the WAVE complex

Our previous findings could show that actin branching and lamellipodia formation is possible in the absence of a functional WAVE complex. Consistently, no significant differences in actin dynamics at the leading edges of *WT* and *Hem1* deficient cells could be observed for migration on an adhesive glass substrate (Fig. 25A and B). Here we directly observed Arp2/3 dynamics at the leading edge and a possible alternative activation by WASp in the absence of WAVE complex. In agreement with the observations described above, transfection of the GFP-labelled Arp2/3 subunit p16-Arc/ArpC5 revealed that Arp2/3 complex could still be recruited to the leading membrane in the absence of Hem1 (Fig. 26B). In both genotypes, when migrating on a non-adhesive substrate, Arp2/3 complex accumulates at the protruding membrane and drains backwards with the substrate-induced enhanced retrograde flow (Fig. 26A and 26B, as well as Mov. S21 and S22). Surprisingly and controversial to previous studies we could identify WASp accumulating in a thin and defined rim at the most distal edge of the leading membrane (Mov. S23 and S24). Kymograph analysis illustrated WASp accumulation with the onset of membrane protrusions and its absence during retraction in both *WT* and *Hem1*^{-/-} cells (Fig. 27). Thus, WASp can be recruited to the leading membrane in the presence and absence of WAVE complex facilitating unaltered Arp2/3 complex activation.

A *WT* on a PEG (inert) surface

B *Hem1*^{-/-} on a PEG (inert) surface
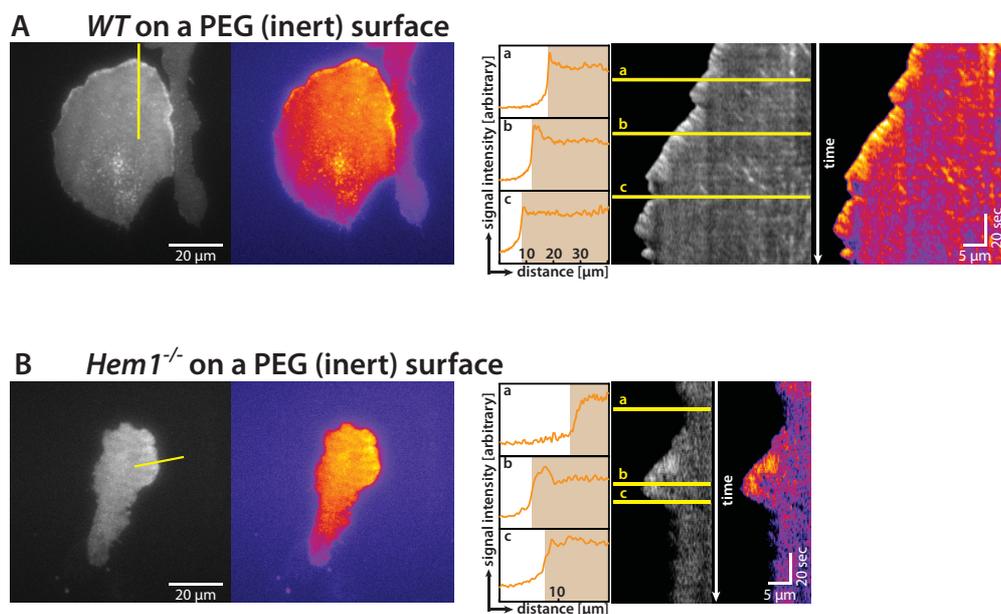
Figure 26. Arp2/3 dynamics in migrating BMDCs. TIRF images of ArpC5–GFP-transfected DCs migrating on a PEG-coated coverslip under agarose. *Left panels:* grey scale and false colour images of migrating mature *WT* (A) and *Hem1*^{-/-} (B) BMDCs. *Right panels:* Kymograph analysis (middle and right picture, grey scale and false colour picture) show the development of the line segment (yellow line) marked in the left panel (cell overview) over time. Three exemplary line intensity histograms (right panel, left picture, a-c) show the fluorescent signal distribution of Arp2/3 along the kymograph line at three distinct time points (a-c). Brown backgrounds of the line intensity histograms indicate the cell interior. Membrane edges correspond to a background colour switch from brown to white.

Figure 27. WASp dynamics in migrating BMDCs. TIRF images of WASp–GFP-transfected DCs migrating on a PEG-coated coverslip under agarose. Three exemplary migrating cells (grey scale) and a magnified region (white box) of the leading edge (grey scale and false colour) are shown for mature *WT* (A) and *Hem1*⁻/⁻ (B) cells. *Upper right panel:* Kymograph analysis (right, grey scale) show the development of the line segment (yellow line) marked in the upper left picture (cell overview) over time. Three exemplary line intensity histograms show the fluorescent WASp signal distribution along the kymograph line at three distinct time points (a-c). Brown backgrounds of the line intensity histograms indicate the cell interior. Membrane edges correspond to a background colour switch from brown to white.

Loss of WAVE leads to VASP depletion at the leading edge

So far, our observations point out a concomitant activation of the Arp2/3 complex by WASp and WAVE complex at the leading edge of BMDCs. However, lower migration velocities in 3D and reduced actin polymerization on non-adhesive substrates in 2D confinement argue for alterations in actin dynamics in *Hem1* depleted BMDCs. The actin elongator VASP has been found at the leading edge of lamellipodia and filopodia as well as in the formation of focal complexes and adhesions. There it promotes actin polymerization required for efficient cell advancement. Recently, a biochemical study reported a physical interaction between Abi1, a component of the WAVE complex and VASP (Dittrich et al., 2010; Maruoka et al., 2011; Tani, 2003). Therefore, we investigated the consequences of loss of *Hem1* and the subsequent Abi1 degradation on VASP localization during migration. Transfection of VASP-GFP verified its recruitment to focal adhesions and the leading membrane of *WT* cells. At the latter VASP localised in a defined small rim confirming direct binding to the membrane during a protrusion phase (Fig. 28A, Mov. S25). Non-adhesive substrates prevented focal complex formation and VASP localisation (Fig. 28C, Mov. S27). Remarkably, VASP recruitment to the protruding membrane was completely abolished in the absence of WAVE complex but localisation to focal complexes was unaffected (Fig.28B, Mov. S26). Furthermore, interference with focal complex formation led to an unspecific VASP distribution indicated by a diffuse GFP signal over the whole cell (Fig. 28D, Mov. S28). In summary, Hem1 seems to be required for VASP localisation to the leading membrane and its absence might explain reduced actin polymerization rates in *Hem1*^{-/-} BMDCs.

79
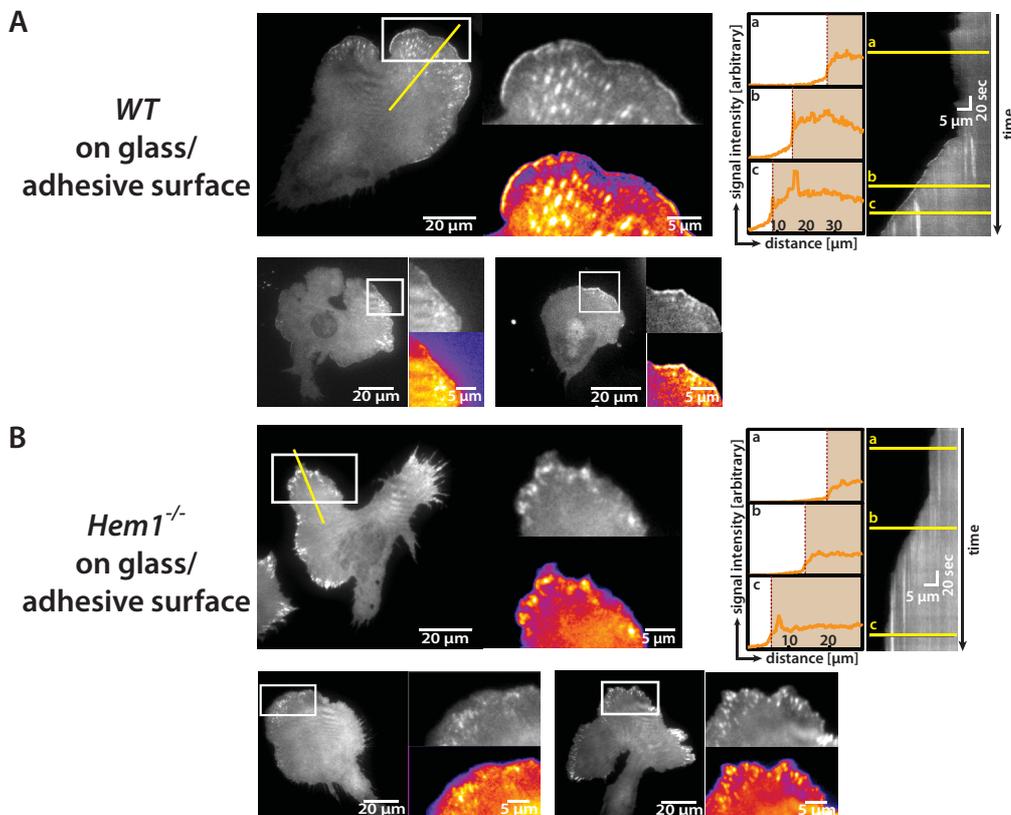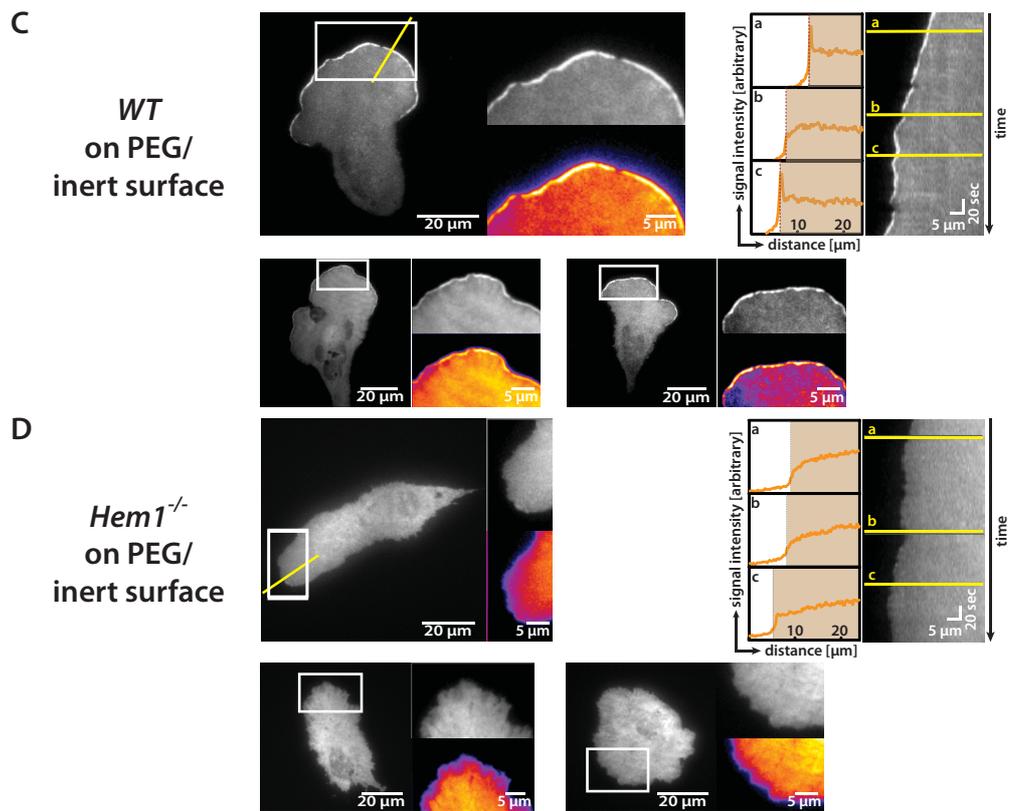
Figure 28. VASP dynamics in migrating BMDCs. TIRF images of VASP–GFP-transfected DCs migrating on adhesive glass (A and B) or non-adhesive (C and D) PEG-coated coverslip under agarose. Three exemplary migrating cells (grey scale) and a magnified region (white box) of the leading edge (grey scale and false colour) are shown for mature *WT* (A and C) and *Hem1*^{-/-} (B and D) cells. *Upper right panels*: Kymograph analysis (right, grey scale) show the development of the line segment (yellow line) marked in the left panel (cell overview) over time. Three exemplary line intensity histograms show the fluorescent VASP-GFP signal distribution along the kymograph line at three distinct time points (a-c). Brown backgrounds of the line intensity histograms indicate the cell interior. Membrane edges correspond to a background colour switch from brown to white.

Generation of WAVE and WASp depleted BMDCs

Approach, hope and fail

The preceding data indicated an alternative Arp2/3 complex activation by WASp that can partially compensate the absence of the WAVE complex at the leading edge of migrating BMDCs. This pathway seems to occur irrespective of the presence of WAVE but strongly depends on the maturation process. Thus, we hypothesised an exclusive WAVE-dependent actin branching within the leading edge of immature BMDCs, and that WAVE ablation caused the observed phenotype. In contrast, WASp recruitment at the leading membrane was enabled upon maturation and could partially resume Arp2/3 activation in the absence of WAVE complex leading to the rather mild phenotype described above.

In order to directly prove this scenario we aimed for a genetic approach disabling both, WASp- and WAVE-dependent Arp2/3 activation. First, we tried to generate a constitutive double-deficient mouse for WASp and WAVE by cross-breeding *WASp$^{-/-}$* and Hem1$^{-/-}$ mice. Since both genes are exclusively expressed in the hematopoietic compartment, the double knockout would have only affected the corresponding cells. Among 78 pups born from several crossings of male *Hem1$^{+/-}$ x WASp$^{-/y}$* and female *Hem1$^{-/+}$ x WASp$^{+/-}$*, not a single viable *Hem1$^{-/-}$ x WASp$^{-/-}$* animal was obtained (Fig. 29A, grey bars). Since one could expect the appearance of double knocked out animals with a probability of 12.5% ($\approx$10 animals if n=78, Fig. 29A, red bars) in case of an unaffected viability, we concluded a prenatal mortality for *Hem1$^{-/-}$ x WASp$^{-/-}$* animals.

Next, we tried to circumvent the apparent embryonic lethality of the constitutive double knockout by crossing mice constitutively knocked out for *WASp* with mice harbouring LoxP-flanked sites comprising exons 4 and 5 of the *Hem1* gene. The combination of the constitutive knockout of only *WASp* with the conditionally targeted *Hem1* gene guaranteed the generation of viable animals and allowed for a subsequent deletion of *Hem1 in vitro.* Thus, exons 4 and 5 of *Hem1* were excised by recombination applying a site-specific Cre-recombinase during BMDC culture. This Cre recombinase was molecularly engineered by fusing it with a basic peptide derived from HIV-TAT to promote cellular uptake and a nuclear localization signal (NLS) to enable nuclear distribution (Peitz et al., 2002). To visualize active recombination and genetic deletion we additionally crossbred a fluorescent recombination indicator (*mTmG* transgene)(Muzumdar et al., 2007). This transgene is harbouring a LoxP-flanked membrane-targeted *dTomato* and stop codon followed by an unflanked membrane-targeted *GFP*. The transgene is transcribed across the *dTomato* until it is terminated by the stop codon leading to red fluorescent cells. Active recombination by TAT-Cre deletes both the *dTomato* and the stop codon enabling the expression of *GFP*. Switching from red to green fluorescence indicates active recombination in a cell and displays successful deletion of the *Hem1* gene (Fig. 29B). Furthermore, using FACS sorting we were able to discriminate and purify green fluorescent *Hem1$^{-/-}$ x WASp$^{-/-}$* cells from red non-recombined *Hem1$^{fl/fl}$ x WASp$^{-/-}$* cells (Fig. 29B, lower panel). As shown in Fig. 29C we were able to successfully transfect BMDCs with TAT-Cre during BMDC differentiation leading to

A

B

Muzumdar *et al.*, Genesis 2007

TAT-NLS-Cre

Peitz *et al.*, PNAS 2002
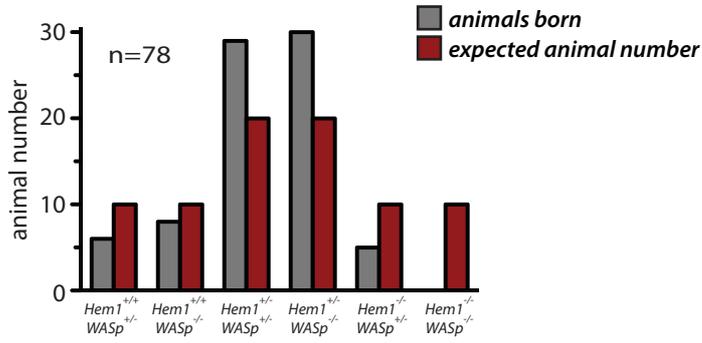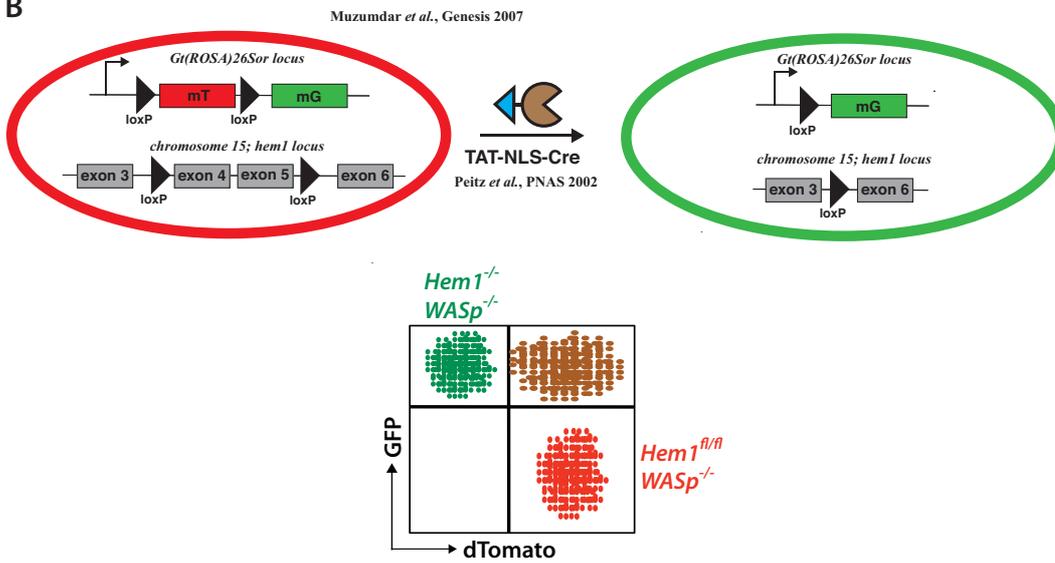
C
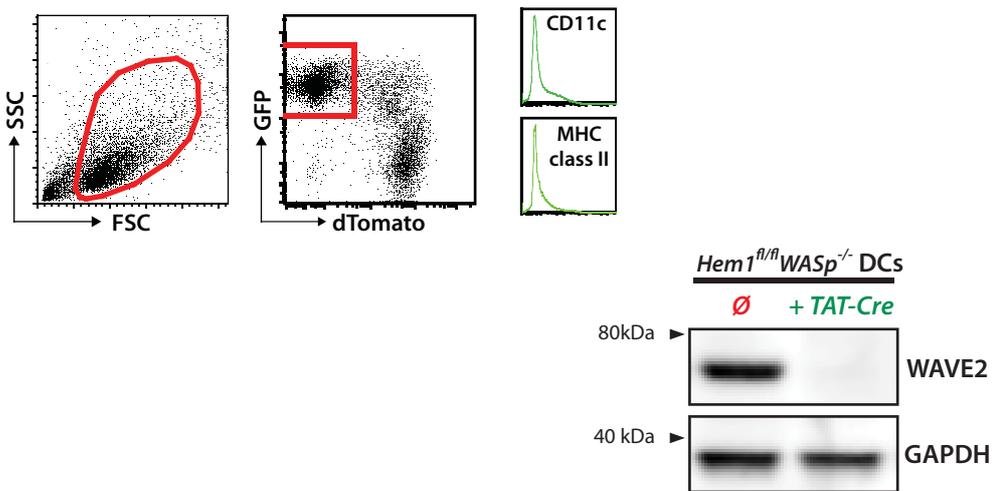
a

Figure 29. Generation of *Hem1*^{-/-} x *WASp*^{-/-} (double knocked out, dKO) BMDCs. (A) Breeding results of *Hem1*^{+/-} x *WASp*^{+/-} and *Hem1*^{+/-} x *WASp*^{-/-} crossings (red) and the expected outcome (grey). n, number of animals born. (B) Alternative strategy to generate dKO BMDCs. Exons 4 and 5 of *Hem1* were conditionally targeted by flanking LoxP sites. *Hem1*^{fl/fl} x *WASp*^{-/-} DCs were treated with Tat-Cre recombinase *in vitro*. To identify *Hem1* deleted cells, a fluorescent recombination indicator (*mTmG* transgene) was additionally introduced. The transgene harbours a LoxP-flanked membrane-targeted *dTomato* and stop codon followed by an unflanked membrane-targeted *GFP*. Active recombination then leads to a switch from red to green fluorescence. (C) Gating strategy to identify and purify dKO BMDCs from *Tat-Cre* treated *Hem1*^{fl/fl} x *WASp*^{-/-} BMDCs. Surface expression of CD11c and MHCII of the GFP⁺ LPS-treated presumable dKO cells was checked by FACS (histograms). WAVE2 expression of untreated and Tat-Cre treated GFP⁺-sorted *Hem1*^{fl/fl} x *WASp*^{-/-} BMDCs was checked by Western blot (lower panel). GFP, green fluorescent protein; MHCII, MHC class II; LPS, lipopolysaccharide.

pronounced population expressing *GFP*. In addition, we could verify that positive recombination of the transgene corresponds to the deletion of *Hem1* resulting in the ablation of WAVE complex (Fig 29C, lower panel). Unfortunately, FACS analysis of the double-deficient (green) cells at the end of BMDC culture revealed lack of expression of DC markers such as CD11c and MHCII. Hence, choosing a conditional approach could circumvent the apparent embryonic lethality of the constitutive double knocked out animals but ultimately proved an impaired BMDC differentiation upon deletion of *WASp* and *Hem1*. Consequently, we were not able to verify our hypothesis that DC maturation enables WASp-dependent actin branching in lamellipodia of migrating BMDCs.

Preliminary Observations

An alternative migration mode of immature *Hem1*-deficient BMDCs

Hem1 deletion in immature BMDCs has been shown to result in a remarkable morphological phenotype accompanied by a pronounced gain in migration persistence and velocity. In addition to these observations we noticed continuous membrane waves originating from the cell tip moving laterally towards the cell body (Mov. S30). Based on this finding we hypothesized a mechanism the cell could employ for forward movement. By coupling or entangling the retrograde moving membrane waves with the surrounding substrate the cell could generate traction pushing the whole cell forward. This caterpillar-like mechanism uses continuous retrograde waves resulting in a constant and smooth gliding of the cell through the ECM. In order to obtain evidence for this mechanism we performed kymograph analysis of migrating immature *Hem1*^{-/-} BMDCs in a 3D collagen matrix (Fig. 30A, Mov. S29). Using kymograph lines parallel to the cell's anterior-posterior axis we obtained the directional information of the movement of cellular flows relative to the substrate. Kymograph analysis of lines tangential to the cell body represented the behaviour of membrane flows whereas a kymograph line through the cell body exhibited the cytoplasmic flow. Kymograph analysis of the membrane waves revealed diagonal downward running lines (orange dashed lines)

A *Migrating Hem1$^{-/-}$ iDC in 3D collagen matrix*
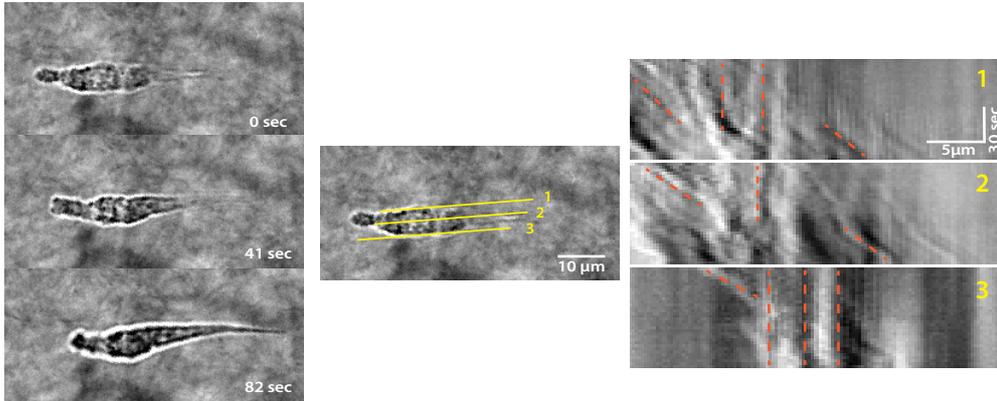
B *Stuck Hem1$^{-/-}$ iDC in 3D collagen matrix*
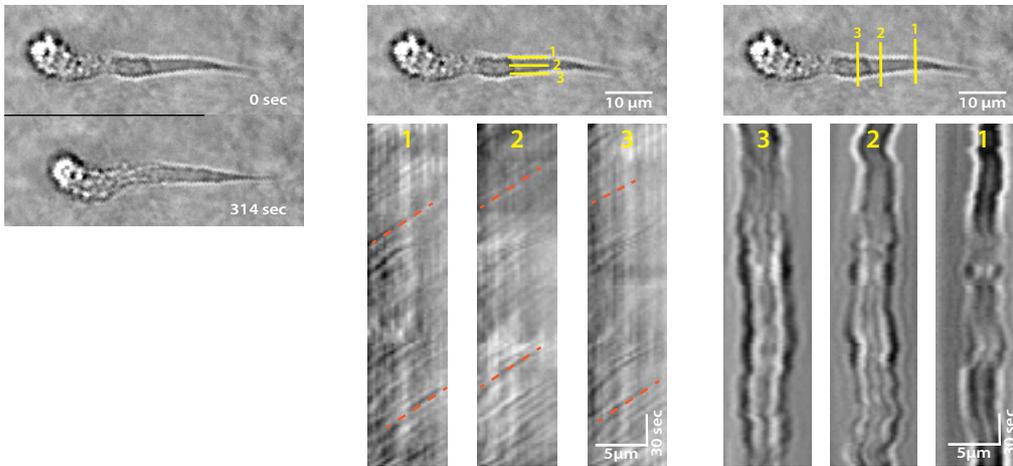
C
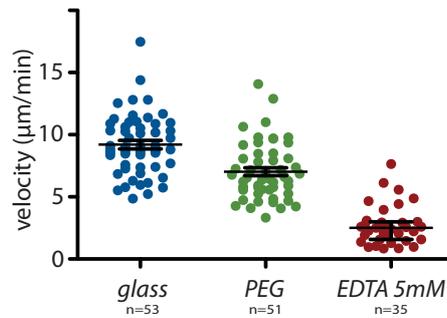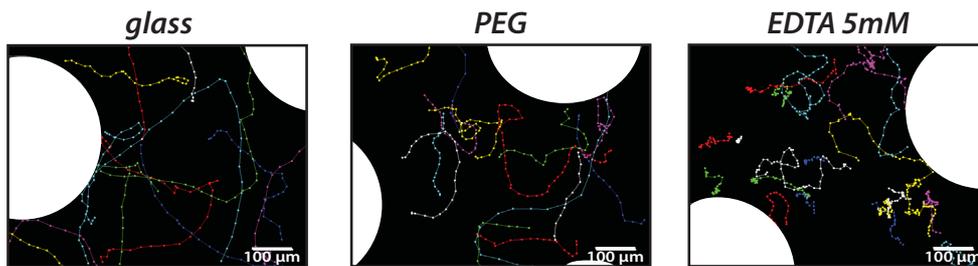
Figure 30. Locomotion of immature *Hem1*-/- by dynamic cell shape changes. (A and B) Migration behaviour and membrane dynamics of *Hem1*-/- BMDCs was observed in a 3D collagen gel. DIC image sequence of a migrating cell (A, left) and a stuck cell (B, left). Membrane dynamics were observed using kymograph analysis of tangential line segments representing the membrane (*middle*, 1 and 3). Cytoplasmic dynamics was determined by a line segment through the cell length (*middle*, 2). (Only in B, *right*) Kymograph analysis of line segments across the cell width (C) Cell migration under confined conditions. Cell trajectories (upper panel) and the measured migration velocities according to the denoted condition. White areas correspond to the position of the confinement pillars.

reflecting an overall forward progress of the membrane point and vertical patterns demonstrating its stationary fate. The first indicates that forward progress exceeds retrograde movement of the membrane wave; the latter refers to a membrane point that remains stationary relative to the substrate pointing to an entanglement with the ECM. The cytoplasmic flow showed a general forward movement but some static situations could be observed. In contrast, a cell that got stuck in the ECM and could not move forward showed both continuous retrograde flow of membrane waves and cytoplasmic stream (Fig. 30B, left kymographs, Mov. S30). In addition we performed kymograph analysis of lines perpendicular to the central length axis of the cell that demonstrated the independence of the movement behaviour of the lateral membrane waves on each side of the cell axis (Fig. 30B, right kymographs). As shown in Fig. 21, the migration of *Hem1*-/- BMDCs completely relies on myosin-driven contractility (Fig. 21C) and to a certain amount on integrin-dependent adhesion (Fig. 21B). In order to test the necessity of integrin-dependent adhesion for the transduction of retrograde membrane movement to the substrate that ultimately leads to the translation into forward progression, we observed cell migration in a confined setup and interfered with cell adhesion using either PEG-coated non-adhesive substrates or inactivated integrins by the application of EDTA (Fig. 30C). The confinement allowed for "chimneying" on a 2D substrate and hence is independent of integrins (Lämmermann and Sixt, 2009). As in 3D, migration on an adhesive glass surface was fast and highly persistent whereas the inert PEG surface resulted in a slight decrease in speed as well as in persistence indicated by an increase in trajectory curvature (Fig. 30C). Cells also showed a higher tendency to form a new cell protrusion accompanied by a change in direction (Compare Mov. S31 and S32). In contrast, EDTA caused an almost complete loss in traction and cells were largely floating rather than performing active migration, leading to a significant decrease in velocity and persistence (Mov. S33). Since EDTA sequesters Mg^{2+} and Ca^{2+} ions that are important for contractility, the observed phenotype could be a combined result of loss of adhesion and an impaired contractility. The latter would hint at the involvement of myosin-driven retrograde membrane waves.

Impaired T cell interaction following *Hem1* deletion

Beside its role in BMDC migration we were wondering about the necessity of actin branching for aspects of DC physiology. Upon migration to the next draining lymph node a DC presents its peripherally acquired antigen to naïve T cells. T cells carrying a T cell receptor (TCR) that

A

B
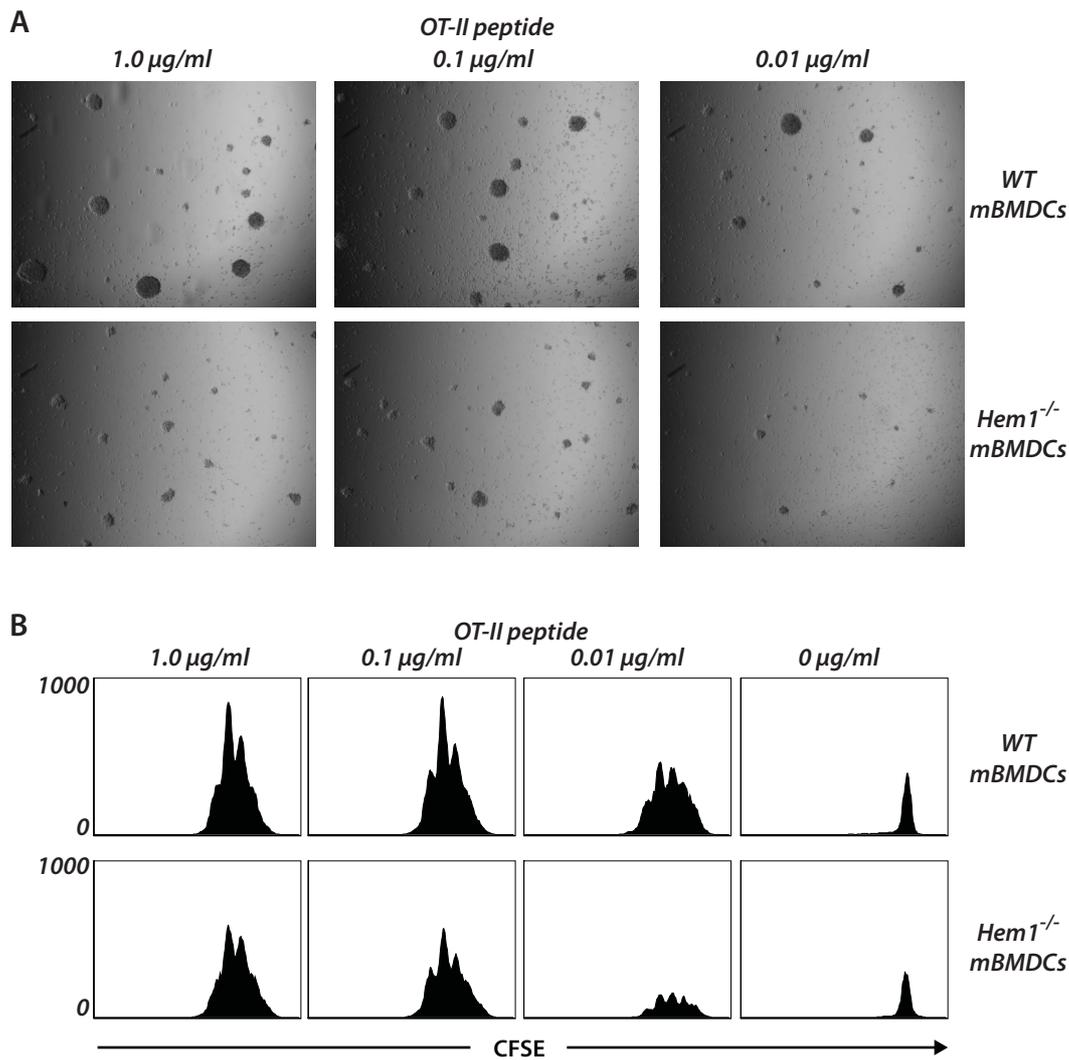
Figure 31. CD4+ T cell priming induced by *WT* and *Hem1−/−* BMDCs *in vitro*. *WT* and *Hem1−/−* BMDCs were mixed with CFSE-labelled OVA-specific OT-II T cells. T cell priming was induced by the addition of increasing doses of MHC class II-restricted OVA peptide. T cell proliferation was observed 3 days post induction. (A) Bright field microscopy images: Overview of DC-T cell cluster sizes and numbers according to the OVA peptide concentration applied. (B) T cell proliferation was measured by flow cytometry. Cell divisions result in the successive dilution of the CFSE label. Histogram plots represent the CFSE dilution profile of OT-II T cells for the indicated OVA peptide doses. Histogram peaks correspond to the number of T cell divisions. Data are representative for at least three independent experiments.

recognizes the cognate Ag presented by the DC are able to bind to and stably interact with the DC. The formed cell-cell interaction is referred to as immunological synapse (IS) and results in T cell proliferation. A dynamic actin cytoskeleton on both sides of an immunological synapse has been shown to be important for the priming of naïve T cells(Al-Alwan et al., 2003; Benvenuti et al., 2004; Calvez et al., 2011; Dustin and Cooper, 2000; Pulecio et al., 2010). To what extent and at which points during IS formation and subsequent signalling events

WAVE-dependent Arp2/3 activation is required for the actin cytoskeletal dynamics on the DC side is still unknown. In order elucidate this open issue we performed an *in vitro* T cell proliferation assay. Therefore, we mixed CFSE-labelled T cells carrying the TCR specific for MHCII-presented ovalbumin (OVA) peptide with mature *WT* or *Hem1*$^{-/-}$ BMDCs. To enable the formation of an IS and to get information on the signalling strength we applied different concentrations of OVA peptide resulting in differing OVA-loaded MHCII molecule densities. Positive T cell priming is visualized and can be measured by CFSE dilution using flow cytometry: each T cell division results in the bisection of the CFSE signal intensity and cell divisions refer to the peak numbers in a CFSE histogram. During bright field microscopic observations we could see pronounced differences in cell cluster size, indicating differences in T cell proliferation capability (Fig. 31A). The cell cluster sizes were much higher when stimulated with *WT* BMDCs compared to T cells primed by *Hem1*$^{-/-}$ BMDCs. Moreover, the corresponding CFSE dilution showed the same number of T cell generations (indicated by the same peak number), however, a significantly reduced number of T cells that could be recovered from the assay (Fig. 31B). These findings suggest that *Hem1*$^{-/-}$ BMDCs are in principle able to prime naïve T cells with the same strength as *WT* DCs but the frequency of DC-T cell interactions seems to be reduced.

DISCUSSION

In this work, we exploited the destabilization and degradation of the pentameric WAVE complex following genetic depletion of one of its subunits. The deletion of the hematopoietic isoform of *Nap1*, namely *Hem1*, in mice specifically disabled the WAVE-dependent Arp2/3 activation in blood cells and enabled the breeding of viable constitutive knockout mice. This allowed us to study the necessity and consequences of this pathway for the physiology of BMDCs. Using amoeboid migrating and chemotactic BMDCs we could reveal essential roles for WAVE-dependent actin branching for cell morphology and locomotion, particularly for lamellipodia formation, in cells that are independent of integrin-mediated force transduction during 3D migration (Lämmermann et al., 2008). Furthermore, we could derive lamellipodia function for random and directional migration. Strikingly, our findings indicate a different employment of WASp- and WAVE-dependent Arp2/3 activation during migration of immature and mature BMDCs.

WAVE-dependent Arp2/3 activation during leukocyte differentiation

Many studies have already tried to elucidate the function and requirement of actin branching for specific cellular processes. It has been demonstrated that genetic deletion of Arp2/3 complex is lethal for a variety of organisms including yeast, *Dictyostelium* and mice, leading to the conclusion that Arp2/3 complex is essential for development and viability in eukaryotes (Pollard and Cooper, 2009; Schwob and Martin, 1992; Yae et al., 2006; Zaki et al., 2007). However, two recent studies could show that this does not necessarily account for a group of mammalian cells in culture (Suraneni et al., 2012; Wu et al., 2012). Several alternative deletion or inhibition strategies focused on the upstream activating pathways including the direct Arp2/3 interactors WASp or WAVE complex. Using N-ethylnitrosourea (ENU) mutagenesis, *Park et al.* could attribute a neutrophilic and lymphopenic phenotype in mice with a single-nucleotide polymorphism (SNP) in the coding sequence of the *Hem1* gene. This point mutation introduced a stop codon in exon 13 leading to the premature termination of *Hem1* translation. Moreover, they identified Hem1 as a subunit of the WAVE complex that is almost exclusively expressed in the hematopoietic system. They could show that its absence results in the degradation of the WAVE complex in several blood cells consequently leading to a strong hematopoietic and immunological phenotype (Park et al., 2008). Employing a conditionally targeted *Hem1* knockout mouse, we could recapitulate WAVE complex degradation following *Hem1* deletion for BMDCs. Furthermore, we could show that WAVE ablation is dispensable for the differentiation and maturation of BMDCs *in vitro*, which is in line with an unaffected differentiation of neutrophils and macrophages as shown by their presence in the ENU mice. In contrast, lymphocyte numbers were drastically decreased in the peripheral blood of these mice, thus referring to an essential contribution of WAVE-dependent cytoskeletal rearrangements in lymphocyte development. Together, these

findings point to a different importance of this pathway for the myeloid and lymphoid lineage. Since distinct endogenous DCs can arise from the lymphoid lineage, it would be interesting to see if *Hem1* deletion differently affects the development of distinct DC subsets (Shortman and Naik, 2006).

The WAVE complex during leading edge formation

Several studies working on fibroblast migration could already show a pivotal role of WAVE-dependent lamellipodia-based migration downstream of Rac (Kobayashi, 1998; Suetsugu et al., 2003; Takenawa and Suetsugu, 2007). Deletion of *WAVE1* or *WAVE2* in fibroblasts even revealed a distinct role of these isoforms in lamellipodia formation (Suetsugu et al., 2003; Yamazaki et al., 2005). *WAVE2*$^{-/-}$ fibroblasts lost lamellipodia and formed multiple filopodial protrusions, demonstrating its essential function in the formation and extension of a broad lamellipodial actin network. Despite absent lamellipodia, fibroblast migration *per se* was still possible but velocity was decreased in response to chemotactic stimuli. Interestingly, reduced velocities were concomitant with diminished migration persistence (Suetsugu et al., 2003; Yan et al., 2003). In contrast, WAVE1 function contributed to lamellipodia stabilization and MMP secretion needed for ECM degradation in 3D migration (Suetsugu et al., 2003; Yamazaki et al., 2005). Consistently, two recent paper described a lamellipodia-independent migration in Arp2/3-depleted fibroblasts (Suraneni et al., 2012; Wu et al., 2012). They directly demonstrated the requirement of Arp2/3 for lamellipodia formation and loss of Arp2/3 resulted in similar morphological alterations as seen in the *WAVE2*$^{-/-}$ fibroblasts. Arp2/3 depleted cells formed multiple filopodia harbouring a sparse network of long and highly bundled actin filaments (Wu et al., 2012).

In our study we were able to recapitulate WAVE-depletion in an amoeboid migrating cell. Consistent with the morphological alterations of *WAVE2*$^{-/-}$ and Arp2/3-deficient fibroblasts, loss of WAVE complex in BMDCs resulted in the transformation of lamellipodial to filopodial membrane protrusions, independent of their maturation state. Moreover, using our approach we can report a solely WAVE-driven actin branching in lamellipodia formation of immature BMDCs. The observed transformation of a broad lamellipodium to a cone-shaped protrusion with a single pointed leading tip could be unambiguously attributed to the loss of actin branches at the leading edge. Whereas fibroblasts employ WAVE1 and WAVE2 at different steps during lamellipodia formation (Suetsugu et al., 2003; Yamazaki et al., 2005), BMDCs regulate WAVE complex-dependent actin branching exclusively via the WAVE2 isoform.

A direct consequence of cell shape changes was observed for the migration behaviour of WAVE depleted BMDCs. Whereas leading edge extension of mature BMDCs was mildly affected, immature BMDCs even gained migration velocity due to enhanced migration persistence. The latter might result from the unipolar and focal employment of the actin polymerization machinery. In contrast, the filopodial phenotype of *WAVE2*$^{-/-}$ fibroblasts drastically interfered with locomotion. Cells exhibited decreased migration velocities and directional persistence (Suraneni et al., 2012). The pronounced differences following WAVE

depletion for mesenchymal and amoeboid migrating cells might be explained by their distinct dependence on the interaction with the substrate. Mesenchymal migration strongly relies on the formation of focal adhesions and thus is a major determinant of cell shape. As reported by *Wu et al.*, Arp2/3-deficiency also interferes with the formation and dynamics of focal adhesions. In particular, the spatial organization and alignment of focal adhesions needed for efficient locomotion is severely disturbed (Wu et al., 2012). Consequently, the phenotypic observations are the direct and combined effect of an altered actin network and focal adhesion assembly. In contrast, focal adhesions are dispensable for amoeboid migrating BMDCs (Lämmermann et al., 2008) and hence do not determine their cell shape. Cell morphology and migration are in fact directly influenced by cytoskeletal dynamics and network geometry and only indirectly by environmental confinement.

Compared to fibroblast migration, a pronounced actin-driven protrusive force generation in the absence of WAVE complex is still possible in BMDCs. But which nucleator(s) actually promote actin polymerization instead still needs to be clarified. Additionally, it would be interesting to see if several actin nucleators including Arp2/3 are acting at the leading edge and WAVE complex ablation only uncovers the activity of the others, or if loss of WAVE complex rather enables the action of other nucleators. The latter idea is supported by a mechanism described in HeLa cells, which use WAVE complex and Arp2/3 to trap the formin mDia in a multimeric complex, thereby inhibiting filopodia formation (Beli et al., 2008). As the disappearance of WAVE was accompanied by the loss of VASP recruitment to the leading edge, our data even indicate a physical interplay of WAVE-dependent actin nucleation and elongation by VASP. A direct biochemical interaction of WAVE complex and VASP via Abi1 was also suggested before (Dittrich et al., 2010; Maruoka et al., 2011; Tani, 2003).The absence of WAVE thus not only reduces actin nucleation and branching, but also decreases actin polymerization rates during lamellipodia formation. Furthermore, VASP activity at the leading edge might not only be required for fast F-actin elongation but also for the competitive binding with actin capping proteins for free barbed ends. Although capping activity has been shown to essentially contribute to lamellipodia formation by assuring a locally high pool of G-actin and short actin filaments, both promoting actin nucleation and branching events (Disanza et al., 2005; Mejillano et al., 2004), an unbalanced high elongation termination rate (due to the lack of its competitor) together with the loss of an essential regulator of actin nucleation and branching could severely affect actin dynamics and protrusion stability. Although WASp might partially rescue Arp2/3 activity at the leading edge in mature BMDCs the lack of VASP still influences stability and dynamics of the lamellipodia and finally the overall migration speed.

The relationship between leading edge morphology and chemokine-guided directional migration

Consistent with the Arp2/3 deleted fibroblasts, our findings revealed severe alterations of cell morphology that did not interfere with the migration ability *per* se, but influenced velocity, migration persistence and the response to directional cues. Moreover, depending on the

maturation state of the BMDCs the loss of WAVE complex resulted in distinct cell morphologies accompanied with differing migration behaviours. Correlating the morphological appearance with the migration phenotypes of these two cell types, we can deduce general cellular requirements for a certain cell function.

Immature and mature *WT* BMDCs exhibit several dynamic and competing lamellipodial protrusions and are able to respond to a chemokine gradient with directional migration. Upon *Hem1* deletion protrusion morphology and migration behaviour were affected to a different extent in immature and mature BMDCs. Despite reduced velocity and pointed cell protrusions, mature *Hem1*$^{-/-}$ cells were able to follow chemokine gradients, whereas unipolar pointed immature cells failed to respond to a CCL3 gradient with directional migration, while migration speed is tremendously enhanced. Hence, our findings indicate that multiple protrusions but not protrusion morphology might be essential for gradient sensing. Like a broad lamellipodium, multiple filopodia-like protrusions could facilitate the simultaneous acquisition of several spatially different chemokine concentrations that can be subsequently integrated over the whole cell and enabling interpretation of the gradient. Only the protrusion with a sufficiently high chemokine signalling relative to the others would be extended or stabilized, resulting in migration towards the gradient source. Thus, multi-polarity would be a prerequisite for chemokine sensing.

Our observations made in more complex and denser substrate environments additionally support this idea. Concomitant with increasing collagen concentrations cells migrating with pointed protrusions displayed lower velocities than lamellipodial migrating cells. Thus, protrusion morphology rather influences its dynamics needed for efficient environmental explorations than gradient interpretation.

The defective chemotaxis of immature *Hem1*$^{-/-}$ BMDCs might also result from their unipolar cell shape and concomitant increased migration persistence rather than affecting gradient sensing *per se*. The sole and very focal actin polymerization leading to this "torpedo-shaped" cell might impede a rapid repolarization although chemokine sensing and signal integration across the cell perimeter is unaffected. In this scenario, cell mechanics would dominate biochemistry. Since the chemotaxis of immature *WT* DCs can only be traced for about 30 min in our assays we cannot exclude a gradual alignment and subsequent persistent migration of immature *Hem1*$^{-/-}$ BMDCs towards the chemokine source.

The importance of actin branching for chemotaxis is controversial. Two independent studies made on Arp2/3 depleted fibroblasts revealed opposite results (Suraneni et al., 2012; Wu et al., 2012). Although both studies performed their knockouts in mouse embryonic fibroblast (MEF) cell lines and observed the same morphological alterations, they report conflicting observations regarding chemotaxis of Arp2/3 depleted cells: *Wu et al.* reported impaired haptotaxis while fibroblast chemotaxis was normal, whereas *Suraneni et al.* describe defective directional migration in response to a chemotactic cue. As discussed above differs mesenchymal from amoeboid cell migration in the necessity of integrin-mediated focal adhesions. Since focal adhesions dynamics has been shown dependent on Arp2/3 activity, the absence of Arp2/3 and subsequently the absence of lamellipodia might differently affect

92

chemotaxis of mesenchymal and amoeboid cells. Using an amoeboid migrating cell system we can dissect and exclude influences of the interaction with the substrate and could reveal solely cell intrinsic requirements for directional migration.

Distinct employment of WAVE and WASp-dependent Arp2/3 activation during lamellipodia formation in immature and mature BMDCs

The different phenotypes of *Hem1* depleted immature and mature BMDCs suggested a different employment and roles of WASp- and WAVE-dependent Arp2/3 activation for lamellipodia formation. As evidenced by the complete absence of actin branches, Arp2/3 activation relies entirely on the WAVE complex and implies WASp absence from the leading edge of immature BMDCs. Concomitant with DC maturation we could find both, WASp recruited to the leading membrane independent of the presence of WAVE complex and partially restored actin branching at the leading edge of *Hem1* depleted cells. Thus immature BMDCs use a solely WAVE-driven actin branching to expand a lamellipodial protrusion, whereas mature BMDC use both NPFs (Fig. 32). This is rather surprising since WASp-mediated actin branching has been more attributed to the formation of other cellular substructures like podosomes/invadopodia, focal adhesions and filopodia (Takenawa and Suetsugu, 2007). Whereas several studies using different cell types could link an essential role of WAVE for lamellipodia formation (Suetsugu et al., 2003; Yamazaki et al., 2003; Yan et al., 2003), less has been reported for WASp on this process. Indeed, *in vitro* migration assays using *WASp-/-* BMDC did not show any obvious alterations in lamellipodia formation (observations of our lab, data not shown). Nevertheless, for carcinoma cells it could be shown that in fact N-WASp is not involved in the formation but the extension of lamellipodia (Lorenz et al., 2004).

Correlating the distinct phenotypes with the presence or absence of WASp-activity at the leading edge leads to further considerations: how is the WASp activity or localisation regulated in both cell types and what is the precise role of WASp at the leading edge? Is WASp-activity redundant or distinct from WAVE-dependent actin branching? In fact, *Dictyostelium* cells have been shown to employ the WAVE-homologue SCAR and WASp for distinct cell functions. *WT* cells exclusively control pseudopod formation via SCAR, whereas WASp drives the assembly of clathrin-coated pits. However in the absence of SCAR, WASp is able to respond to SCAR-upstream signals and to compensate its function (Veltman et al., 2012). Since we could detect WASp recruitment and actin branching at the leading front of *WT* and *Hem1* depleted mature BMDCs, one would assume a redundant function of WASp and WAVE. Considering that the "rescued" actin branching in *Hem1-/-* cells has not been observed for the full cell population argues for a partial or only transient compensation by WASp. This is further supported by the apparent interaction of WAVE and the actin elongator VASP. If WAVE mediates VASP recruitment to the leading membrane, stable lamellipodia formation could require the action of both. Thus, although WASp could compensate the branching function of WAVE, efficient elongation fails in the absence of VASP and results in a rather instable lamellipodium. Since these observation were made on a
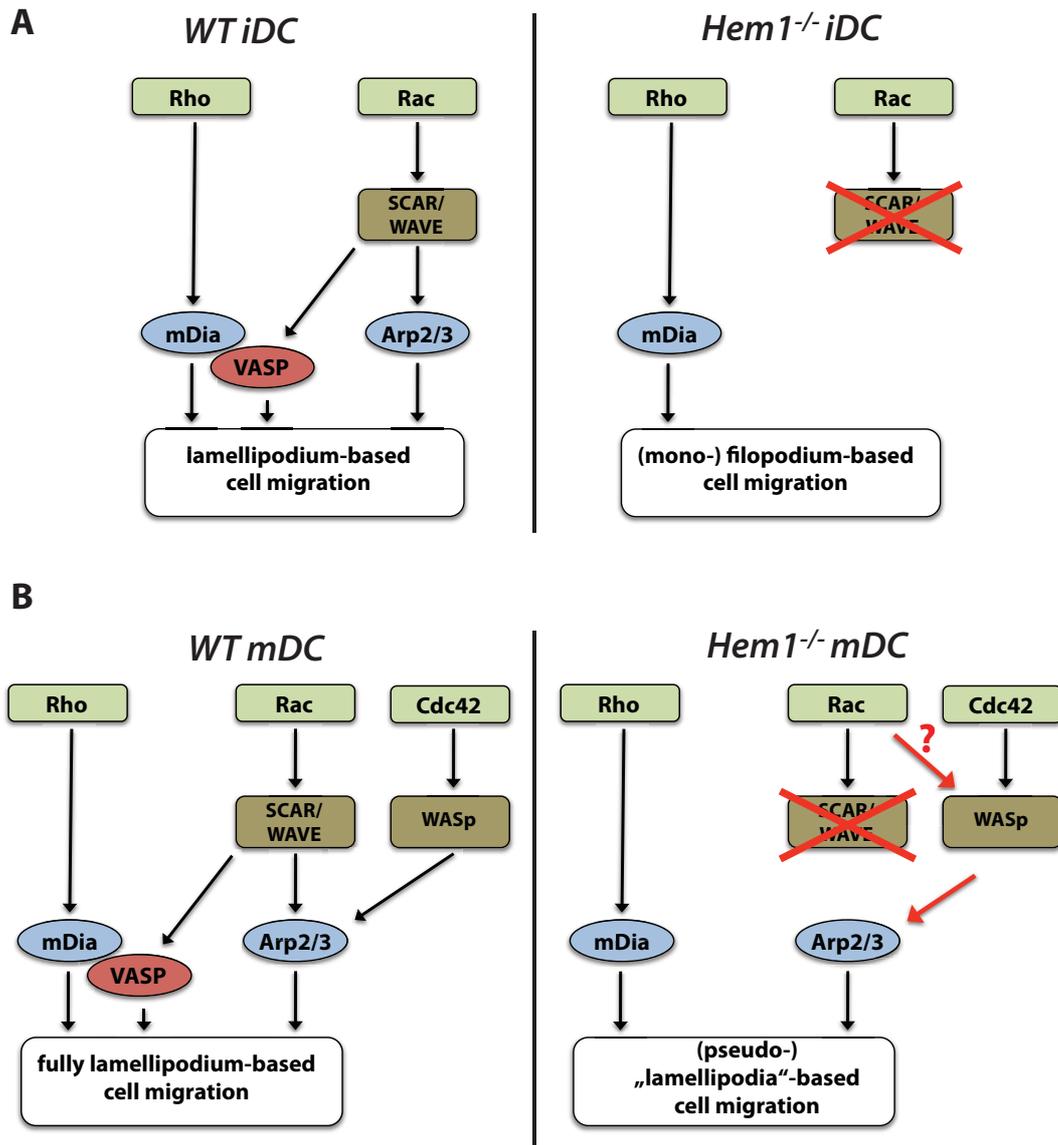
Figure 32. Hypothesized signalling pathways contributing to actin-driven protrusion formation in BMDCs. From our observation we derive the following scenarios: (A) In immature DCs solely WAVE-driven Arp2/3 branching in combination with linear-filament polymerization and elongation by formins lead to a lamellipodium-based migration mode. In the absence of WAVE complex, Arp2/3 is not activated at the leading edge resulting in a (mono-) filopodium-based locomotion. (B) In mature DCs Arp2/3 can be additionally activated at the leading edge by WASp, and hence both NPFs drive lamellipodium-based cell migration. In case of the loss of WAVE complex, WASp is able to (partially or transiently) compensate for Arp2/3 activation at the leading edge leading to the migration with a rather instable lamellipodium.

2D substrate and could not be directly seen in a 3D environment, in which the *Hem1* deleted cells show a clearly pointed morphology, further afford needs to be done to clarify if WASp activity at the leading edge is the consequence of the 2D substrate or an artefact generated by the experimental design.

Considering the different morphologies and 3D migration behaviour of immature and mature *Hem1*^{-/-} BMDCs, and an enabled WASp activity at the leading edge upon maturation, supports the idea of distinct roles of WAVE and WASp-dependent actin branching at the leading edge. WASp in mature BMDCs might not compensate for lamellipodia-shaped pseudopods but might render initiation of multiple protrusions. Thus, WASp-driven branches could provide the cyto-architecture for a fork-like protrusion network, whereas WAVE-dependent Arp2/3 activation drives the individual lamellipodial extension of each pseudopod (Fig.32, lower panel).

Recent studies also claimed a direct interaction between WASp and the WAVE complex component Ab1 (Innocenti et al., 2004; Singh et al., 2013; Wang et al., 2013). Although shown for different cell types and distinct cellular functions this interaction suggests a regulatory potential of the WAVE complex for WASp. If so, WAVE depletion could also negatively influence the membrane recruitment of WASp even though only partially since other recruitment mechanisms are still functional. Nevertheless, WASp activity could be decisively reduced and thus additionally destabilizing lamellipodia-like protrusion formation. Considering that both NPFs regulate membrane curvature via the interacting with BAR domain-containing proteins (Takenawa and Suetsugu, 2007), their loss could additionally contribute to the protrusion phenotype of *Hem1* deleted BMDCs.

Perspectives

Locomotion by cell shape dynamics

In a recent publication of Driscoll *et al.* (2012) a migration mechanism for chemotactic *Dictyostelium* cells was described that employs wave-like dynamic cell shape changes to promote locomotion (Driscoll et al., 2012). In non-adherent cells these myosin II-driven membrane waves propagate rearwards from the leading edge along both sides of the cell. When in contact with an adhesive substrate the waves, indicated by high curvature regions, stop moving relative to the substrate. By coupling the otherwise rearward moving membrane waves to the substrate, a traction force pushing the cell forward is generated. The authors relate these protrusive waves to the zig-zag-like motion and conclude a mechanism that allows for "cell swimming" in viscous fluids and navigation through complex 3D environments.

When observing the migration of *Hem1*^{-/-} BMDCs we noticed similar membrane dynamics as described for *Dictyostelium* cells. The unipolar "torpedo-shaped" cells displayed membrane waves originating from the very tip of the cell and travelling laterally to the posterior (as demonstrated by the stuck cell). During 3D migration some waves can entangle with the ECM and stop moving rearwards relative to the substrate. These observations suggested a migration mechanism analogous to *Dictyostelium*: when coupled to the substrate, retrograde membrane waves push the cell forward supporting actin polymerization-driven leading edge advance. As indicated by our experiments, integrin-mediated adhesion might not necessarily be important for the entanglement with the ECM but positively influences migration speed and persistence. Our data clearly do not prove but give some evidence that

such a mechanism might exist. In our further work we have to figure out the driving force of those waves and precisely correlate wave-ECM interactions with the cell's forward advance.

In 1939, W.H. Lewis postulated a "superficial plasmagel layer" with contractile properties that contributes to "form, locomotion and division" (Lewis, 1939). Ignoring his idea for almost half a century, subsequent work focusing on the cell cortex suggested that cortical contraction leads to intracellular flows that promote these cellular properties and events (Bray and White, 1988). These conclusions were made from descriptive rather simple and low resolved brightfield microscopy observations and a correlation of these intracellular flows to cell crawling has not been made until today. Following their idea of contraction-driven cortical flows, using immature $Hem1^{-/-}$ as a model cell system we might be able to prove the existence of those intracellular flows and link them with wave-like dynamic cell shape changes. Then, another 25 years later, one could finally prove Lewis' postulate by correlating cortical flows with locomotion.

WAVE-dependent Arp2/3 activation for Ag-presentation and T cell activation

Apart from directed cell migration, other physiological functions of DCs include antigen uptake, processing and presentation, as well as the activation of naïve T cells. All these processes have been demonstrated to require a dynamic actin cytoskeleton (Vicente-Manzanares and Sánchez-Madrid, 2004). Many studies revealed the importance of the upstream regulatory elements driving actin polymerization, particularly the Rho-GTPases or their direct regulators Rho-GEFs/ Rho-GAPs. In dendritic cells essentials roles for the Rho-mDia-dependent actin nucleation as well as for WASp-driven actin branching on T cell priming have been made ((Bouma et al., 2011; 2007; Pulecio et al., 2008; Tanizaki et al., 2010)). Using $Hem1$ deleted BMDCs we can elucidate specific steps during immunological synapse formation and T cell activation that require WAVE-dependent actin branching. Our preliminary *in vitro* data auspiciously indicate a defective T cell stimulation potential that calls for further detailed investigations.

Concluding remarks

In this thesis we elucidated the importance of branched actin networks for the physiology, particularly for the migration of BMDCs. Using the genetic deletion of the hematopoietic WAVE complex subunit $Hem1$ to generate BMDCs lacking the whole WAVE complex we revealed two distinct morphological phenotypes that depend on the maturation status of the cell. This clearly indicated a different employment and importance of this pathway for these two cell types but more importantly it opened up the possibility to derive general architectural requirements of a cell for a certain cellular function. Fig. 33 depicts the cell and protrusion morphologies depending on their genotype and maturation status and their consequence on the migration behaviour. As already discussed above, a qualitative comparison of the protrusion morphologies and their concomitant consequence for the migration let us conclude that although having an unaffected signalling apparatus a cell can only obtain a function if certain cyto-architectural conditions are fulfilled. In our case, a

gradient can only be sensed with an intact signal transduction in addition to multiple protrusions. Further work is ongoing to ultimately prove this statement.

A major finding of this study was the impressive phenotypic outcome of immature BMDCs following *Hem1* deletion. But instead of considering these cells as the pure consequence of WAVE ablation, the torpedo-shaped cells can serve as a discrete cell system consisting of a minimal migration apparatus: linear protrusive actin polymerization, actomyosin contractility and integrins. Interfering with the latter has been shown to result in residual migration and might even be dispensable. Thus, using this system one might deduce cellular mechanisms that contribute to migration and have yet not been discovered since they are covered or repressed in a more complex actin cytoskeleton. Furthermore, this minimal system and its implications on the migration behaviour evidence and emphasize the necessity of additional components that modulate the actin cytoskeleton required for a physiological relevant cell migration and function.

		gradient	
	locomotion	sensing	polarity
WT *iDC/mDC*	++	++	++
Hem1⁻ᐟ⁻ *mDC*	+	++	++
Hem1⁻ᐟ⁻ *iDC*	+++	-	+++

Figure 33. Filament geometry determines cell and protrusion morphology. Taken together we could show that the loss of actin branching severely alters cell shape, which in turn affects cell polarity, migratory behaviour and gradient sensing. Multiple competing lamellipodial protrusions seem to be required for efficient 3D locomotion (especially in complex environments) and a pointed morphology doesn't affect the capability to respond to chemotactic gradients with directional migration. But if protrusion number is additionally reduced to one, the resulting hyperpolarized cell exhibits a highly persistent and accelerated migration but fails to sense chemotactic gradients. Thus, protrusion number but not their individual morphology is critical for chemotaxis.

MATERIAL AND METHODS

Material

Chemicals

All chemicals used are mentioned individually in the methodical description.

Mice

All animals used in this study were bred and maintained in a conventional animal facility at the Institute of Science and Technology Austria (IST Austria, Preclinical Facility) according to local regulations. Mice were sacrificed between 4 to 12 weeks of age for use in experiments. *Wildtype* (C57BL/6JCrl), *CD11c-Cre^tg* (B6.Cg-Tg(Itgax-cre)1-1Reiz/J)(Caton et al., 2007), *mT/mG^tg* (B6.129(Cg)-Gt(ROSA)26Sortm4(ACTB-tdTomato,-EGFP)Luo/J)(Muzumdar et al., 2007) and *OT-II^tg* (B6.Cg-Tg(TcraTcrb)425Cbn/J)(Barnden et al., 1998) mice were originally purchased from Charles Rivers Laboratories International, Inc. and further bred in the IST Austria animal facility. *Hem1^-/-*, *Hem1^fl/fl* (both unpulished) and *WASp^-/-* animals were provided by Prof. Dr. Theresia Stradal (University of Münster/ Germany). *Lifeact-GFP^tg* mice were generated in collaboration with Prof. Dr. Roland Wedlich-Söldner at the Max-Planck-Institute for Biochemistry (Riedl et al., 2008). Except for crossings with *mT/mG^tg* animals (129SV background), all mice were kept with a C57BL/6 background.

Plasmids

The following table includes all plasmids used for transfection into bone marrow-derived DCs.

Plasmid	References
Lifeact-GFP	(Riedl et al., 2008)
VASP-GFP	Theresia Stradal
ArpC5 (p16)-GFP	Theresia Stradal
WASP-GFP	Michael Way
Hem1-GFP	(Weiner et al., 2006)
WAVE1	Theresia Stradal
WAVE3	Theresia Stradal

Antibodies

The following antibodies were used for immunodetection by flow cytometry, Immunohistochemistry or Western Blotting.

Molecule	Isotype	Labeling	Dilution	Clone	Source
CD11c	ar. hamster IgG	APC	1:300 (FACS)	N418	eBioscience
MHC II (I-A/I-E)	rat IgG2b, κ	eFlour450	1:800 (FACS)	M5/114.15.2	eBioscience
CD4	rat IgG2b, κ	biotin	1:300 (FACS)	GK1.5	eBioscience
CD40	rat IgG2a, κ	biotin	1:100 (FACS)	1C10	eBioscience
CD16/32	rat IgG2a, λ	-	1:100 (FACS)	93	eBioscience
CD80	ar. hamster IgG	biotin	1:1200 (FACS)	10-1071	eBioscience
CD86	rat IgG2a, κ	biotin	1:1200 (FACS)	GL-1	eBioscience
CCR7	rat IgG2a, κ	PE	1:300 (FACS)	4B12	eBioscience
Isotype Control	ar. hamster IgG	APC	1:300 (FACS)	eBio299Arm	eBioscience
Isotype Control	rat IgG2b, κ	eFlour450	1:800 (FACS)	eB149/10H5	eBioscience
Isotype Control	rat IgG2a, κ	PE	1:300 (FACS)	eBR2a	eBioscience
Streptavidin	-	PE	1:400 (FACS)	-	eBioscience
WAVE1 (L-19)	goat IgG	-	1:200 (WB)	polyclonal	Santa Cruz
WAVE2	mouse IgG	-	1:10 (WB)	2236.1	T. Stradal
WAVE3	rabbit IgG	-	1:1000 (WB)	polyclonal	Cell Signal.
GAPDH	mouse IgG1	HRP	1:3000 (WB)	GA1R	Abcam
LYVE1	rat IgG2a	-	1:300 (IHC)	223322	R&D Sytems
α-mouse	goat IgG (H+L)	HRP	1:5000 (WB)	polyclonal	Bio Rad
α-rabbit	goat IgG (H+L)	HRP	1:5000 (WB)	polyclonal	Bio Rad
α-goat	donkey IgG	HRP	1:3000 (WB)	polyclonal	Santa Cruz
α-rat	donkey IgG, F(ab')$_2$	Alexa Flour 488	1:400 (IHC)	polyclonal	Jackson

Microscopy and FACS

The following microscopes and FACS devices were used and provided by the Bioimaging Facility of the IST Austria: Upright Zeiss LSM 700 confocal microscope, Upright and inverted Leica SP5 confocal microscope, Upright multiphoton LaVision microscope, Visitron

TIRF/FRAP microscope, Becton Dickinson Biosciences cell sorter FACS Aria III and cell analyser FACS CantoII.

Electron microscopic pictures were acquired by a FEI Tecnai F30 (Polara) microscope in collaboration with the group of Prof. Victor Small at the Institute of Molecular Biotechnology Austria (IMBA) Vienna.

Methods

Cell culture

All cells were grown and maintained in a humidified incubator at 37°C and 5% CO_2. If not mentioned additionally, hematopoietic cells were cultured in R10 medium.

R10 medium: RPMI (Gibco) supplemented with 10% fetal calf serum (FCS; Gibco), 5% penicillin/streptomycin (Gibco), 5 % glutamine (Gibco) and 50μM β-mercaptoethanol (β-Me-EtOH, Gibco)

GM-CSF production

Bone marrow differentiation into DCs or macrophages is dependent on the growth factor granulocyte-macrophage colony-stimulating factor (GM-CSF; (Lutz et al., 1999)). Growth factor was obtained via the cultivation of a GM-CSF secreting hybridoma cell line (provided by Prof. Dr. Brigitta Stockinger, National Institute for Medical Research, London, UK). The GM-CSF producing hybridoma cells were cultivated in R10 medium in cell culture flasks (BD Falcon). Cells were kept at 90 to 100% confluency for two days in the same medium. The cell supernatant was collected, centrifuged to remove remaining cells and filtered (Corning vacuum filter/storage bottle system, 0.45 μm pore size) before addition to bone marrow cells. After two rounds of supernatant collection the cells were trypsinised, split and transferred to new flasks. Growth factor containing cell supernatants were stored at 4°C.

Cell passaging

For the passaging of the adherently growing GM-CSF hybridoma cell line, cells needed to be detached from cell culture flasks (Greiner) by trypsinisation. Adherent cells were washed with phosphate buffered saline (PBS, Gibco) prior to incubation with 2 ml Trypsin-ethylenediaminetetraacetic acid (1x Trypsin-EDTA) solution (Gibco;) for 2-4 min at room temperature (RT). Adding 10 ml R10 medium stopped the enzymatic activity of trypsin. The cells were centrifuged and resuspended in fresh culture medium. Cells were seeded at the desired density in a new culture flask.

Generation of bone marrow-derived DCs (BMDCs)

DCs were generated from flushed bone marrow as previously described by (Lutz et al., 1999)

with modifications mentioned in (Weber and Sixt). Mice were sacrificed by cervical dislocation and the femurs removed. After brief disinfection with 70% ethanol, the bones were opened with sterile scissors at the distal end. Bone marrow was obtained by centrifugation of the bones using a self-assembled centrifugation tube: a rubber ring was placed half way inside a 1.5 ml microfuge tube. A 1 ml pipette tip was inserted into the ring and cut at the top end to a suitable size so that the lid of the tube closed. Additionally, 250 µl of R10 medium were added to the microfuge tube. The femur and tibia of one mouse were placed vertically with the opened side down into the opening of the pipette tip. Bones were centrifuged in a benchtop centrifuge at 1900xg for 4 min in order to collect the bone marrow. The rubber ring and the pipette tip were subsequently removed and the pelleted bone marrow was resuspended in fresh R10 medium ensuring the cells were separated. Cells were counted using the CASY Cell Counter (Roche). Subsequently, cells were adjusted to a final concentration of $2.5x10^5$ cells/ml in R10 medium supplemented with 10% GM-CSF. Bone marrow of *Hem1^{-l-}* mice was plated at $1,25x10^5$ cells/ml; a volume 10 ml cell suspension was transferred to one 10 cm petri dish (Greiner). On day 3 of culture 10 ml of R10 medium containing 20% GM-CSF was added. On day 6 and 8 of culture 10 ml medium were removed by aspiration and replaced with 10 ml R10 medium supplemented with 20% GM-CSF. DCs were used for experiments at day 7-8 as immature, or at day 9 to 10 as mature BMDCs (see next paragraph), respectively. If not used directly, cells were cryo-preserved at day 8 to 9 of culture.

BMDC maturation

On day 8 to 9 of culture immature BMDCs were matured overnight. DCs of on 1-2 petri dishes (depending on cell density) were pooled and pelleted, resuspended in 12 ml R10 medium supplemented with 10% GM-CSF and split onto two 5 cm cell culture dish (Falcon) containing 6 ml cell suspension. DCs were matured by stimulation with 200 ng/ml lipopolysaccharide (LPS; Sigma-Aldrich; *E.coli*; 0127:B8). Non-adherent, mature DCs were used for experiments after at least 12 hours.

Cryopreservation and thawing of DCs

DCs of two petri dishes (approx. $5x10^6$ cells) were pelleted and resuspended in 1 ml of precooled freezing medium (4°C) and transferred to cryo vials (Corning). The cells were stored at -80°C or for long-term storage (> 3 months) transferred into liquid nitrogen.

For recovery the cryo vials were placed in a water-bath at 37°C. The thawed cell suspension was washed once with 10 ml PBS, pelleted and resuspended in 24 ml R10 medium. Cell suspension was split over four 5 cm cell culture dishes (Falcon) and overnight maturation was induced by the addition of 200 ng/ml LPS.

Freezing medium: FCS (Gibco) supplemented with 10% DMSO (Sigma-Aldrich)

BMDC plasmid transfection

For DC transfection with GFP-construct plasmids the *Mouse T Cell Nucleofector® Kit* (Lonza) was used. An amount of $4\text{-}5\times10^6$ immature DCs were pelleted (300 g, 5min) and washed once with 1xPBS. After pelleting, the cells were resuspended in 100 µl room temperate *Mouse T Cell Nucleofector solution* supplemented with the provided additive according to the manufacturer's instructions. Subsequently, 4-5 µg plasmid DNA was added and thoroughly mixed. After incubation for 10-15 minutes at RT, the cell suspension was transferred to the provided electroporation cuvette (Lonza) avoiding air bubbles. Transfection was performed using the *program X-001* of the *Amaxa Nucleofector*. Immediately after transfection the DC suspension was transferred into a 5 cm culture dish (Falcon) containing 6 ml pre-warmed (37°C) R10 medium supplemented with 10% GM-CSF. Four hours post infection, maturation was induced with 200 ng/ml LPS (Sigma-Aldrich; *E. coli* 0127:B8).

For the enrichment of productively transfected cells, GFP-expressing (GFP positive) cells were identified and sorted using the FACS AriaIII (Becton Dickinson; GFP: excitation 488 nm; emission 575 nm).

HEK transfection for protein overexpression

HEK293 cells were grown in D10 medium. HEK cells were used for protein overexpression by transfection of protein-GFP plasmid constructs. The day before transfection, HEK cells were seeded in a 6-well cell culture plate (Falcon) ensuring that the cells would be at 30-40 % confluency the following day. For transfection 100µl OptiMEM (Gibco) was mixed with 5 µl Lipofectamine® 2000 (Invitrogen) and incubated for 5 minutes at RT. Meanwhile another 100 µl OptiMEM was supplemented with 1 µg plasmid-DNA. Both solution were then combined and incubated for a further 25 minutes at RT. Finally, 200 µl of DNA-Lipofectamine-OptiMEM mixture was added to the HEK cells with 2 ml DMEM. Transfection efficiency was checked 24-36 hours post transfection by GFP-expression using a standard lab fluorescence microscope. Cells were washed with 1x PBS and trypsinised for 5 minutes following harvesting and pelleting (300g, 5 min). The cell pellet was washed again with 1x PBS, before cells were lysed in 150 µl RIPA buffer (NEB). Cell lysates were prepared and stored as described (*see:* Biochemical methods).

D10 medium: *DMEM (Gibco) supplemented with 10% fetal calf serum (FCS; Gibco), 5% penicillin/streptomycin (Gibco) and 5 % glutamine (Gibco)*

In vitro excision of loxP-flanked genes in BMDCs

As a constitutive deletion of *Hem1* and *WASP* double knockout appeared to be embryonically lethal, we aimed to generate *Hem1$^{-/-}$* x *WASP$^{-/-}$* BMDCs by *in vitro* excision of *Hem1* in *WASP* deficient BMDCs. For this purpose *Hem1^{floxflox}* x *WASP$^{-/-}$* mice were crossbred and sacrificed to isolate bone marrow for BMDC generation. BMDC culture was started according to the BMDC generation protocol mentioned above until day 3 of differentiation. On day 3 cells were harvested and washed 3x with 1xPBS (Centrifugation in between for 5min/300g). Cells

were resuspended to a final concentration of $2x10^6$ cells/ml in pre-warmed HyClone medium (Thermo Scientific) and transferred to fresh 10 cm petri dishes (max. 25 ml per petri dish). After one hour of starvation at 37°C/ 5% CO_2 4 µM Tat-NLS-Cre ((Peitz et al., 2002); recombinant protein was purchased from the core facility of the Max-Planck-Institute for Biochemistry, Martinsried) and 250 µM Chloroquin (Sigma-Aldrich) was applied for another hour at 37°C/ 5% CO_2. Afterwards cells were harvested and plated at 2.5 x 10^6 cells per 10cm petri dish in 20 ml of R10 medium supplemented with 20% GM-CSF supernatant. Differentiation was continued and maturation was executed as described previously.

Biochemical methods

Preparation of whole cell lysates

Immature or mature BMDCs were harvested and washed once with 1xPBS. An amount of $1x10^6$ cells were pelleted and resuspended in 100 µl cooled 1x lysis buffer (NEB). Cell lysates were incubated for 10 min on ice prior to lysate clearance by centrifugation, 10 min at 4°C at full speed (< 13000rpm). The supernatant was transferred into a fresh low-protein-binding reagent tube (1.5 ml; Biozym) and kept on ice until further proceeding with SDS-PAGE and Western blotting. Protein concentrations were determined using the BCA (bicinchoninic acid) Protein Assay Kit (Pierce). If not directly used for further assays, lysates were snap frozen in liquid nitrogen and stored at -80°C.

SDS-PAGE

For protein separation by molecular mass and subsequent identification by western blotting the Novex® NuPAGE® SDS-PAGE (sodium dodecyl sulfate polyacrylamide gel electrophoresis) Gel System (Invitrogen) was used. All steps were performed according to the manufacturer's protocol. Volumes corresponding to 15-30 µg proteins from whole cell lysates were mixed with 2x sample loading buffer in a maximum volume of 15 µl and proteins were subsequently denatured for 10 minutes at 70°C. After brief centrifugation, the lysates were loaded on pre-cast 4-12% NuPAGE® Bis-Tris Gels (Invitrogen) and gels were run for 50-60 minutes at 200V in 1x MOPS buffer (NuPAGE® 20x MOPS SDS running buffer; Invitrogen).

2x sample loading buffer: *50 µl 4x NuPAGE® LDS sample buffer (Invitrogen) was mixed with 10 µl 10x reducing reagent (Invitrogen) and 40 µl millipore water.*

Western blotting

Western blotting was used to detect and quantify specific proteins by means of antibodies. The proteins were separated by SDS-PAGE (described above) and subsequently electrophoretically transferred to a PVDF membrane (iBlot® Transfer Stack, PVDF; Invitrogen). The iBlot® - Western Blotting System (Invitrogen) was used. The transfer was strictly performed according to the manufacturer's protocol.

For the immunodetection of the protein the membranes were blocked with blocking buffer for 1 hour at RT. The respective primary antibodies were diluted in blocking buffer

and applied for overnight incubation at 4°C under. The next day the membrane was washed three times for 15 min with 1x TBS-T and incubated with horseradish peroxidase (HRP)-conjugated secondary antibody diluted in blocking buffer for 1.5 hours at RT. The membrane was washed as previously described, followed by antibody detection using *Clarity™ Western ECL Substrate* (Bio Rad). For chemiluminescence detection the PVDF membrane was incubated for 5 minutes with a mixture of 500 µl Clarity western peroxide reagent and 500 µl Clarity western luminol/enhancer reagent. All incubation steps were carried out under constant agitation. The chemiluminescent signal was detected with the Molecular Imager® VersaDoc™ MP Imaging System (Bio Rad) of the life science facility of IST Austria.

10x Tris buffered saline (10x TBS): *200 mM Tris (Sigma-Aldrich), 1.4 M NaCl (Merck), pH 7.5*

1x TBS-T: *1xTBS + 0.1% Tween20 (Sigma-Aldrich)*

WB blocking buffer: *1x TBS-T containing 5% non-fat milk (Sigma-Aldrich)*

Primary antibody	Dilution	Secondary antibody	Dilution
α-WAVE1	1:200	α-goat-HRP	1:3000
α-WAVE2	1: 20	α-mouse-HRP	1:5000
α-WAVE3	1:1000	α-rabbit-HRP	1:3000

Extraction and fixation of the actin cytoskeleton (for EM analysis)
Cells were differentiated and matured as described. EM-grids (1% Formvar-coated 200 mesh hexagonal Au grids, Agar Scientific) with additional carbon, glow discharged!) were coated for 1 hour with 0.01 L-Polylysine (150-300 kDa, Sigma-Aldrich). Cells were seeded on the grids at a sufficient density and incubated for <2 hours to allow for cell spreading and polarization. Afterwards, cells were simultaneously extracted and fixed with 0.5% Triton X-100 (Fluka) and 0.25% glutaraldehyde (Agar Scientific) in 1x CB. After an initial fixation of 2 min, post fixation was carried out for 15 min in cytoskeleton buffer containing 2% glutaraldehyde and 1 µg/ml phalloidin (Life Technologies) to stabilize the actin filaments. The grids were then stored in cytoskeleton buffer containing 2% glutaraldehyde with 10 µg/ml phalloidin at 4 °C, before processing for electron microscopy. Negative staining was performed in mixtures of 4–6% sodium silicotungstate (SST) (pH 7), supplemented with 10 µg/ml phalloidin and 10 nm BSA (bovine serum albumin)- saturated gold colloid diluted 1:10 from a gold stock (Koestler et al., 2008). Samples were respectively analysed on an 80kV transmission electron microscope (Morgagni, FEI) and FEI Tecnai F30 Helium (Polara) microscope, operated at 300 kV.

10x Cytoskeleton buffer (CB): 10 mM MES, 150 mM NaCl, 5 mM EGTA, 5 mM glucose, and 5 mM MgCl2, pH 6.1.

Immunological methods

Flow Cytometry/ Fluorescence-**activated cell sorting (FACS)**

Fluorescence-labelled antibodies were used for the labelling cell surface proteins and for quantification by flow cytometry. Surface staining was performed according to standard procedures at a cell density of 1-2 x 10^6 per 50 µl and volumes were scaled up accordingly. In brief, cells were washed once with FACS buffer, pelleted (300 g, 5 min) and resuspended in FACS-buffer supplemented with the appropriate amount of primary antibodies. Cell suspensions were incubated in the dark for 15 min at 4°C to allow for antibody binding. After washing with FACS-buffer (5x staining volume), cells were directly stained with labelled primary antibodies, resuspended in an appropriate volume of FACS buffer and used for FACS analysis. Biotinylated primary antibodies were subsequently stained using a fluorescence-labelled streptavidin (15 min, 4°C) prior to FACS analysis.

Cell surface staining of CCR7 on DCs was performed at 37°C for 30 min in the dark followed by immediate cool down on ice to prevent receptor internalization. Samples were constantly kept at 4°C during washing steps and waiting times until data acquisition.

Flow-cytometric analysis was performed on FACS Canto II (Becton Dickinson) or FACS Aria III (Becton Dickinson) using FACS DIVA software (Becton Dickinson) for acquisition and FlowJo (Treestar) for analysis.

FACS buffer: 1x PBS (GIBCO), 2 mM EDTA (Sigma-Aldrich), 1% BSA (Sigma Aldrich)

In vitro T cell proliferation assay

To test the T cell priming efficiency of *WT* and *Hem1$^{-/-}$* BMDCs, an *in vitro* assay of OT-II T cell activation was performed. CD4$^+$ T cells of OTII transgenic mice (B6.Cg-Tg(TcraTcrb)425Cbn/J, The Jackson Laboratory) were isolated from LNs and spleen. Organs were dissected and disrupted in FACS buffer using 2 moistened microscope slides. The cell suspension was subsequently filtered using a cell strainer (BD Falcon, 70µm Nylon) before cells were pelleted and resuspended in MACS buffer. Subsequently CD4$^+$ T cells were purified by positive selection using MACS (CD4 (L3T4) MicroBeads, Miltenyi Biotec) according to the manufacturer's protocol. Following isolation, T cells were labelled with the fluorescent dye 5,6-carboxyfluorescein diacetate succinimidyl ester (CFSE). Labelling allows monitoring of cells that proliferate in response to Ag (OVA peptide). These cells show a reduction in CFSE fluorescence, which is directly measured by FACS. For CFSE labelling, T cells (10x10^{6}cells/ml) were resuspended in pre-warmed (37°C) CFSE labelling buffer (1x10^7 cells/ml) and pre-incubated for 5 minutes at 37°C (water bath). CFSE staining solution (eBioscience) was then added rapidly (final CFSE conc. = 1 µM) to the cell suspension and mixed thoroughly. Staining was performed for 10 minutes at 37°C while mixing was repeated every 2 minutes. To stop the labelling reaction pre-warmed (37°C) R10 medium was added and cells were subsequently washed twice with 1xPBS. Finally, T cells, OVA peptide (synthesized by the core facility of the MPI of Biochemistry, Munich) and mature BMDCs (BMDCs were differentiated and matured as described before) were mixed and the assay

started: 5×10^4 T cells were mixed with 5×10^3 BMDCs in the presence of varying concentrations of OVA peptide (0.01 – 1.0 µg/ml final) to a final volume of 200 µl R10 per well of 96-well plate (round bottom, Falcon). Proliferation occurred for 72h at 37°C/ 5% CO_2 in a standard incubator. Before proliferation was analysed by FACS, cells were stained for CD4 (αCD4-eF450, eBioscience) and 7-amino-actinomycin D (7-AAD viability staining solution, eBioscience).
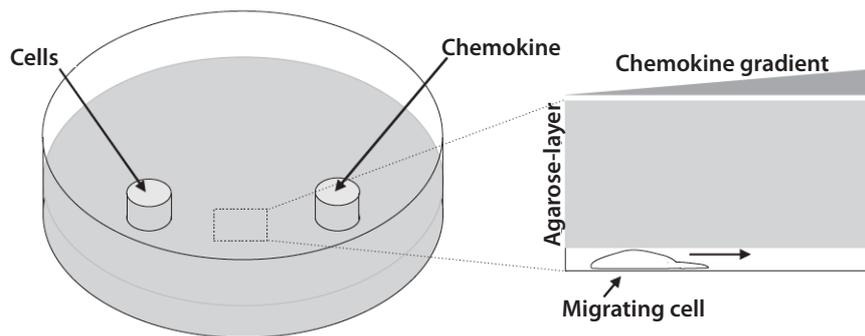
Figure 34. Experimental setup of the under agarose assay. A cell solution is injected under the agarose layer. Cells migrate in the confined environment between the glass surface and the agarose matrix.

Cell migration assays

Under agarose assay

The "under agarose assay" (UAA) was used for the analysis of the actin cytoskeleton dynamics and the localization pattern of different GFP-tagged proteins during DC migration, imaged using total internal reflexion fluorescence (TIRF) microscopy. In the UAA BMDCs were injected between the cover slip and an agarose/medium layer, directed migration was induced by an adjacent chemokine reservoir (Fig. 34).

For the UAA, a 5% agarose solution was made by dissolving 1 g agarose (UltraPure™, Invitrogen) in 5 ml ddH₂O, heating it until the agarose was completely solubilized. The agarose solution was mixed with prewarmed solution (48,5°C) of 5 ml 2xHBSS and 10 ml R20 medium. A volume of 400 µl from the final solution was filled into a custom-made round glass bottom dish (diameter 2 cm). The agarose/medium was equilibrated for 20-25 minutes at 37°C 5% CO_2 in a humid environment. Afterwards, a chemokine reservoir was created by stamping a hole into the agarose layer, which was subsequently filled with 2.5 µg/ml CCL19. Within a distance of approximately 5 mm $2-3 \times 10^4$ DCs, in a volume of 0.7 µl were injected between the glass coverslip and the agarose layer.

For all TIRF-UAAs custom-made glass bottom dishes were used. The glass slides were untreated or coated with polyethylene glycol (PEG). For PEG coating the glass bottom dishes

were plasma-treated for 1 min in a plasma cleaner (Harrick) and afterwards covered with 100 µl PLL-PEG coating solution at 4°C over night. Before usage in the assay, the dishes were rinsed with 1xPBS to remove residual unbound PLL-PEG.

HBSS (2x): 0,975 g/l Hanks' balanced salts (Sigma-Aldrich), 7 mM Na2CO3 (Merck), pH 7.2

R20 medium: RPMI (Gibco) with 20% FCS (Gibco), 5% penicillin/streptomycin (PAA), 5% glutamine (PAA)

PLL-PEG coating solution: 0.2 mg/ml poly(L-lysine)-graft-poly(ethylene glycol) (PLL-g-PEG; SuSoS) in 10 mM HEPES pH 7.3

3D bovine collagen assay

In order to quantify the migration velocities and/or to determine the chemotactic potential, DCs were incorporated into a 3D collagen matrix *in vitro* and migration behaviour was observed. For chemotaxis assays, a CCL3 (immature DCs) or a CCL19 (mature DCs) chemokine gradient was applied. This assays was performed as previously described in (Lämmermann et al., 2008).

For one standard collagen gel, 150 µl PureCol® was carefully mixed with 20 µl MEM (10x) and 10 µl $NaHCO_3$-solution avoiding bubbles. A 2:1 ratio, 150 µl of the collagen solution was mixed with 75 µl DC suspension resulting in a final gel concentration of 1.7 mg/ml and a cell concentration of 1×10^6 cells/ml gel. 125 µl of the collagen-cell mixture was casted into a round custom-made migration chamber (diameter 12 mm, thickness 2 mm). For the assembly of the collagen fibers and buffer equilibration, the gels were incubated at 37°C 5% CO_2 for 45 minutes. Afterwards, the gels were overlaid with 40 µl of CCL19 (0.625 µg/ml final conc. Diluted in R10 medium, R&D Systems) or CCL3 (0.625 µg/ml final conc. Diluted in R10 medium, PeproTech). For inhibition studies, gels were supplemented with 30 µM blebbistatin (Sigma-Aldrich), 100 nM or 500 nM latrunculin A (Tocris Bioscience) or 5 mM EDTA, pH 8.0 (Sigma, Aldrich) before casting the gels. Inhibitors were present in the same end-concentrations as in the chemokine dilutions.

DC migration was observed via time-lapse video microscopy. Manual cell tracking was carried out using the software ImageJ with the 'Manual Tracking Plugin' and trakcs were plotted using the "Chemotaxis Tool" (both http://rsbweb.nih.gov/ij/).

Collagen solution: PureCol® (stock: 3,1 mg/ml, bovine Collagen I, Advanced Biometrix) in 1× minimum essential medium eagle (MEM 10x, Sigma-Aldrich) and 0.4% sodium ($NaHCO_3$-solution 7.5%, Sigma-Aldrich)

DC suspension: mature DCs adjusted to $3x10^6$ cells/ml in R10 medium

3D rat tail collagen assay

To validate the migration behaviour and velocities in more complex environments, we performed the abovementioned 3D collagen gel assay using rat tail collagen type I (3.74 mg/ml, Becton Dickinson) with a modified protocol. Bovine collagen is obtained by acidic pepsin treatment that reduces the number of telopeptides needed for collagen crosslinking during collagen fibril assembly. In contrast, rat tail collagen is still telopeptide intact, thus forming thinner fibrils that generate a collagen network with narrower pore sizes (Wolf et al., 2013). Fibrillar collagen matrices were reconstituted *in vitro* by raising the pH to 7.4 using 0.345 N NaOH and buffering by 20 μM HEPES together with MEM. Collagen matrices with different final collagen concentrations were prepared by dilution of the rat tail collagen stock solution with 0.01 N HCl. The preparation of collagen stock solutions for different matrices summarized in the following table:

Rat tail collagen stock (3,74 mg/ml) μl	HCl 0.01 N μl	Final collagen concentration in matrix (mg/ml)
296	354	1.1
470	180	1.7
643	7	2.3
Final volume: 650 μl		

For 306 μl gel one of these collagen stock solutions (dependent on desired final collagen concentration in the gel) was mixed with 40 μl MEM (10x), 35 μl NaOH (0.345N), 10 μl HEPES (1M) and 100 μl DC suspension (LPS-matured DCs, 2.5×10^6 cells/ml in R10). The collagen-DC mixture was cast into a round custom-made migration chamber (diameter 12 mm, thickness 2 mm) and polymerized at 37°C 5% CO_2 for 15-20 minutes. Afterwards, the gels were overlaid with 40 μl of CCL19 (0.625 μg/ml final conc. Diluted in R10 medium, R&D Systems).

DC migration was observed via time-lapse video microscopy. Manual cell tracking was carried out using the software ImageJ with the 'Manual Tracking Plugin' and tracks were plotted using the "Chemotaxis Tool" (both http://rsbweb.nih.gov/ij/).

The fibrillar collagen matrix architecture was detected by confocal reflection microscopy using the Leica SP5 inverted microscope (objective: HC PL APO 20/0.7 CS, argon ion laser 488nm, detection = 480-500nm).

Fluorescence labelling of dendritic cells

BMDCs were differentiated and matured as previously described. Mature DCs were harvested, counted and adjusted to 1×10^7 cells/ml in room temperate 1xPBS. For labelling, Tetra-Methylrhodamine (TAMRA; TAMRA, SE; 5-(and-6)-Carboxytetramethylrhodamine, Succinimidyl Ester (5(6)-TAMRA, SE; Invitrogen), Oregon Green® (CellTrace™ Oregon Green® 488 carboxylic acid diacetate, succinimidyl ester carboxy-DFFDA, SE; Invitrogen) or eFluor® 670 (Cell Proliferation Dye eFluor® 670; eBioscience) was added to a final

concentration of 10 μM TAMRA, 3 μM Oregon Green® or 1 μM eFluor® 670, respectively. After 10 min incubation fresh R10 medium was added to the cell suspension to stop the reaction and cells were pelleted. Subsequently, cells were resuspended in pre-warmed (37°C) R10 medium and incubated for another 30 minutes at 37°C for esterification. Finally, cells were washed twice with 1xPBS and subsequently used for experiments (crawl in assay, *in vivo* migration assay).

Ex vivo crawl in assay (end point analysis)

This assay was performed according to a modified protocol described in detail ((Weber and Sixt)), however instead of live cell imaging it was used as an end point method. Here, the migration potential of *WT* and *Hem1*^{-/-} DCs into lymphatic vessels of unfixed ventral ear sheets after two hours was evaluated. In brief, 4-6 weeks old C57BL/6 mice were sacrificed, ears split and the cartilage-free ventral ear half was spread carefully over the lid of sample tube (1.5 ml) with the dermis side up. The ear sheet was fixed using a ring made of the other have of the tube. This setup was then mounted on 5 cm culture dish. BMDCs were fluorescence labelled as described above. TAMRA-labelled wildtype DCs and eFluor® 670-labelled knockout DCs (*Hem1*^{-/-} or *WASP*^{-/-}), or *vice versa*, were mixed at 1:1 ratio and adjusted to a final concentration of 5×10^6 cells/ml in R10 medium. A volume of 100 μl (= 5×10^5 cells) were applied to one ear sheet and incubated for 5-10 minutes at 37°C, 5% CO_2 to allow migration into the tissue. Subsequent washing of the ear explant with R10 medium removed non-infiltrated DCs. Ears were then covered with fresh R10 medium and incubated for another 2 hours at 37°C, 5% CO_2 to allow DC migration towards and into the lymphatic vessels. After "crawl in", ear explants were washed with 1xPBS and incubated in fixation buffer for 1-3 days at 4°C. Afterwards, the lymphatic vessels of the ears were immunostained by using α-LYVE1 (1:300 in R10 medium). Ear explants were incubated for 45-60 minutes at RT and subsequently washed three times with R10 medium. The secondary antibody – conjugated with Alexa Fluor 488 (Jackson) – was applied (1:400 in R10) and explants were incubated for another 45 min at RT in the dark. After the final three washes with R10 medium the ear halves were used for confocal imaging (dermis facing upwards).

End point images were acquired with the upright SP5 confocal microscope (Leica) equipped with the following objectives: HCX IRAPO L 25x/0.95 W (11506323), WD=2.5 mm; HC PL FL 10x/0.3 PH1 (11506507), WD=11.0 mm.

<u>Fixation buffer:</u> *1% (w/v) paraformaldehyde (PFA, Sigma-Aldrich) in 1xPBS*

In vivo migration assay

Mature DCs were fluorescently labelled with 10 μM TAMRA or 3 μM Oregon Green® (Invitrogen) as described. Wildtype and knockout (*Hem1*^{-/-} or *WASP*^{-/-}) were differently labelled, mixed at 1:1 ratio and adjusted to a final concentration of 4×10^7 cells/ml in 1xPBS. 25 μl (= 1×10^6 cells) were injected into the mouse hind footpads. Draining popliteal LNs were harvested after 24 hours and transferred to a polystyrene FACS tube (Falcon BD) containing

0.5 ml complete DMEM for subsequent isolation of the DCs for flow cytometry analysis (one LN per tube) (the protocol was kindly provided by Prof. Dr. Sanjiv Luther, Lausanne). LNs were then opened and cut into pieces in the tube using sterile scissors. Afterwards LN fragments were digested by the addition of collagenase D, DNaseI and $CaCl_2$ (see digestion buffer bellow). Digestion occurred for 30 min at 37°C in a water bath and solution was thoroughly pipetted every 10 minutes using a 1 ml pipette to further disrupt the fragments. The enzymatic reaction was stopped after 30 minutes by the addition of 10 mM EDTA. Cell solution was again thoroughly pipetted to disrupt remaining LN fragments and subsequently flushed through a cell strainer into a fresh FACS tube (tube with cell strainer cap, BD Falcon). Cells were pelleted by centrifugation washed once with 1xPBS and resuspended in FACS buffer. Cells were stained for CD11c and MHC II as described.

Complete DMEM: *2.5% FCS (Gibco), 10 mM HEPES (Sigma-Aldrich), 5% penicillin/ streptomycin (Gibco) and 5 % glutamine (Gibco)*

Digestion buffer: *complete DMEM, 3mM $CaCl_2$ (Sigma-Aldrich), 0.5 mg/ml collagenase D (Roche), 40 µg/ml DNase I (Roche)*

EDTA 0.5 M, pH 7.2: *Ethylenediaminetetraacetic acid (EDTA, Sigma-Aldrich)*

In vitro confined migration

To confine DCs and observe their migration behaviour, an array of micropillars was used (protocol was obtained from Mael Le Berre, Institut Curie, France).

The micropillars were fabricated from a mould obtained by lithography (Jack Merrin, IST Austria, Fig. 35A). Briefly, a layer of photo-resist (SU8) was spin-coated directly on a silicon wafer and soft-baked to obtain a 4 µm height photo-resist. The micropillar pattern was created by UV-exposure through a photo-mask. After development, the resist formed the conjugate of round micropillars (4µm in height, 300µm width separated of each other by 300µm), which was used as a mould to fabricate the micropillars with polypimethylpiloxane (PDMS) (RTV615, GE). After pouring a small amount of vacuumed PDMS mix of liquid elastomer and polymer (8:1, w:w) on the mould, plasma cleaned (Harrick Plasma) round cover slips (ThermoFisher, 12 mm, #1) were pushed gently onto the surface of the mould to eliminate excessive PDMS. Subsequently, the mould was placed on a heating plate (IKA® C-MAG HP7) and baked at 90°C for 15 minutes. Afterwards, the excess polymerized PDMS was carefully removed, the coverslips coated with PDMS micropillars were gently detached by rinsing with 2-propanol (Sigma-Aldrich). The coverslips were then placed on self-made PDMS pillars, which were stuck on the inside of a cell culture dish lid (6cm) (Fig. 35B, left). For the pillars, a vacuumed PDMS mix (25:1) was poured into the pillar mould (IST Austria Miba Machine Shop) and baked overnight at 70°C. The polymerized pillars were carefully removed from the mould, cleaned with 2-propanol and glued to the lid using a silicone sealant (Marina). In parallel, a hole (12 mm in diameter) was cut in the bottom part of the

dish (IST machine shop) and a cover slip (Menzel Gläser, 22 x 22mm, #1) was glued on the outside using silicon glue (Fig. 35B, right). The bottom and the lid were subsequently plasma cleaned and if needed PEG-coated (PLL-PEG, SuSoS AG see above).

Before the migration assay, the migration chambers were pre-incubated with 10 ml R10

A

SU-8
Si

Dispensing SU-8
photoresist on a Si wafer

Spin-coating & soft bake

Mask aligning

Exposure with a UV lamp

Photo resist containing the
conjugate of round micropillars

B

coverslip incl. micropillars

PDMS pilllar
glued to lid

cell culture dish lid

a hole was cut in the
middle of the dish bottom

hole was sealed with a
glass coverslip

cell culture dish bottom

C

cell suspension

Figure 35. Preparation steps for the cell confinement setup. (A) Schematic illustration of the mould fabrication by UV lithography. (B) Assembly scheme for (*left*) the cell culture dish lid including the PDMS pillar the micropatterned coverslip on top; (*right*) the cell culture dish bottom with a cut 12 mm hole sealed with a glass coverslip. (C) A drop of cell solution was put on the micropatterned coverslip of the confining lid and placed on the prepared bottom dish containing R10 medium. Cells migrated in between the micropillars.

for 1 hour at 37°C/ 5% CO_2 (Fig. 35C). For confined migration, the medium was removed and 3-10 x 10^4 cells in 2-5 μl were applied on top of the micropatterned coverslip of the confining lid and pressed thoroughly to the coverslip of the dish bottom (Fig. 35C, middle). Whilst applying pressure, the lid and bottom dish were sealed with a tape at the dish edges to fix the confinement state (Fig. 35C, right). After an incubation of 30-60 minutes at 37°C/ 5% CO_2, cell migration was observed on a conventional inverted stereomicroscope (Leica DM IL LEDs).

PDMS mix for micropillars: _Sylgard 184 silicone elastomer and RTV615 (GE) polymer (both Dow Corning) in a 8:1 ratio (w/w)_

PDMS mix for pillars: _Sylgard 184 silicone elastomer and RTV615 (GE) polymer (both Dow Corning) in a 25:1 ratio (w/w)_

Microscopy

Time lapse microscopy: brightfield, DIC and TIRF

Experiments were performed at 37°C with 5% CO_2 in a humidified and heated chamber using a Leica DM IL LEDs microscope operated via FireWire Recorder software (custom made, SVS-Vistek). Up to six samples were analysed simultaneously using six individual setups, thereby allowing the same conditions for controls and probes.

Total internal reflection (TIRF) microscopy and differential interference contrast (DIC) were performed with an inverted Axiovert 200 (Zeiss) microscope, a TIRF 488/561-nm laser system (Visitron systems) and an Evolve™ EMCCD camera (Photometrics) triggered by VisiView software (Visitron).

Confocal microscopy

Images of ear explants after _ex vivo_ crawl-in assays were acquired with the upright confocal laser-scanning microscope (Leica SP5) equipped with the following objectives: HC PL FL 10x/0.3 PH1 (11506507), WD=11.0 mm, HCX IRAPO L 25x/0.95 W (11506323), WD=2.5 mm. Images were acquired, processed and evaluated using FIJI image processing software.

EM microscopy

For routine inspection of samples 200mesh hexagonal (Agar Scientific) nickel grids were stained with 60μl 2% sodium silicotungstate (SST) with 1μg/ml phalloidin and imaged on an 80kV transmission electron microscope (Morgagni, FEI).

For electron tomography Formvar-coated 200 mesh hexagonal Au grids (Agar Scientific) were stained with 6% SST including 1μg/ml phalloidin and around 1:10 BSA-gold colloid preparation from a gold stock. Tilt series were acquired on an FEI Tecnai F30 Helium (Polara) microscope, operated at 300 kV and cooled to approximately 80K. Automated acquisition of tilt series was driven by SerialEM 3.x. Normally, the tilt range was -60 to +60 using the Saxton tilt scheme based on 1° increments from 0° tilt, at a defocus value of -5μm.

For every sample two tilt series around orthogonal axes were recorded on a Gatan UltraScan 4000 CCD camera at magnifications typically from x31,000 to x39,000 with binning 2 giving a pixel size of typically 0.75 to 0.59nm per pixel.

Re-projections from the tilt series were generated using IMOD software from the Boulder Laboratory for 3D Electron Microscopy of Cells (Kremer et al., 1996), using the gold particles as fiducials for alignments. Using IMOD, filaments were manually tracked and models generated. A typical tomogram comprised a z-stack of 75-95 sections of 0.746nm each (~ 56-71nm in total).

Image analysis
Video quality enhancement
In general, image analysis was performed using FIJI image processing software (http://fiji.sc/Fiji). Videos were processed using background subtraction and low-pass filter as well as general brightness and contrast adjustments.

Manual cell tracking
Videos showing both migrating cells and surrounding tissue were imported as .stk-files to ImageJ (http://rsbweb.nih.gov/ij). Cells were tracked using the "Manual Tracking Plug-in" and analysis was done by implementing the "Chemotaxis Plug-in" (http://rsbweb.nih.gov/ij/).

Automated cell tracking
Chemotaxis assays using immature BMDCs were analysed using FIJI image processing software with a custom made automated tracking script (Robert Hauschild, IST Austria Imaging facility) (Fig. 36B). In brief, cell migration image sequences (brightfield) were edited using the implemented background subtraction tool. Thereby each single image was subtracted by the average intensity of the z-projection of the whole stack. This was followed by a particle filtering that discards objects much smaller (<7px) or larger (>40px) than the cells. Using the script, the lateral displacement of the entire image of frame t_o was calculated in such a way that the overlap with the image of the following frame t_1 was maximized (Fig. 36A). Migration speed was calculated from y-displacement in µm divided by the time between two consecutive frames (*here:* 30 seconds).

Kymograph analysis
Kymographs are used to graphically represent a spatial position (point/line) over time, in which a spatial axis represents time. In image analysis it is a way to represent dynamic processes on a single image. Here we employed kymograph analysis to observe the dynamics of proteins involved in actin polymerization during cell migration. Proteins were transiently expressed as GFP-fusions and monitored over time by their fluorescent signal using time-lapse TIRF microscopy. Kymograph analysis was performed for a line segment of the obtained image stack. The kymographs can be seen as an *x-t* scan, in which the intensity along a given line is plotted for the images of a (time-) stack. Each time point gives an

intensity line, plotted *e.g.* along the x-axis of the kymograph. These lines are stacked along the y-axis for the indicated frames. So we get an image, which moves along space in the x direction and along time in the y direction. Arp2/3, WASp, VASP, actin dynamics and membrane flow were analysed by kymograph and line-scan analysis, using FIJI.

A

frame t_0 frame t_1

overlay frame t_0,t_1

read out displacement of **frame t_0** in y-direction to generate max. overlap of frame t_0,t_1

y
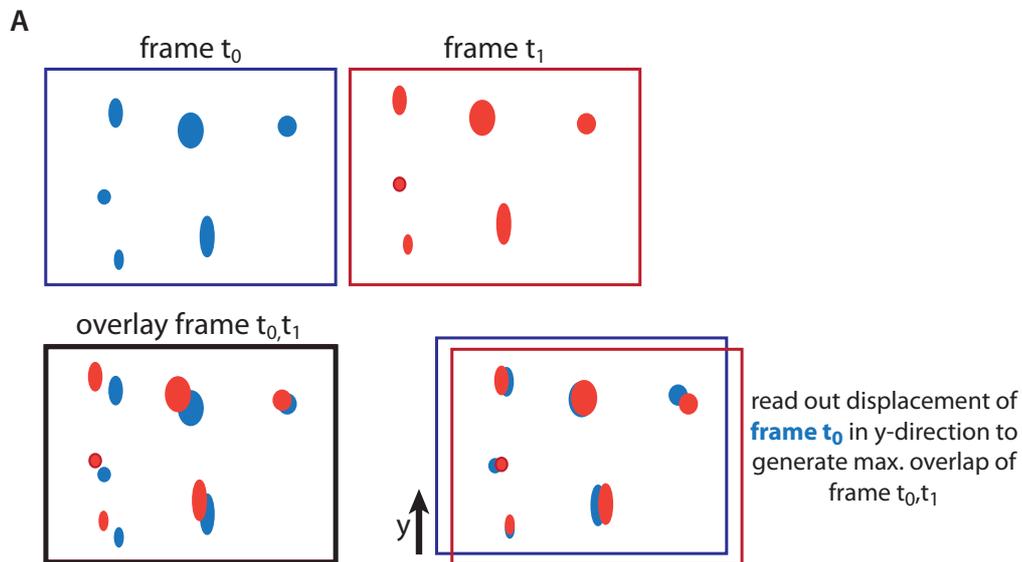
B

```
path = File.openDialog("Select a file");
open(path);
rename("Result of stack.tif");
run("32-bit");

getDimensions(width, height, channels, slices, frames);
stack_size=slices;
x_size=width;
y_size=height;

run("Z Project...", "start=1 stop="+stack_size+" projection=[Average Intensity]");
imageCalculator("Subtract create 32-bit stack", "Result of stack.tif","AVG_Result of stack.tif");
selectWindow("AVG_Result of stack.tif");
close();
selectWindow("Result of stack.tif");
close();
selectWindow("Result of Result of stack.tif");
rename("Result of stack.tif");

run("Bandpass Filter...", "filter_large=40 filter_small=7.5 suppress=None tolerance=5 autoscale saturate process");

for (i = 0; i < stack_size-2; i++) {

        newImage("f", "32-bit Black", x_size, y_size, 1);
        newImage("g", "32-bit Black", x_size, y_size, 1);
        selectWindow("Result of stack.tif");

        setSlice(i+1);
        run("Copy");

//      run("FFT Options...", "fft complex");

        selectWindow("f");
        run("Paste");
        run("Multiply...", "value=-1");
        changeValues(-10000,0,0);
//run("FFT");
//selectWindow("FFT of f");
//run("Close");

        run (Images to Stack", "name=Stack2 title=[] use);
        run("Image Stabilizer", "transformation=Translationmaximum_pyramid_levels=1
template_update_coefficient=0.90 maximum_iterations=200 error_tolerance=0.0000001 ");
selectWindow("Stack2");
        run("Close");
}
```

Figure 36. Automated cell tracking as a tool for the analysis of directional migration. (A) Simplified illustration of the used script. (B) Detailed FIJI script used.

Statistical analysis

Student's t-tests and analysis of variance (ANOVA) were performed after data was confirmed to fulfil the criteria of normal distribution and equal variance. Student´s t-test is used to compare the means of two samples and ANOVA to compare the means of three or more groups. Kruskal-Wallis tests or Mann-Whitney U-test were applied for data, which did not fulfil the criteria of t-test and ANOVA (normal distribution and equal variance). The Mann–Whitney U test is a non-parametric statistical hypothesis test for assessing whether two independent samples of observations have equally large values. The Kruskal–Wallis one-way analysis of variance by ranks is an extension of the Mann–Whitney U test to three or more groups. For post-hoc test of Kruskal-Wallis tests' data were pairwise compared with Dunn´s method; ANOVA tests' data were pairwise compared with Bonferroni´s method. All analyses were performed with GraphPad Prism.

BIBLIOGRAPHY

Abercrombie, M. (1980). The Croonian Lecture, 1978: The Crawling Movement of Metazoan Cells. pp. 129–147.

Abercrombie, M., Heaysman, J., and Pegrum, S.M. (1970). The locomotion of fibroblasts in culture: III. Movements of particles on the dorsal surface of the leading lamella. Exp. Cell Res. *62*, 389-398.

Al-Alwan, M.M., Liwski, R.S., Haeryfar, S.M., Baldridge, W.H., Hoskin, D.W., Rowden, G., and West, K.A. (2003). Cutting edge: dendritic cell actin cytoskeletal polarization during immunological synapse formation is highly antigen-dependent. The Journal of Immunology *171*, 4479–4483.

Alexandrova, A.Y., Arnold, K., Schaub, S., Vasiliev, J.M., Meister, J.-J., Bershadsky, A.D., and Verkhovsky, A.B. (2008). Comparative dynamics of retrograde actin flow and focal adhesions: formation of nascent adhesions triggers transition from fast to slow flow. PLoS ONE *3*, e3234.

Allen, W.E., Zicha, D., Ridley, A.J., and Jones, G.E. (1998). A role for Cdc42 in macrophage chemotaxis. The Journal of Cell Biology *141*, 1147–1157.

Alvarez, D., Vollmann, E.H., and Andrian, von, U.H. (2008). Mechanisms and consequences of dendritic cell migration. Immunity *29*, 325–342.

Amann, K.J., and Pollard, T.D. (2001). The Arp2/3 complex nucleates actin filament branches from the sides of pre-existing filaments. Nat Cell Biol *3*, 306–310.

Ananthakrishnan, R., and Ehrlicher, A. (2007). The forces behind cell movement. International Journal of Biological Sciences *3*, 303.

Antón, I.M., Jones, G.E., Wandosell, F., Geha, R., and Ramesh, N. (2007). WASP-interacting protein (WIP): working in polymerisation and much more. Trends Cell Biol. *17*, 555–562.

Arrieumerlou, C., and Meyer, T. (2005). A local coupling model and compass parameter for eukaryotic chemotaxis. Developmental Cell *8*, 215–227.

Azuma, T. (1998). Gelsolin is a downstream effector of rac for fibroblast motility. Embo J. *17*, 1362–1370.

Banchereau, J., and Steinman, R.M. (1998). Dendritic cells and the control of immunity. Nature *392*, 245-252.

Barnden, M.J., Allison, J., Heath, W.R., and Carbone, F.R. (1998). Defective TCR expression in transgenic mice constructed using cDNA-based alpha- and beta-chain genes under the control of heterologous regulatory elements. Immunol Cell Biol *76*, 34–40.

Bear, J.E., and Gertler, F.B. (2009). Ena/VASP: towards resolving a pointed controversy at the barbed end. Journal of Cell Science *122*, 1947–1953.

Bear, J.E., Loureiro, J.J., Libova, I., Fässler, R., Wehland, J., and Gertler, F.B. (2000). Negative regulation of fibroblast motility by Ena/VASP proteins. Cell *101*, 717–728.

Beli, P., Mascheroni, D., Xu, D., and Innocenti, M. (2008). WAVE and Arp2/3 jointly inhibit filopodium formation by entering into a complex with mDia2. Nature *10*, 849–857.

Benvenuti, F., Lagaudrière-Gesbert, C., Grandjean, I., Jancic, C., Hivroz, C., Trautmann, A., Lantz, O., and Amigorena, S. (2004). Dendritic cell maturation controls adhesion, synapse formation, and the duration of the interactions with naive T lymphocytes. J Immunol *172*, 292–301.

Blanchoin, L., Amann, K.J., Higgs, H.N., Marchand, J.B., Kaiser, D.A., and Pollard, T.D. (2000). Direct observation of dendritic actin filament networks nucleated by Arp2/3 complex and WASP/Scar proteins. Nature *404*, 1007–1011.

Blaser, H., Reichman-Fried, M., Castanon, I., Dumstrei, K., Marlow, F.L., Kawakami, K., Solnica-Krezel, L., Heisenberg, C.-P., and Raz, E. (2006). Migration of zebrafish primordial germ cells: a role for myosin contraction and cytoplasmic flow. Developmental Cell *11*, 613–627.

Block, J., Breitsprecher, D., Kühn, S., Winterhoff, M., Kage, F., Geffers, R., Duwe, P., Rohn, J.L., Baum, B., Brakebusch, C., et al. (2012). FMNL2 drives actin-based protrusion and migration downstream of Cdc42. Curr. Biol. *22*, 1005–1012.

Bosticardo, M., Marangoni, F., Aiuti, A., Villa, A., and Grazia Roncarolo, M. (2009). Recent advances in understanding the pathophysiology of Wiskott-Aldrich syndrome. Blood *113*, 6288–6295.

Bouma, G., Burns, S., and Thrasher, A.J. (2007). Impaired T-cell priming in vivo resulting from dysfunction of WASp-deficient dendritic cells. Blood *110*, 4278–4284.

Bouma, G., Mendoza-Naranjo, A., Blundell, M.P., de Falco, E., Parsley, K.L., Burns, S.O., and Thrasher, A.J. (2011). Cytoskeletal remodeling mediated by WASp in dendritic cells is necessary for normal immune synapse formation and T cell priming. Blood *118*, 2492-2501.

Bouma, G., Burns, S.O., and Thrasher, A.J. (2009). Wiskott–Aldrich Syndrome Immunodeficiency resulting from defective cell migration and impaired immunostimulatory activation. Immunobiology *214*, 778–790.

Bourguignon, L.Y., and Bourguignon, G.J. (1984). Capping and the cytoskeleton. Int. Rev. Cytol. *87*, 195–224.

Bray, D., and White, J.G. (1988). Cortical flow in animal cells. Science *239*, 883–888.

Bray, D., Heath, J., and Moss, D. (1986). The membrane-associated "cortex" of animal cells:

its structure and mechanical properties. J. Cell Sci. Suppl. *4*, 71–88.

Bretscher, M.S. (1976). Directed lipid flow in cell membranes. Nature *260*, 21–23.

Bretscher, M.S. (2008). Recap on cell migration. Traffic *9*, 198–199.

Burnette, D.T., Manley, S., Sengupta, P., Sougrat, R., Davidson, M.W., Kachar, B., and Lippincott-Schwartz, J. (2011). A role for actin arcs in the leading-edge advance of migrating cells. Nat Cell Biol *13*, 371–381.

Cai, Y., Biais, N., Giannone, G., Tanase, M., Jiang, G., Hofman, J.M., Wiggins, C.H., Silberzan, P., Buguin, A., Ladoux, B., et al. (2006). Nonmuscle myosin IIA-dependent force inhibits cell spreading and drives F-actin flow. Biophysical Journal *91*, 3907–3920.

Cain, R.J., and Ridley, A.J. (2009). Phosphoinositide 3-kinases in cell migration. Biol. Cell *101*, 13–29.

Calvez, R., Lafouresse, F., De Meester, J., Galy, A., Valitutti, S., and Dupré, L. (2011). The Wiskott-Aldrich syndrome protein permits assembly of a focused immunological synapse enabling sustained T-cell receptor signaling. Haematologica *96*, 1415–1423.

Campellone, K.G., and Welch, M.D. (2010). A nucleator arms race: cellular control of actin assembly. Nat Rev Mol Cell Biol *11*, 237–251.

Campellone, K.G.K., Webb, N.J.N., Znameroski, E.A.E., and Welch, M.D.M. (2008). WHAMM Is an Arp2/3 Complex Activator That Binds Microtubules and Functions in ER to Golgi Transport. Cell *134*, 14–14.

Carlier, M.F., and Pantaloni, D. (2007). Control of Actin Assembly Dynamics in Cell Motility. J. Biol. Chem. *282*, 23005–23009.

Caton, M.L., Smith-Raska, M.R., and Reizis, B. (2007). Notch-RBP-J signaling controls the homeostasis of CD8- dendritic cells in the spleen. Journal of Experimental Medicine *204*, 1653-1664.

Charras, G.T. (2008). A short history of blebbing. J Microsc *231*, 466–478.

Charras, G., and Paluch, E. (2008). Blebs lead the way: how to migrate without lamellipodia. Nat Rev Mol Cell Biol *9*, 730–736.

Charras, G.T., Hu, C.-K., Coughlin, M., and Mitchison, T.J. (2006). Reassembly of contractile actin cortex in cell blebs. The Journal of Cell Biology *175*, 477–490.

Charras, G.T., Yarrow, J.C., Horton, M.A., Mahadevan, L., and Mitchison, T.J. (2005). Non-equilibration of hydrostatic pressure in blebbing cells. Nature *435*, 365–369.

Chesarone, M.A., and Goode, B.L. (2009). Actin nucleation and elongation factors: mechanisms and interplay. Current Opinion in Cell Biology *21*, 28–37.

Chhabra, E.S., and Higgs, H.N. (2007). The many faces of actin: matching assembly factors with cellular structures. Nat Cell Biol *9*, 1110–1121.

Choi, C.K., Vicente-Manzanares, M., Zareno, J., Whitmore, L.A., Mogilner, A., and Horwitz, A.R. (2008). Actin and alpha-actinin orchestrate the assembly and maturation of nascent adhesions in a myosin II motor-independent manner. Nat Cell Biol *10*, 1039–1050.

Chung, C.Y., Funamoto, S., and Firtel, R.A. (2001). Signaling pathways controlling cell polarity and chemotaxis. Trends Biochem. Sci. *26*, 557–566.

Cory, G.O.C., Garg, R., Cramer, R., and Ridley, A.J. (2002). Phosphorylation of tyrosine 291 enhances the ability of WASp to stimulate actin polymerization and filopodium formation. Wiskott-Aldrich Syndrome protein. Journal of Biological Chemistry *277*, 45115–45121.

Derivery, E., Fink, J., Martin, D., Houdusse, A., and Piel, M. (2008). Free Brick1 is a trimeric precursor in the assembly of a functional wave complex. PLoS One *3*, e2462.

Derivery, E., Sousa, C., Gautier, J.J., Lombard, B., Loew, D., and Gautreau, A. (2009). The Arp2/3 Activator WASH Controls the Fission of Endosomes through a Large Multiprotein Complex. Developmental Cell *17*, 712–723.

Derry, J.M., Ochs, H.D., and Francke, U. (1994). Isolation of a novel gene mutated in Wiskott-Aldrich syndrome. Cell *78*, 635-644.

Devreotes, P.P., and Janetopoulos, C.C. (2003). Eukaryotic chemotaxis: distinctions between directional sensing and polarization. Journal of Biological Chemistry *278*, 20445–20448.

Disanza, A., Steffen, A., Hertzog, M., Frittoli, E., Rottner, K., and Scita, G. (2005). Actin polymerization machinery: the finish line of signaling networks, the starting point of cellular movement. Cell. Mol. Life Sci. *62*, 955–970.

Dittrich, M., Strassberger, V., Fackler, M., Tas, P., Lewandrowski, U., Sickmann, A., Walter, U., Dandekar, T., and Birschmann, I. (2010). Characterization of a Novel Interaction Between Vasodilator-Stimulated Phosphoprotein and Abelson Interactor 1 in Human Platelets: A Concerted Computational and Experimental Approach. Arteriosclerosis, Thrombosis, and Vascular Biology *30*, 843–850.

Diz-Muñoz, A., Krieg, M., Bergert, M., Ibarlucea-Benitez, I., Muller, D.J., Paluch, E., and Heisenberg, C.-P. (2010). Control of directed cell migration in vivo by membrane-to-cortex attachment. Plos Biol *8*, e1000544.

Driscoll, M.K., McCann, C., Kopace, R., Homan, T., Fourkas, J.T., Parent, C., and Losert, W. (2012). Cell shape dynamics: from waves to migration. PLoS Comp Biol *8*, e1002392.

Dustin, M.L., and Cooper, J.A. (2000). The immunological synapse and the actin cytoskeleton: molecular hardware for T cell signaling - Nature Immunology. Nat. Immunol. *1*, 23–29.

Eisenmann, K.M., Harris, E.S., Kitchen, S.M., Holman, H.A., Higgs, H.N., and Alberts, A.S. (2007). Dia-interacting protein modulates formin-mediated actin assembly at the cell cortex. Curr. Biol. *17*, 579–591.

Etienne-Manneville, S. (2004). Cdc42 - the centre of polarity. Journal of Cell Science *117*, 1291–1300.

Etienne-Manneville, S., and Hall, A. (2002). Rho GTPases in cell biology. Nature *420*, 629–635.

Etienne-Manneville, S., and Hall, A. (2003). Cell polarity: Par6, aPKC and cytoskeletal crosstalk. Current Opinion in Cell Biology *15*, 67–72.

Evers, E.E., Zondag, G.C.M., Malliri, A., Price, L.S., Klooster, ten, J.P., van der Kammen, R.A., and Collard, J.G. (2000). Rho family proteins in cell adhesion and cell migration. European Journal of Cancer *36*, 1269–1274.

Faure-André, G., Vargas, P., Yuseff, M.-I., Heuzé, M., Diaz, J., Lankar, D., Steri, V., Manry, J., Hugues, S., Vascotto, F., et al. (2008). Regulation of dendritic cell migration by CD74, the MHC class II-associated invariant chain. Science *322*, 1705–1710.

Fehon, R.G., McClatchey, A.I., and Bretscher, A. (2010). Organizing the cell cortex: the role of ERM proteins. Nat Rev Mol Cell Biol *11*, 276–287.

Ferron, F., Rebowski, G., Lee, S.H., and Dominguez, R. (2007). Structural basis for the recruitment of profilin–actin complexes during filament elongation by Ena/VASP. Embo J. *26*, 4597–4606.

Fink, R.D., and Trinkaus, J.P. (1988). Fundulus deep cells: directional migration in response to epithelial wounding. Dev. Biol. *129*, 179–190.

Friedl, P., and Wolf, K. (2010). Plasticity of cell migration: a multiscale tuning model. The Journal of Cell Biology *188*, 11–19.

Friedl, P., Borgmann, S., and Bröcker, E.B. (2001). Amoeboid leukocyte crawling through extracellular matrix: lessons from the Dictyostelium paradigm of cell movement. J. Leukoc. Biol. *70*, 491–509.

Friedl, P., Entschladen, F., Conrad, C., Niggemann, B., and Zänker, K.S. (1998a). CD4+ T lymphocytes migrating in three-dimensional collagen lattices lack focal adhesions and utilize beta1 integrin-independent strategies for polarization, interaction with collagen fibers and locomotion. Eur. J. Immunol. *28*, 2331–2343.

Friedl, P., Zänker, K.S., and Bröcker, E.B. (1998b). Cell migration strategies in 3-D extracellular matrix: differences in morphology, cell matrix interactions, and integrin function. Microsc. Res. Tech. *43*, 369–378.

Friedl, P., and Wolf, K. (2003). Proteolytic and non-proteolytic migration of tumour cells and

leucocytes. Biochem. Soc. Symp. 277–285.

Galbraith, C.G., Yamada, K.M., and Galbraith, J.A. (2007). Polymerizing actin fibers position integrins primed to probe for adhesion sites. Science *315*, 992–995.

Giannone, G., Dubin-Thaler, B.J., Rossier, O., Cai, Y., Chaga, O., Jiang, G., Beaver, W., Döbereiner, H.-G., Freund, Y., Borisy, G., et al. (2007). Lamellipodial Actin Mechanically Links Myosin Activity with Adhesion-Site Formation. Cell *128*, 561–575.

Gilden, J., and Krummel, M.F. (2010). Control of cortical rigidity by the cytoskeleton: Emerging roles for septins. Cytoskeleton *67*, 477–486.

Goley, E.D., and Welch, M.D. (2006). The ARP2/3 complex: an actin nucleator comes of age. Nat Rev Mol Cell Biol *7*, 713–726.

Gomez, T.S., and Billadeau, D.D. (2009). A FAM21-Containing WASH Complex Regulates Retromer-Dependent Sorting. Developmental Cell *17*, 699–711.

Gómez-Moutón, C., Lacalle, R.A., Mira, E., Jiménez-Baranda, S., Barber, D.F., Carrera, A.C., Martínez-A, C., and Mañes, S. (2004). Dynamic redistribution of raft domains as an organizing platform for signaling during cell chemotaxis. The Journal of Cell Biology *164*, 759–768.

Gupton, S.L., Anderson, K.L., Kole, T.P., Fischer, R.S., Ponti, A., Hitchcock-DeGregori, S.E., Danuser, G., Fowler, V.M., Wirtz, D., Hanein, D., et al. (2005). Cell migration without a lamellipodium: translation of actin dynamics into cell movement mediated by tropomyosin. The Journal of Cell Biology *168*, 619–631.

Hafner, M.M., Wenk, J.J., Nenci, A.A., Pasparakis, M.M., Scharffetter-Kochanek, K.K., Smyth, N.N., Peters, T.T., Kess, D.D., Holtkötter, O.O., Shephard, P.P., et al. (2004). Keratin 14 Cre transgenic mice authenticate keratin 14 as an oocyte-expressed protein. Genesis *38*, 176–181.

Han, Y., Eppinger, E., Schuster, I.G., Weigand, L.U., Liang, X., Kremmer, E., Peschel, C., and Krackhardt, A.M. (2009). Formin-like 1 (FMNL1) is regulated by N-terminal myristoylation and induces polarized membrane blebbing. J. Biol. Chem. *284*, 33409–33417.

Hanakam, F., Albrecht, R., Eckerskorn, C., Matzner, M., and Gerisch, G. (1996). Myristoylated and non-myristoylated forms of the pH sensor protein hisactophilin II: intracellular shuttling to plasma membrane and nucleus monitored in real time by a fusion with green fluorescent protein. Embo J. *15*, 2935–2943.

Hannemann, S., Madrid, R., Stastna, J., Kitzing, T., Gasteier, J., Schönichen, A., Bouchet, J., Jimenez, A., Geyer, M., Grosse, R., et al. (2008). The Diaphanous-related Formin FHOD1 associates with ROCK1 and promotes Src-dependent plasma membrane blebbing. Journal of Biological Chemistry *283*, 27891–27903.

Harms, B.D., Bassi, G.M., Horwitz, A.R., and Lauffenburger, D.A. (2005). Directional

122

persistence of EGF-induced cell migration is associated with stabilization of lamellipodial protrusions. Biophysical Journal *88*, 1479–1488.

Haston, W.S., and Shields, J.M. (1984). Contraction waves in lymphocyte locomotion. Journal of Cell Science *68*, 227–241.

Hewitt, J.A. (1979). Surf-riding model for cell capping. Journal of Theoretical Biology *80*, 115–127.

Higgs, H.N., and Peterson, K.J. (2005). Phylogenetic analysis of the formin homology 2 domain. Mol. Biol. Cell *16*, 1–13.

Hitz, C., Wurst, W., and Kühn, R. (2007). Conditional brain-specific knockdown of MAPK using Cre/loxP regulated RNA interference. Nucleic Acids Research *35*, e90.

Hogue, M.J. (1919). The effect of hypotonic and hypertonic solutions on fibroblasts of the embryonic chick heart *in vitro*. J. Exp. Med. *30*, 617–648.

Holtfreter, J. (1943). A study of the mechanics of gastrulation. Part I. J. Exp. Zool. *94*, 261–318.

Howard, J. (2001). Mechanics of Motor Proteins and the Cytoskeleton. Catalog. Sinauer Associates. Sunderland, MA.

Huttenlocher, A., Sandborg, R.R., and Horwitz, A.F. (1995). Adhesion in cell migration. Current Opinion in Cell Biology *7*, 697–706.

Huttenlocher, A., and Horwitz, A.R. (2011). Integrins in cell migration. Cold Spring Harb Perspect Biol *3*, a005074.

Ibáñez, C.F. (2004). Lipid rafts as organizing platforms for cell chemotaxis and axon guidance. Neuron *42*, 3–5.

Iglesias, P.A., and Devreotes, P.N. (2008). Navigating through models of chemotaxis. Current Opinion in Cell Biology *20*, 35–40.

Innocenti, M., Zucconi, A., Disanza, A., and Frittoli, E. (2004). Abi1 is essential for the formation and activation of a WAVE2 signalling complex. Nature Cell Biology *6*, 319-327.

Itoh, R.E., Kurokawa, K., Ohba, Y., Yoshizaki, H., Mochizuki, N., and Matsuda, M. (2002). Activation of rac and cdc42 video imaged by fluorescent resonance energy transfer-based single-molecule probes in the membrane of living cells. Mol Cell Biol *22*, 6582–6591.

Jacobelli, J., Bennett, F.C., Pandurangi, P., Tooley, A.J., and Krummel, M.F. (2009). Myosin-IIA and ICAM-1 regulate the interchange between two distinct modes of T cell migration. J Immunol *182*, 2041–2050.

Johnson, D.I. (1999). Cdc42: An essential Rho-type GTPase controlling eukaryotic cell polarity. Microbiol. Mol. Biol. Rev. *63*, 54–105.

Kageyama, T. (1977). Motility and locomotion of embryonic cells of the Medaka, *Oryzias Latipes*, during early development. Development, Growth and Differerntiation *19*, 103–110.

Kobayashi, K. (1998). p140Sra-1 (Specifically Rac1-associated Protein) Is a Novel Specific Target for Rac1 Small GTPase. Journal of Biological Chemistry *273*, 291–295.

Koestler, S.A., Auinger, S., Vinzenz, M., Rottner, K., and Small, J.V. (2008). Differentially oriented populations of actin filaments generated in lamellipodia collaborate in pushing and pausing at the cell front. Nature *10*, 306–313.

Kölsch, V., Charest, P.G., and Firtel, R.A. (2008). The regulation of cell motility and chemotaxis by phospholipid signaling. Journal of Cell Science *121*, 551–559.

Kremer, J.R., Mastronarde, D.N., and McIntosh, J.R. (1996). Computer visualization of three-dimensional image data using IMOD. Journal of Structural Biology *116*, 71-76.

Kress, H., Stelzer, E.H.K., Holzer, D., Buss, F., Griffiths, G., and Rohrbach, A. (2007). Filopodia act as phagocytic tentacles and pull with discrete steps and a load-dependent velocity. Proc. Natl. Acad. Sci. U.S.a. *104*, 11633–11638.

Krummel, M.F., and Macara, I. (2006). Maintenance and modulation of T cell polarity. Nat. Immunol. *7*, 1143–1149.

Kubota, H.Y. (1981). Creeping locomotion of the endodermal cells dissociated from gastrulae of the Japanese newt, Cynops pyrrhogaster. Exp. Cell Res. *133*, 137–148.

Kunda, P., Craig, G., Dominguez, V., and Baum, B. (2003). Abi, Sra1, and Kette control the stability and localization of SCAR/WAVE to regulate the formation of actin-based protrusions. Current Biology *13*, 1867-1875.

Kurokawa, K. (2005). Localized RhoA Activation as a Requirement for the Induction of Membrane Ruffling. Mol. Biol. Cell *16*, 4294–4303.

Ladwein, M., and Rottner, K. (2008). On the Rho'd: The regulation of membrane protrusions by Rho-GTPases. FEBS Letters *582*, 2066-2074.

Lammermann, T., Renkawitz, J., Wu, X., Hirsch, K., Brakebusch, C., and Sixt, M. (2009). Cdc42-dependent leading edge coordination is essential for interstitial dendritic cell migration. Blood *113*, 5703–5710.

Langridge, P.D., and Kay, R.R. (2006). Blebbing of Dictyostelium cells in response to chemoattractant. Exp. Cell Res. *312*, 2009–2017.

Lauffenburger, D.A., Tranquillo, R.T., and Zigmond, S.H. (1988). Concentration gradients of chemotactic factors in chemotaxis assays. Meth. Enzymol. *162*, 85–101.

Lauffenburger, D., Farrell, B., Tranquillo, R., Kistler, A., and Zigmond, S. (1987). Gradient perception by neutrophil leucocytes, continued. Journal of Cell Science *88 (Pt 4)*, 415–416.

Lämmermann, T., and Sixt, M. (2009). Mechanical modes of "amoeboid" cell migration. Current Opinion in Cell Biology *21*, 636–644.

Lämmermann, T., Bader, B.L., Monkley, S.J., Worbs, T., Wedlich-Söldner, R., Hirsch, K., Keller, M., Förster, R., Critchley, D.R., Fässler, R., et al. (2008). Rapid leukocyte migration by integrin-independent flowing and squeezing. Nature *453*, 51–55.

Le Clainche, C., and Carlier, M.-F. (2008). Regulation of actin assembly associated with protrusion and adhesion in cell migration. Physiol. Rev. *88*, 489–513.

LeClaire, L.L., Baumgartner, M., Iwasa, J.H., Mullins, R.D., and Barber, D.L. (2008). Phosphorylation of the Arp2/3 complex is necessary to nucleate actin filaments. The Journal of Cell Biology *182*, 647–654.

Lefkowitz, R.J., and Whalen, E.J. (2004). β-arrestins: traffic cops of cell signaling. Current Opinion in Cell Biology *16*, 162–168.

Levayer, R., and Lecuit, T. (2012). Biomechanical regulation of contractility: spatial control and dynamics. Trends Cell Biol. *22*, 61–81.

Lewis, W.H. (1939). The role of a superficial plasmagel layer in changes of form, locomotion and division of cells in tissue cultures. Protoplasma *33*, 317–317.

Li, R., and Gundersen, G.G. (2008). Beyond polymer polarity: how the cytoskeleton builds a polarized cell. Nat Rev Mol Cell Biol *9*, 860–873.

Lommel, S., Benesch, S., Rottner, K., Franz, T., Wehland, J., and Kühn, R. (2001). Actin pedestal formation by enteropathogenic Escherichia coli and intracellular motility of Shigella flexneri are abolished in N-WASP-defective cells. EMBO Rep *2*, 850–857.

Lorenz, M., Yamaguchi, H., Wang, Y., Singer, R.H., and Condeelis, J. (2004). Imaging sites of N-wasp activity in lamellipodia and invadopodia of carcinoma cells. Curr. Biol. *14*, 697–703.

Lutz, M.B., Kukutsch, N., Ogilvie, A.L., Rößner, S., Koch, F., Romani, N., and Schuler, G. (1999). An advanced culture method for generating large quantities of highly pure dendritic cells from mouse bone marrow. Journal of Immunological Methods *223*, 77–92.

Machacek, M., Hodgson, L., Welch, C., Elliott, H., Pertz, O., Nalbant, P., Abell, A., Johnson, G.L., Hahn, K.M., and Danuser, G. (2009). Coordination of Rho GTPase activities during cell protrusion. Nature *461*, 99–103.

Machesky, L.M., Mullins, R.D., Higgs, H.N., Kaiser, D.A., Blanchoin, L., May, R.C., Hall, M.E., and Pollard, T.D. (1999). Scar, a WASp-related protein, activates nucleation of actin filaments by the Arp2/3 complex. Proc. Natl. Acad. Sci. U.S.a. *96*, 3739–3744.

Malawista, S.E., de Boisfleury Chevance, A., and Boxer, L.A. (2000). Random locomotion and chemotaxis of human blood polymorphonuclear leukocytes from a patient with leukocyte adhesion deficiency-1: normal displacement in close quarters via chimneying. Cell Motil.

Cytoskeleton *46*, 183–189.

Mallavarapu, A., and Mitchison, T. (1999). Regulated actin cytoskeleton assembly at filopodium tips controls their extension and retraction. The Journal of Cell Biology *146*, 1097–1106.

Mandeville, J.T., Lawson, M.A., and Maxfield, F.R. (1997). Dynamic imaging of neutrophil migration in three dimensions: mechanical interactions between cells and matrix. J. Leukoc. Biol. *61*, 188–200.

Martin, A.C., Welch, M.D., and Drubin, D.G. (2006). Arp2/3 ATP hydrolysis-catalysed branch dissociation is critical for endocytic force generation. Nat Cell Biol *8*, 826–833.

Maruoka, M., Sato, M., Yuan, Y., Ichiba, M., Fujii, R., Ogawa, T., Ishida-Kitagawa, N., Takeya, T., and Watanabe, N. (2011). Abi-1-bridged tyrosine phosphorylation of VASP by Abelson kinase impairs association of VASP to focal adhesions and regulates leukemic cell adhesion. Biochem J. *441*, 889-899.

Mast, S.O. (1926). Structure, movement, locomotion, and stimulation in amoeba. J. Morphol. *41*, 347–425.

Mattila, P.K., and Lappalainen, P. (2008). Filopodia: molecular architecture and cellular functions. Nat Rev Mol Cell Biol *9*, 446–454.

Mayer, M., Depken, M., Bois, J.S., Jülicher, F., and Grill, S.W. (2010). Anisotropies in cortical tension reveal the physical basis of polarizing cortical flows. Nature *467*, 617–621.

Medalia, O., Weber, I., Frangakis, A.S., Nicastro, D., Gerisch, G., and Baumeister, W. (2002). Macromolecular architecture in eukaryotic cells visualized by cryoelectron tomography. Science *298*, 1209–1213.

Mejillano, M.R.M., Kojima, S.-I.S., Applewhite, D.A.D., Gertler, F.B.F., Svitkina, T.M.T., and Borisy, G.G.G. (2004). Lamellipodial Versus Filopodial Mode of the Actin Nanomachinery - Pivotal Role of the Filament Barbed End. Cell *118*, 11–11.

Mellman, I.I., and Steinman, R.M.R. (2001). Dendritic Cells - Specialized and Regulated Antigen Processing Machines. Cell *106*, 4–4.

Mitchison, T.J., and Cramer, L.P. (1996). Actin-based cell motility and cell locomotion. Cell *84*, 371–379.

Morone, N., Fujiwara, T., Murase, K., Kasai, R.S., Ike, H., Yuasa, S., Usukura, J., and Kusumi, A. (2006). Three-dimensional reconstruction of the membrane skeleton at the plasma membrane interface by electron tomography. The Journal of Cell Biology *174*, 851–862.

Murphy, D.A., and Courtneidge, S.A. (2011). The 'ins' and "outs" of podosomes and invadopodia: characteristics, formation and function. Nat Rev Mol Cell Biol *12*, 413–426.

Muzumdar, M.D., Tasic, B., Miyamichi, K., Li, L., and Luo, L. (2007). A global double-fluorescent Cre reporter mouse. Genesis *45*, 593–605.

Narita, A., Mueller, J., Urban, E., Vinzenz, M., Small, J.V., Maéda, Y. (2012). Direct Determination of Actin Polarity in the Cell. J. Mol. Biol. *419*, 359.

Nemethova, M., Auinger, S., and Small, J.V. (2008). Building the actin cytoskeleton: filopodia contribute to the construction of contractile bundles in the lamella. The Journal of Cell Biology *180*, 1233–1244.

Nobes, C.D., and Hall, A. (1999). Rho GTPases control polarity, protrusion, and adhesion during cell movement. The Journal of Cell Biology *144*, 1235–1244.

Nobes, C.D., and Hall, A. (1995). Rho, Rac, and Cdc42 GTPases regulate the assembly of multimolecular focal complexes associated with actin stress fibers, lamellipodia, and filopodia. Cell *81*, 53–62.

Osmani, N., Peglion, F., Chavrier, P., and Etienne-Manneville, S. (2010). Cdc42 localization and cell polarity depend on membrane traffic. The Journal of Cell Biology *191*, 1261–1269.

Otero, C., Groettrup, M., and Legler, D.F. (2006). Opposite fate of endocytosed CCR7 and its ligands: recycling versus degradation. The Journal of Immunology *177*, 2314–2323.

Paluch, E., Piel, M., Prost, J., Bornens, M., and Sykes, C. (2005). Cortical actomyosin breakage triggers shape oscillations in cells and cell fragments. Biophysical Journal *89*, 724–733.

Pantaloni, D., Boujemaa, R., Didry, D., Gounon, P., and Carlier, M.F. (2000). The Arp2/3 complex branches filament barbed ends: functional antagonism with capping proteins. Nat Cell Biol *2*, 385–391.

Park, H., Staehling-Hampton, K., Appleby, M.W., Brunkow, M.E., Habib, T., Zhang, Y., Ramsdell, F., Liggitt, H.D., Freie, B., Tsang, M., et al. (2008). A point mutation in the murine Hem1 gene reveals an essential role for Hematopoietic Protein 1 in lymphopoiesis and innate immunity. Journal of Experimental Medicine *205*, 2899–2913.

Park, K.C., Rivero, F., Meili, R., Lee, S., Apone, F., and Firtel, R.A. (2004). Rac regulation of chemotaxis and morphogenesis in Dictyostelium. Embo J. *23*, 4177–4189.

Partridge, M.A., and Marcantonio, E.E. (2006). Initiation of attachment and generation of mature focal adhesions by integrin-containing filopodia in cell spreading. Mol. Biol. Cell *17*, 4237–4248.

Peitz, M., Pfannkuche, K., Rajewsky, K., and Edenhofer, F. (2002). Ability of the hydrophobic FGF and basic TAT peptides to promote cellular uptake of recombinant Cre recombinase: a tool for efficient genetic engineering of mammalian genomes. Proc. Natl. Acad. Sci. U.S.a. *99*, 4489–4494.

Pertz, O., Hodgson, L., Klemke, R.L., and Hahn, K.M. (2006). Spatiotemporal dynamics of

RhoA activity in migrating cells. Nature *440*, 1069–1072.

Petrie, R.J., Gavara, N., Chadwick, R.S., and Yamada, K.M. (2012). Nonpolarized signaling reveals two distinct modes of 3D cell migration. The Journal of Cell Biology *197*, 439–455.

Pflicke, H., and Sixt, M. (2009). Preformed portals facilitate dendritic cell entry into afferent lymphatic vessels. Journal of Experimental Medicine *206*, 2925–2935.

Pollard, T.D., and Cooper, J.A. (2009). Actin, a Central Player in Cell Shape and Movement. Science *326*, 1208–1212.

Ponti, A., Machacek, M., Gupton, S.L., Waterman-Storer, C.M., and Danuser, G. (2004). Two distinct actin networks drive the protrusion of migrating cells. Science *305*, 1782–1786.

Prehoda, K.E. (2000). Integration of Multiple Signals Through Cooperative Regulation of the N-WASP-Arp2/3 Complex. Science *290*, 801–806.

Premont, R.T., Bohn, L.M., and Lefkowitz, R.J. (2004). Desensitization of G protein-coupled receptors and neuronal functions. Annu Rev Neurosci. *27*, 107-144.

Pulecio, J., Petrovic, J., Prete, F., Chiaruttini, G., Lennon-Dumenil, A.M., Desdouets, C., Gasman, S., Burrone, O.R., and Benvenuti, F. (2010). Cdc42-mediated MTOC polarization in dendritic cells controls targeted delivery of cytokines at the immune synapse. Journal of Experimental Medicine *207*, 2719–2732.

Pulecio, J., Tagliani, E., Scholer, A., Prete, F., Fetler, L., Burrone, O.R., and Benvenuti, F. (2008). Expression of Wiskott-Aldrich syndrome protein in dendritic cells regulates synapse formation and activation of naive CD8+ T cells. J Immunol *181*, 1135–1142.

Renkawitz, J., Schumann, K., Weber, M., Lämmermann, T., Pflicke, H., Piel, M., Polleux, J., Spatz, J.P., and Sixt, M. (2009). Adaptive force transmission in amoeboid cell migration. Nat Cell Biol *11*, 1438–1443.

Ridley, A.J. (2006). Rho GTPases and actin dynamics in membrane protrusions and vesicle trafficking. Trends Cell Biol. *16*, 522–529.

Ridley, A.J. (2011). Life at the Leading Edge. Cell *145*, 1012–1022.

Riedl, J., Crevenna, A.H., Kessenbrock, K., Yu, J.H., Neukirchen, D., Bista, M., Bradke, F., Jenne, D., Holak, T.A., Werb, Z., et al. (2008). Lifeact: a versatile marker to visualize F-actin. Nat Meth *5*, 605–607.

Roadcap, D.W., and Bear, J.E. (2009). Double JMY: making actin fast. Nat Cell Biol *11*, 375–376.

Rogers, S.L., Wiedemann, U., and Stuurman, N. (2003). Molecular requirements for actin-based lamella formation in Drosophila S2 cells. The Journal of Cell Biology *162*, 1079-1088.

Roh-Johnson, M., Shemer, G., Higgins, C.D., McClellan, J.H., Werts, A.D., Tulu, U.S., Gao,

L., Betzig, E., Kiehart, D.P., and Goldstein, B. (2012). Triggering a cell shape change by exploiting preexisting actomyosin contractions. Science *335*, 1232–1235.

Romero, S., Le Clainche, C., Didry, D., Egile, C., Pantaloni, D., and Carlier, M.-F. (2004). Formin Is a Processive Motor that Requires Profilin to Accelerate Actin Assembly and Associated ATP Hydrolysis. Cell *119*, 419–429.

Sahai, E. (2005). Mechanisms of cancer cell invasion. Curr. Opin. Genet. Dev. *15*, 87–96.

Sahai, E., and Marshall, C.J. (2003). Differing modes of tumour cell invasion have distinct requirements for Rho/ROCK signalling and extracellular proteolysis. Nat Cell Biol *5*, 711–719.

Sakata, D., Taniguchi, H., Yasuda, S., Adachi-Morishima, A., Hamazaki, Y., Nakayama, R., Miki, T., Minato, N., and Narumiya, S. (2007). Impaired T lymphocyte trafficking in mice deficient in an actin-nucleating protein, mDia1. J. Exp. Med. *204*, 2031–2038.

Salbreux, G., Charras, G., and Paluch, E. (2012). Actin cortex mechanics and cellular morphogenesis. Trends Cell Biol. *22*, 536–545.

Satoh, N., Kageyama, T., and Sirakami, K.-I. (1976). Motility of dissociated embryonic cells in *Xenopus Laevis*: its significance to morphogenetic movements *. Development, Growth and Differerentiation *18*, 55–67.

Schwob, E., and Martin, R.P. (1992). New yeast actin-like gene required late in the cell cycle. Nature *355*, 179-182.

Servant, G., Weiner, O.D., Neptune, E.R., Sedat, J.W., and Bourne, H.R. (1999). Dynamics of a chemoattractant receptor in living neutrophils during chemotaxis. Mol. Biol. Cell *10*, 1163–1178.

Shi, Y., Zhang, J., Mullin, M., Dong, B., Alberts, A.S., and Siminovitch, K.A. (2009). The mDial formin is required for neutrophil polarization, migration, and activation of the LARG/RhoA/ROCK signaling axis during chemotaxis. J Immunol *182*, 3837–3845.

Shikama, N., Lee, C.W., France, S., Delavaine, L., Lyon, J., Krstic-Demonacos, M., and La Thangue, N.B. (1999). A Novel Cofactor for p300 that Regulates the p53 Response. Molecular Cell *4*, 12–12.

Shortman, K., and Naik, S.H. (2006). Steady-state and inflammatory dendritic-cell development. Nat Rev Immunol *7*, 19–30.

Singh, A., Winterbottom, E.F., Ji, Y.J., Hwang, Y.-S., and Daar, I.O. (2013). Abelson Interactor 1 (Abi1) and Its Interaction with Wiskott-Aldrich Syndrome Protein (Wasp) Are Critical for Proper Eye Formation in Xenopus Embryos. J Biol Chem. *288*, 14135-14146.

Smith, A., Carrasco, Y.R., Stanley, P., Kieffer, N., Batista, F.D., and Hogg, N. (2005). A talin-dependent LFA-1 focal zone is formed by rapidly migrating T lymphocytes. The Journal of

Cell Biology *170*, 141–151.

Snapper, S.B., Takeshima, F., Antón, I., Liu, C.H., Thomas, S.M., Nguyen, D., Dudley, D., Fraser, H., Purich, D., Lopez-Ilasaca, M., et al. (2001). N-WASP deficiency reveals distinct pathways for cell surface projections and microbial actin-based motility. Nat Cell Biol *3*, 897–904.

Sohrmann, M., and Peter, M. (2003). Polarizing without a c(l)ue. Trends Cell Biol. *13*, 526–533.

Sossey-Alaoui, K. (2005). WAVE3-mediated Cell Migration and Lamellipodia Formation Are Regulated Downstream of Phosphatidylinositol 3-Kinase. J. Biol. Chem. *280*, 21748–21755.

Srinivasan, S., Wang, F., Glavas, S., Ott, A., Hofmann, F., Aktories, K., Kalman, D., and Bourne, H.R. (2003). Rac and Cdc42 play distinct roles in regulating PI(3,4,5)P3 and polarity during neutrophil chemotaxis. The Journal of Cell Biology *160*, 375–385.

Stanley, P., Smith, A., McDowall, A., Nicol, A., Zicha, D., and Hogg, N. (2008). Intermediate-affinity LFA-1 binds alpha-actinin-1 to control migration at the leading edge of the T cell. Embo J. *27*, 62–75.

Steffen, A., Faix, J., Resch, G.P., Linkner, J., Wehland, J., Small, J.V., Rottner, K., and Stradal, T.E.B. (2006). Filopodia formation in the absence of functional WAVE- and Arp2/3-complexes. Mol. Biol. Cell *17*, 2581–2591.

Steffen, A., Rottner, K., Ehinger, J., Innocenti, M., Scita, G., Wehland, J., and Stradal, T.E.B. (2004). Sra-1 and Nap1 link Rac to actin assembly driving lamellipodia formation. Embo J. *23*, 749–759.

Steinman, R.M. (1991). The dendritic cell system and its role in immunogenicity. Annu. Rev. Immunol. *9*, 271-296.

Steinman, R.M. (2002). Inaugural Article: Avoiding horror autotoxicus: The importance of dendritic cells in peripheral T cell tolerance. Proceedings of the National Academy of Sciences *99*, 351–358.

Steketee, M.B., and Tosney, K.W. (2002). Three functionally distinct adhesions in filopodia: shaft adhesions control lamellar extension. J. Neurosci. *22*, 8071–8083.

Stradal, T.E.B., Rottner, K., Disanza, A., Confalonieri, S., Innocenti, M., and Scita, G. (2004). Regulation of actin dynamics by WASP and WAVE family proteins. Trends Cell Biol. *14*, 303–311.

Suetsugu, S., Hattori, M., Miki, H., Tezuka, T., Yamamoto, T., Mikoshiba, K., and Takenawa, T. (2002). Sustained activation of N-WASP through phosphorylation is essential for neurite extension. Developmental Cell *3*, 645–658.

Suetsugu, S., Yamazaki, D., Kurisu, S., and Takenawa, T. (2003). Differential roles of WAVE1

and WAVE2 in dorsal and peripheral ruffle formation for fibroblast cell migration. Developmental Cell *5*, 595–609.

Suraneni, P., Rubinstein, B., Unruh, J.R., Durnin, M., Hanein, D., and Li, R. (2012). The Arp2/3 complex is required for lamellipodia extension and directional fibroblast cell migration. The Journal of Cell Biology *197*, 239–251.

Swaney, K.F., Huang, C.-H., and Devreotes, P.N. (2010). Eukaryotic chemotaxis: a network of signaling pathways controls motility, directional sensing, and polarity. Annu Rev Biophys *39*, 265–289.

Swanson, J.A. (2008). Shaping cups into phagosomes and macropinosomes. Nat Rev Mol Cell Biol *9*, 639–649.

Takenawa, T., and Suetsugu, S. (2007). The WASP–WAVE protein network: connecting the membrane to the cytoskeleton. Nat Rev Mol Cell Biol *8*, 37–48.

Takenawa, T., Miki, H., Sasaki, T., and Takai, Y. (1998). Induction of filopodium formation by a WASP-related actin-depolymerizing protein N-WASP : Abstract : Nature. Nature *391*, 93–96.

Tani, K. (2003). Abl Interactor 1 Promotes Tyrosine 296 Phosphorylation of Mammalian Enabled (Mena) by c-Abl Kinase. J. Biol. Chem. *278*, 21685–21692.

Tanizaki, H., Egawa, G., Inaba, K., Honda, T., Nakajima, S., Moniaga, C.S., Otsuka, A., Ishizaki, T., Tomura, M., Watanabe, T., et al. (2010). Rho-mDia1 pathway is required for adhesion, migration, and T-cell stimulation in dendritic cells. Blood *116*, 5875–5884.

TAYLOR, R.B., DUFFUS, W.P.H., RAFF, M.C., and de PETRIS, S. (1971). Redistribution and Pinocytosis of Lymphocyte Surface Immunoglobulin Molecules Induced by Anti-Immunoglobulin Antibody. Nature *233*, 225–229.

Tickle, C.A., and Trinkaus, J.P. (1973). Changes in surface extensibility of Fundulus deep cells during early development. Journal of Cell Science *13*, 721–726.

Trinkaus, J.P. (1973). Surface activity and locomotion of Fundulus deep cells during blastula and gastrula stages. Dev. Biol. *30*, 69–103.

Trinkaus, J.P., and Lentz, T.L. (1967). Surface specializations of Fundulus cells and their relation to cell movements during gastrulation. The Journal of Cell Biology *32*, 139–153.

Veltman, D.M., King, J.S., Machesky, L.M., and Insall, R.H. (2012). SCAR knockouts in Dictyostelium: WASP assumes SCAR's position and upstream regulators in pseudopods. The Journal of Cell Biology *198*, 501-508.

Vicente-Manzanares, M., and Sánchez-Madrid, F. (2004). Role of the cytoskeleton during leukocyte responses. Nat Rev Immunol *4*, 110–122.

Vicente-Manzanares, M., Choi, C.K., and Horwitz, A.R. (2009). Integrins in cell migration--the actin connection. Journal of Cell Science *122*, 199–206.

Vicker, M.G. (1989). Gradient and temporal signal perception in chemotaxis. Journal of Cell Science *92 (Pt 1)*, 1–4.

Vicker, M.G., Lackie, J.M., and Schill, W. (1986). Neutrophil leucocyte chemotaxis is not induced by a spatial gradient of chemoattractant. Journal of Cell Science *84*, 263–280.

Vignjevic, D., Schoumacher, M., Gavert, N., Janssen, K.-P., Jih, G., Laé, M., Louvard, D., Ben-Ze'ev, A., and Robine, S. (2007). Fascin, a novel target of beta-catenin-TCF signaling, is expressed at the invasive front of human colon cancer. Cancer Res. *67*, 6844–6853.

Vinzenz, M., Nemethova, M., Schur, F., Mueller, J., Narita, A., Urban, E., Winkler, C., Schmeiser, C., Koestler, S.A., Rottner, K., et al. (2012). Actin branching in the initiation and maintenance of lamellipodia. Journal of Cell Science *125*, 2775-2785.

Vonna, L., Wiedemann, A., Aepfelbacher, M., and Sackmann, E. (2007). Micromechanics of filopodia mediated capture of pathogens by macrophages. Eur. Biophys. J. *36*, 145–151.

Wang, T., Cleary, R.A., Wang, R., and Tang, D.D. (2013). Role of the adapter protein Abi1 in actin-associated signaling and smooth muscle contraction. J Biol Chem. *288*, 20713-20722.

Watanabe, N., and Higashida, C. (2004). Formins: processive cappers of growing actin filaments. Experimental Cell Research *301*, 16-22.

Weber, M., Hauschild, R., Schwarz, J., Moussion, C., de Vries, I., Legler, D.F., Luther, S.A., Bollenbach, T., and Sixt, M. (2013). Interstitial Dendritic Cell Guidance by Haptotactic Chemokine Gradients. Science *339*, 328–332.

Weber, M., and Sixt, M. (2013). Live Cell Imaging of Chemotactic Dendritic Cell Migration in Explanted Mouse Ear Preparations. Methods in Molecular Biology *1013*, 215-226.

Wedlich-Söldner, R., and Li, R. (2003). Spontaneous cell polarization: undermining determinism. Nat Cell Biol *5*, 267–270.

Weiner, O.D., Rentel, M.C., Ott, A., Brown, G.E., Jedrychowski, M., Yaffe, M.B., Gygi, S.P., Cantley, L.C., Bourne, H.R., and Kirschner, M.W. (2006). Hem-1 Complexes Are Essential for Rac Activation, Actin Polymerization, and Myosin Regulation during Neutrophil Chemotaxis. Plos Biol *4*, e38.

Welch, M.D., and Mullins, R.D. (2002). Cellular control of actin nucleation. Annu. Rev. Cell Dev. Biol. *18*, 247–288.

Wettschureck, N., and Offermanns, S. (2005). Mammalian G Proteins and Their Cell Type Specific Functions. Physiol. Rev. *85*, 1159-1204.

Wiesner, S., Helfer, E., Didry, D., Ducouret, G., Lafuma, F., Carlier, M.-F., and Pantaloni, D.

(2003). A biomimetic motility assay provides insight into the mechanism of actin-based motility. The Journal of Cell Biology *160*, 387–398.

Witke, W., Sharpe, A.H., Hartwig, J.H., Azuma, T., and Stossel, T.P. (1995). Hemostatic, inflammatory, and fibroblast responses are blunted in mice lacking gelsolin. Cell *81*, 41-51.

Wolf, K., Lindert, te, M., Krause, M., Alexander, S., Riet, te, J., Willis, A.L., Hoffman, R.M., Figdor, C.G., Weiss, S.J., and Friedl, P. (2013). Physical limits of cell migration: Control by ECM space and nuclear deformation and tuning by proteolysis and traction force. The Journal of Cell Biology *201*, 1069–1084.

Wolf, K., Mazo, I., Leung, H., Engelke, K., Andrian, von, U.H., Deryugina, E.I., Strongin, A.Y., Bröcker, E.B., and Friedl, P. (2003a). Compensation mechanism in tumor cell migration: mesenchymal-amoeboid transition after blocking of pericellular proteolysis. The Journal of Cell Biology *160*, 267–277.

Wolf, K., Müller, R., Borgmann, S., Bröcker, E.B., and Friedl, P. (2003b). Amoeboid shape change and contact guidance: T-lymphocyte crawling through fibrillar collagen is independent of matrix remodeling by MMPs and other proteases. Blood *102*, 3262–3269.

Wu, C., Asokan, S.B., Berginski, M.E., Haynes, E.M., Sharpless, N.E., Griffith, J.D., Gomez, S.M., and Bear, J.E. (2012). Arp2/3 is critical for lamellipodia and response to extracellular matrix cues but is dispensable for chemotaxis. Cell *148*, 973–987.

Xiao, Z., Zhang, N., Murphy, D.B., and Devreotes, P.N. (1997). Dynamic distribution of chemoattractant receptors in living cells during chemotaxis and persistent stimulation. The Journal of Cell Biology *139*, 365–374.

Yae, K., Keng, V.W., Koike, M., and Yusa, K. (2006). Sleeping beauty transposon-based phenotypic analysis of mice: lack of Arpc3 results in defective trophoblast outgrowth. Molecular And Cellular Biology *26*, 6185-6196.

Yamazaki, D., Fujiwara, T., Suetsugu, S., and Takenawa, T. (2005). A novel function of WAVE in lamellipodia: WAVE1 is required for stabilization of lamellipodial protrusions during cell spreading. Genes Cells *10*, 381–392.

Yamazaki, D., Suetsugu, S., Miki, H., Kataoka, Y., Nishikawa, S.-I., Fujiwara, T., Yoshida, N., and Takenawa, T. (2003). WAVE2 is required for directed cell migration and cardiovascular development. Nature *424*, 452–456.

Yan, C., Martinez-Quiles, N., Eden, S., Shibata, T., Takeshima, F., Shinkura, R., Fujiwara, Y., Bronson, R., Snapper, S.B., Kirschner, M.W., et al. (2003). WAVE2 deficiency reveals distinct roles in embryogenesis and Rac-mediated actin-based motility. Embo J. *22*, 3602–3612.

Yanai, M., Kenyon, C.M., Butler, J.P., Macklem, P.T., and Kelly, S.M. (1996). Intracellular pressure is a motive force for cell motion in Amoeba proteus. Cell Motil. Cytoskeleton *33*, 22–29.

Yang, J., and Weinberg, R.A. (2008). Epithelial-Mesenchymal Transition: At the Crossroads of Development and Tumor Metastasis. Developmental Cell *14*, 818–829.

Yoshida, K., and Soldati, T. (2006). Dissection of amoeboid movement into two mechanically distinct modes. Journal of Cell Science *119*, 3833–3844.

Zaki, M., King, J., Fütterer, K., and Insall, R.H. (2007). Replacement of the essential Dictyostelium Arp2 gene by its Entamoeba homologue using parasexual genetics. BMC Genet *8*, 28.

Zech, T.T., Calaminus, S.D.J.S., Caswell, P.P., Spence, H.J.H., Carnell, M.M., Insall, R.H.R., Norman, J.J., and Machesky, L.M.L. (2011). The Arp2/3 activator WASH regulates α5β1-integrin-mediated invasive migration. Journal of Cell Science *124*, 3753–3759.

Zuchero, J.B., Coutts, A.S., Quinlan, M.E., Thangue, N.B.L., and Mullins, R.D. (2009). p53-cofactor JMY is a multifunctional actin nucleation factor. Nat Cell Biol *11*, 451–459.

SUPPLEMENTARY MOVIE LEGENDS

Movies S1 and S2. Immature *WT* (S1, AVI 230 KB) and *Hem1*^{-/-} (S2, AVI 374 KB) BMDCs in solution. Time-lapse differential interference contrast (DIC) microscopy of fully differentiated but immature "steady state" BMDCs. Cell behaviour was followed over 60 seconds (1 sec/frame, 61 frames, 30 fps).

Movies S3 and S4. Mature *WT* (S3, AVI 726 KB) and *Hem1*^{-/-} (S4, AVI 743 KB) BMDCs in solution. The experiment descript in Movie S2 was repeated with mature BMDCs. Cell behaviour was followed over 120 seconds (1 sec/frame, 121 frames, 30 fps).

Movie S5. Actin network organization of immature *WT* (S5, AVI 63.1 MB) BMDCs. z-scan of tomogram and model corresponding to Fig. 18C. The first part of the video shows a scan through tomogram stacks from the dorsal to the ventral surface of a *WT* lamellipodium edge with selected branch junctions highlighted in red circles. This is followed by a combination of the tomogram stacks with the positions of branch junctions in the stack superimposed as red spots. Finally, the complete model of the branch junctions and the adjacent filaments (green lines). Black particles with a white halo in tomogram scan are gold particles used for aligning the tilt series during back projection.

Movie S6. Actin network organization of immature *Hem1*^{-/-} (S6, AVI 48.8 MB) BMDCs. z-scan of tomogram and model corresponding to Fig. 18D The first part of the video shows a scan through tomogram stacks from the dorsal to the ventral surface of a complete branch-free *Hem1*^{-/-} leading tip. Selected branch junctions highlighted in red circles. This is followed by a combination of the tomogram stacks superimposed with the positions of filaments (green lines) and their orientation (red dots = barbed ends) obtained as described in Fig. 18. Black particles with a white halo in tomogram scan are gold particles used for aligning the tilt series during back projection.

Movies S7 and S8. Exemplary 3D migration behaviour of an immature *WT* (S7, AVI, 1.5 MB) and a *Hem1*^{-/-} BMDC (S8, AVI, 1.4 MB). High magnification time-lapse movies of migrating BMDCs in a 3D collagen matrix corresponding to Fig. 20A/B. Migration behaviour was monitored over 4.5 minutes (2 sec/frame, 135 frames, 30 fps, 63x objective).

Movies S9 and S10. Immature *WT* (S9) and *Hem1*^{-/-} (S10) BMDCs migrating in a 3D collagen gel in the presence of uniform CCL3 (both AVIs 8.7 MB) Time-lapse movie of BMDCs embedded in a 3D collagen matrix and migrating in a uniform CCL3 field. Individual trajectories are followed over time periods of 30 to 60 min and illustrated in colours. Their plotted trajectories are shown in Fig. 20D/E. Cell behaviour was monitored over 4 hours (1 min/frame, 241 frames, 15 fps, 10x objective).

Movies S11 and S12. 3D migration of immature *WT* (S11, AVI, 6.9 MB) and *Hem1*^{-/-} BMDCs (S12, AVI, 7.7 MB) in a CCL3 gradient. Time-lapse movies of BMDCs embedded in a 3D collagen matrix and migrating in a CCL3 gradient corresponding to Fig. 21A. The

chemokine source is located at the movie top. Migration behaviour was monitored over 30 minutes (30 sec/frame, 60 frames, 20 fps, 4x objective).

Movies S13 and S14. Exemplary 3D migration behaviour of a mature *WT* (S13, AVI, 1.7 MB) and a *Hem1*^{-/-} BMDC (S14, AVI, 1.9 MB). High magnification time-lapse movies of migrating BMDCs in a 3D collagen matrix corresponding to Fig. 22A/B. The chemokine source is located at the movie top. Migration behaviour was monitored over 150 seconds (1 sec/frame, 151 frames, 60 fps, 63x objective).

Movies S15 and S16. Chemotacting mature *WT* (S15) and *Hem1*^{-/-} (S16) BMDCs in a 3D collagen gel (both AVIs 5.7 MB) Time-lapse movie of BMDCs embedded in a 3D collagen matrix and migrating along a CCL19 gradient. The chemokine source is located at the movie top. Migration behaviour was monitored over 3 hours (3 min/frame, 60 frames, 10 fps, 10x objective).

Movies S17 (AVI, 3.9 MB) and S18 (AVI, 3.1 MB). Spatial and temporal dynamics of the actin cytoskeleton in BMDCs on adhesive surfaces. Lifeact-GFP transfected BMDCs migrate under agarose on an adhesive glass towards a CCL19 gradient. An exemplary *WT* (S17) and *Hem1*^{-/-} (S18) BMDC is shown. TIRF microscopy, time-lapse over the indicated time (2 s/frame, 24fps, 63x objective).

Movies S19 (AVI, 3.4 MB) and S20 (AVI, 2.1 MB). Spatial and temporal dynamics of the actin cytoskeleton in BMDCs on inert surfaces. Lifeact-GFP transfected dendritic cell migrates under agarose on a PEG-coated surface towards a CCL19 gradient. An exemplary *WT* (S19) and *Hem1*^{-/-} (S20) BMDC is shown. TIRF microscopy, time-lapse over the indicated time (1.6 s/frame, 30fps, 63x objective).

Movies S21 (AVI, 7.4 MB) and S22 (AVI, 3.5 MB). Arp2/3 dynamics in migrating BMDCs. TIRF time-lapse movies of BMDCs transfected with ArpC5–GFP migrating on a PEG-coated coverslip under agarose. An exemplary *WT* (S21) and *Hem1*^{-/-} (S22) BMDC is shown. Migration was monitored over the indicated time (1.6 sec/frame, 30 fps, 63x objective).

Movies S23 (AVI, 10.9 MB) and S24 (AVI, 5.5 MB). WASp dynamics in migrating BMDCs. TIRF time-lapse movies of BMDCs transfected with WASp–GFP migrating on a PEG-coated coverslip under agarose. An exemplary *WT* (S23) and *Hem1*^{-/-} (S24) BMDC is shown. Migration was monitored over the indicated time (1 sec/frame, 24 fps, 63x objective).

Movies S25 (AVI, 4.1 MB) and S26 (AVI, 3.9 MB). VASP dynamics in BMDCs migrating on adhesive surfaces. VASP-GFP transfected BMDCs migrate under agarose on an adhesive glass towards a CCL19 gradient. An exemplary *WT* (S25) and *Hem1*^{-/-} (S26) BMDC is shown. TIRF microscopy, time-lapse over the indicated time (2 s/frame, 24fps, 63x objective).

Movies S27 (AVI, 4.2 MB) and S28 (AVI, 1.8 MB). VASP dynamics in BMDCs migrating on inert surfaces. VASP-GFP transfected BMDCs migrate under agarose on PEG-coated

surface towards a CCL19 gradient. An exemplary *WT* (S27) and *Hem1^{-/-}* (S28) BMDC is shown. TIRF microscopy, time-lapse over the indicated time (1.6 s/frame, 30fps, 63x objective).

Movies S29 (AVI, 239 KB) and S30 (AVI, 549 KB). Membrane wave dynamics of immature *Hem1^{-/-}* BMDCs. Time-lapse movies of an immature migrating (S29) and stuck (S30) *Hem1^{-/-}* BMDCs in a 3D collagen matrix. Cell behaviour was observed over the indicated time (2.4 s/frame, 25 fps, 63x objective).

Movies S31 (AVI, 9.3 MB), S32 (AVI, 11.2 MB) and S33 (AVI, 8.8 MB). Confined migration of immature *Hem1^{-/-}* BMDCs. Time-lapse movies of immature *Hem1^{-/-}* BMDCs migrating in a confining setup (4 μm confinement). Cells migration was observed on adhesive glass (S31), PEG-coated surfaces (S32) and in the presence of 5 mM EDTA (S33), respectively, over the indicated time (1min/frame, 20 fps, 4x objective).

SUPPLEMENTARY STATISTICAL ANALYSIS

T-tests and ANOVAs were performed after data were confirmed to fulfill the criteria, otherwise Kruskal-Wallis tests or Mann-Whitney U-tests were applied. If overall ANOVA or Kruskal-Wallis tests were significant, we performed posthoc tests with pair-wise comparison (ANOVA: Bonferroni, Kruskal-Wallis: Dunn). Analyses were performed with GraphPad Prism.

Figure	Sample(s)	Test statistic	Samples size/ Degrees of freedom	P-value	Posthoc test
16B	*WT* DMSO vs. *Hem1*^{-/-} DMSO	Mann-Whitney U=3639	n=150	P<0.0001	
	WT DMSO vs. all *WT* inhibitors	Kruskal-Wallis; H=157.2	df=3	P<0.0001	Dunn's, selected pairs, for details see next table
	Hem1^{-/-} DMSO vs. all *Hem1*^{-/-} inhibitors	Kruskal-Wallis; H=220.5	df=3	P<0.0001	Dunn's, selected pairs, for details see next table
20C	*WT* vs. *Hem1*^{-/-}	t-test, t=22.56	df=596		
21B	all samples; (transformed to obtain normalized data Y=log(Y))	ANOVA F=111.5	df=3,488	P<0.0001	Bonferroni's, selected pairs, for details see next table
21C	all samples	Kruskal-Wallis; H=288.5	df=3	P<0.0001	Dunn's, selected pairs, for details see next table
22B	all samples; (transformed to obtain normalized data Y=log(Y))	ANOVA F=40.82	df=2,536	P<0.0001	Bonferroni's, selected pairs, for details see next table
22C	*WT* vs. *Hem1*^{-/-} 1.1 mg/ml (transformed to obtain normalized data Y=sqrt(Y))	t-test, t=5.134	df=176	P<0.0001	

	WT vs. *Hem1*$^{-/-}$ 1.1 mg/ml (transformed to obtain normalized data Y=sqrt(Y))	t-test, *t*=6.513	df=167	P<0.0001	
	WT vs. *Hem1*$^{-/-}$ 1.1 mg/ml (transformed to obtain normalized data Y=sqrt(Y))	t-test, *t*=12.37	df=157	P<0.0001	
23C	all samples; (transformed to obtain normalized data Y=log(Y))	ANOVA *F*=17.15	df=2,48	P<0.0001	Bonferroni's, selected pairs, for details see next table

Posthoc tests of Figs. 16B, 21B/C, 22B and 23C:

Kruskal Wallis; posthoc all pairwise comparison (Dunn's Method)

ANOVA; posthoc compare selected pairs (Bonferroni's Method)

Figure	Comparison	P-value
16B	*WT* DMSO vs. *WT* LatA	P<0.05
	WT DMSO vs. *WT* Bleb	P<0.05
	WT DMSO vs. *WT* Noco	ns
	Hem1$^{-/-}$ DMSO vs. *Hem1*$^{-/-}$ LatA	P<0.05
	Hem1$^{-/-}$ DMSO vs. *Hem1*$^{-/-}$ Bleb	ns
	Hem1$^{-/-}$ DMSO vs. *Hem1*$^{-/-}$ Noco	ns
21B	*WT* vs. *WT* EDTA	P<0.05
	WT vs. *Hem1*$^{-/-}$	P<0.05
	Hem1$^{-/-}$ vs. *Hem1*$^{-/-}$ EDTA	P<0.05
21C	*WT* vs. *WT* Blebbi	P<0.05
	WT vs. *Hem1*$^{-/-}$	P<0.05
	Hem1$^{-/-}$ vs. *Hem1*$^{-/-}$ Blebbi	P<0.05

22B	WT vs. $WASp^{-/-}$	$P<0.05$
	WT vs. $Hem1^{-/-}$	$P<0.05$
	$WASp^{-/-}$ vs. $Hem1^{-/-}$	$P<0.05$
23C	WT/WT^{-} vs. $WT/WASp^{-/-}$	$P<0.05$
	WT/WT^{-} vs. $WT/Hem1^{-/-}$	$P<0.05$
	$WT/WASp^{-/--}$ vs. $WT/Hem1^{-/-}$	$P<0.05$

ACKNOWLEDGEMENTS

An important institution of this work was our daily kicker match. Therefore, many thanks to all the kicker victims: Daniel Capek, Jan Schwarz, Martin Behrndt, Maurizio Monti, Michael Smutny, Pedro Campino, Philipp Schmalhorst and Vanessa Barone. You essentialy helped cheering me up after unsuccessful experiments. A special thanks to Gabby Krens: WE ARE THE (KICKER-) CHAMPIONS – my friend!

I also want to insist in thanking my friends and scientific fellows Klaus Heger and Maxi Kern. We've been suffering and celebrating together in science as well as in private for almost a decade and became really good friends. Meeting you guys was a real gain. To quote a wise man's words: "Gute Freunde kann niemand trennen…".

A very important person for my PhD life who deserves to be mentioned individually is Michele Weber. At any time she was willing to listen to my problems and helped in solving them. It is good to have a friend like you. A simple 'thank you' does for sure not compare to your efforts. But anyhow, thanks a lot Michele and a big hug to Australia!

It was also a real pleasure to meet and collaborate with Prof. Dr. Ludger Klein and his team. Aside from our scientific work, I have also benefited greatly in my private life. Thanks a lot to Martin Aichinger. I think it was a legendary FACS evening and I am very glad for your friendship.

As it turned out later, meeting Maria Hinterberger was even more important and influential. In terms of the most beautiful "sideproject" of this thesis I would like to thank you, Maria! I am deeply grateful to have you and also Johannes. You constantly show me what really matters in life. I really enjoy any time I can spend with you. I am very much looking forward to our shared future!

Last but not least I would like to honour my parents for the freedom to do whatever I chose. They always accepted and supported my decisions without any doubts and believed in my abilities.

- Iucundi acti labores –